ISSN:2661-4448(online)
2661-443X(print)
Volume 2 No.2 2020

MECHANICAL ENGINEERING SCIENCE

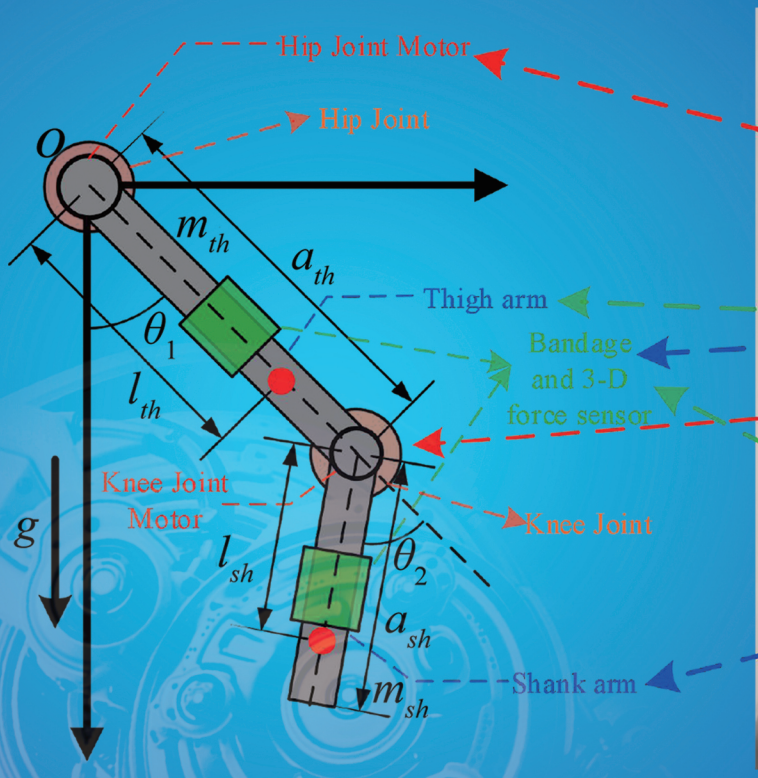

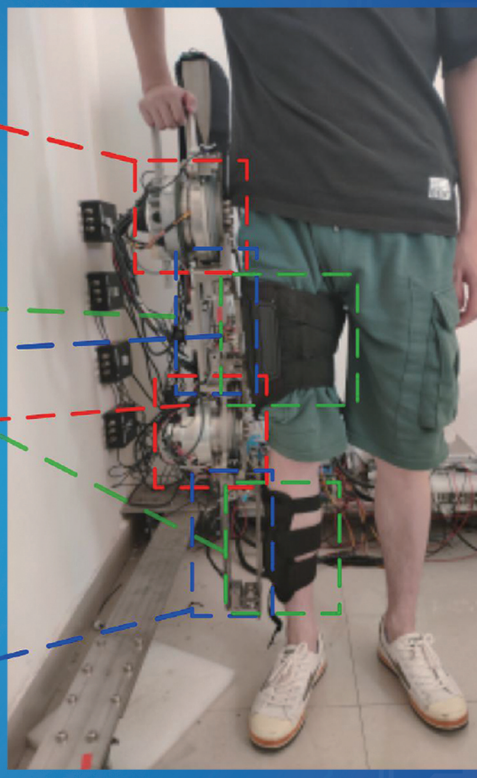

VISER
www.viserdata.com

COMPANY INTRODUCTION

Viser Technology Pte. Ltd. was founded in Singapore with branch offices in both Hebei and Chongqing, China. Viser focuses on publishing scientific and technological journals and books that promote the exchange of scientific and technological findings among the research community and around the globe. Despite being a young company, Viser is actively connecting with well-known universities, research institutes, and indexation database, and has already established a stable collaborative relationship with them. We also have a group of experienced editors and publishing experts who are dedicated to publishing high-quality journal and book contents. We offer the scholars various academic journals covering a variety of subjects and we are committed to reducing the hassles of scholarly publishing. To achieve this goal, we provide scholars with an all-in-one platform that offers solutions to every publishing process that a scholar needs to go through in order to show their latest finding to the world.

Mechanical Engineering Science

Publisher: Viser Technology Pte. Ltd.

ISSN: 2661-4448 (online)
2661-443X (print)

Frequency: Semi-annual

Add.:21 Woodlands Close, #08-18,
Primz Bizhub SINGAPORE (737854)

https://www.viserdata.com/

Mechanical Engineering Science

Volume 2 No.2 (2020)

CONTENTS

VISER

Message from Special Issue of Intelligent Fluid Dynamics Technology

In the past decades, fluid transmission technology has made remarkable achievements and its application scope covers almost all walks of life. However, the complexity of fluid dynamics technology makes it face severe challenges in data analysis and mining, model application difficulties and so on. Fortunately, the development of intelligent science makes it possible to solve these problems. A new round of technological revolution and industrial transformation driven by artificial intelligence and its main core technology are changing the world pattern and becoming another great leap in the development process of human society.

In recent years, artificial intelligence has been widely used in many fields of fluid transmission technology. In the research of fluid drive control, neural network is used to identify the model of fluid transmission system and expert system is used to realize fault diagnosis of fluid transmission system; in fluid dynamics calculation, artificial intelligence can improve turbulence prediction accuracy and accelerate the research of data visualization analysis.

In the future, intelligent power conversion technology is used to replace throttling to solve the problem of resistance control and realize regeneration and power sharing; new visual sensing technology is used to collect system data to realize efficient energy conversion and health management. Joint efforts in efficient transmission, energy management and prediction development are the cornerstones to realize intelligent dynamics drive technology. It makes sure that the intelligent dynamics technology will encounter new challenges, new opportunities and will make many new contributions.

In order to timely report the latest research achievements of intelligent dynamics technology and provide opportunities for academic exchange, we especially organized a special issue of intelligent dynamics technology. Professor Shi Yan from Beihang University and Professor Yao Jing from Yanshan University are specially invited to organize this issue. With the strong support of the two professors, a number of scholars engaged in the research of intelligent dynamics technology were invited to write articles, which ensured the publication of the special issue at a high level.

Finally, we would like to thank Professor Shi Yan and Professor Yao Jing for their efforts in publishing this special issue. From the planning of the special issue, the organization of manuscripts, the recommendation of experts and the review of manuscripts, the two professors have given their warm, rigorous and meticulous help in the whole process, which providing strong technical guarantee and selfless dedication for the academic quality of special issue. We would like to express our high respect and sincere gratitude.

Planner Author

Yan SHI professor of Automation Science and Electrical Engineering Academy in Beijing University of Aeronautics and Astronautics, deputy director in Beijing Key Laboratory of Pneumatic Thermal Energy Storage and Energy Technology, director in Key Laboratory of Machinery Industry Compressed Air Energy Conservation and Energy Storage. Mainly engaged in the theory and technology of precision detection and control in pneumatic systems; proposed a number of key common detection theories and methods for pneumatic components which have been adopted as one of the National Standards and one of the Industry Standards; proposed a number of pneumatic systems Energy-saving control theory and technology which has been recommended as the key technology in Machinery Industry to promote during The 12th five-year plan period.

Jing YAO (1978—) obtained a doctor degree of engineering at Yanshan University in 2009. Currently, she is professor and doctoral supervisor and now serve as the vice dean of School of Mechanical Engineering, Yanshan University, China. Since 2009, she started the teaching and study at Yanshan University. In 2014 and 2015, she visited the University of California at Davis and IFAS Institute of Aachen University in Germany. At present, she has presided over more than 10 national projects including the National Key R & D project and National Natural Science Foundation projects of China and 5 million-level social service projects, and participated in 1 Major Project of National Natural Science Foundation of China. She was selected as "Millions of Talent Projects National Candidates" and won the title of "Young and Middle-aged Experts with Outstanding Contributions", and won the First Prize of Science and Technology, the First Prize Award of Teaching Achievement and Excellent Educators Award in Hebei Province and other 8 awards. Her research focuses on heavy equipment of high-power hydraulic servo system, high-performance proportional hydraulic components, high-precision control algorithm, digital hydraulic technology, intelligent hydraulic technology, etc. Moreover, she published nearly 60 papers, including 23 in SCI and EI, and wrote 2 books and authorized 25 patents.

About the author

Qing GUO received the B.E. degree in Automation from Harbin Institute of Technology, Harbin, China, in 2003, and the M.S. and Ph.D. degrees in Navigation, Guidance and Control from Harbin Institute of Technology, in 2005 and 2008, respectively. Now Dr. Guo is a full professor in School of Aeronautics and Astronautics, University of Electronic Science and Technology of China. Dr. Guo is also the backup candidates for academic and technical leaders in Sichuan Province, the member of Fluid transmission and control branch, Chinese Mechanical Engineering Society, the Senior member of Mechanical Engineering Society, Youth expert group leader of the committee on fluid control and Engineering, Chinese society of mechanics. His research interests include robust and adaptive control, electrohydraulic, exoskeleton \& rehabilitation robot.

Tao YU (1979.02—), male, received his PhD from Northeastern University in China. He is now a professor and vice president of the School of Electromechanical and Automotive Engineering in Yantai University. He serves as member of the standing director of the Rotor dynamics Committee of China Vibration Engineering Society, member of Shandong Mechanical Engineering Society, member of The Technical Committee for Standardization of After-sales Service of Shandong Province, leader of the first batch of Outstanding young Innovation teams in Shandong Province, leader of Shandong province first-class professional major 'Mechanical design, Manufacturing and automation'. His research interests include mechanical dynamic design, mechanical fault diagnosis and state monitoring, vibration control and advanced damping vibration reduction, virtual simulation technology, industrial robot application integration, etc.

Wei ZHONG (1983—) male, He currently is an Associate Professor with the School of Mechanical Engineering, Jiangsu University of Science and Technology, China. He was admitted to Zhejiang University in September 2001, majored in Mechatronics engineering. He received the Bachelor degree in 2006 (five-year program) and the Ph.D. degree in mechatronics engineering in 2011 from Zhejiang University, China. From Oct 2008 to Sep 2010, he visited Tokyo Institute of Technology as a visiting researcher funded by the China Scholarship Council. His main research interests lie in pneumatic transmission and control, gas lubrication theory and application technology, and industrial automation test.

About the author

Chunyou ZHANG graduated from Inner Mongolia Agricultural University with a master's degree in engineering. At present, he is an associate professor in Inner Mongolia University for Nationalities. He is currently working toward the Ph.D. degree with Beihang University, Beijing China. His research interests include oil field energy saving technology, new energy utilization, fluid transmission and control, robot technology and so on.

Yeming ZHANG (1979.8—) male, Han nationality, Feicheng, Shandong Province, has a doctor's degree and an associate professor. He is a senior member of China Society of Mechanical Engineering (G16150551), member of pneumatic special committee of fluid transmission and control branch of China Society of mechanical engineering, and preparatory member of national hydraulic and pneumatic Standardization Technical Committee. In June 2011, he graduated from the Department of mechanical and electronic engineering, School of Automation Science and electrical engineering, Beijing University of Aeronautics and Astronautics, with a doctor's degree in engineering.

He has presided over or participated in more than 20 projects, such as the science and Technology Commission of the Military Commission, the National Natural Science Foundation, the national science and technology support plan, the doctoral program of the Ministry of education, the General Administration of quality supervision and Quarantine of the people's Republic of China, tackling key scientific and technological problems in Henan Province, basic scientific research business expenses of colleges and universities in Henan Province, and major enterprise projects.

Qihui YU received the Ph.D. degree from Beihang University (BUAA), China, in 2015. He is currently an Associate professor with the Inner Mongolia University of Science and Technology. He currently hosts an open Foundation of the State Key Laboratory of Fluid Power and Mechatronic Systems in Zhejiang University, the Natural Science Foundation of Inner Mongolia (Grant No. 2018BS05003). His research interests include energy saving of compressed air system, new energy technology, and heat exchange technique.

Viser Technology Pte. Ltd.
Mechanical Engineering Science
doi: 10.33142/mes.v2i2.3160

Research Article Open Access

Robust Sliding Mode Control for a 2-DOF Lower Limb Exoskeleton Base on Linear Extended State Observer

Zhenlei CHEN[1, 2], Qing GUO[1, 2*], Yao YAN[1, 2], Dan JIANG[3]

1 School of Aeronautics and Astronautics, University of Electronic Science and Technology of China, Chengdu, China
2 Aircraft Swarm Intelligent Sensing and Cooperative Control Key Laboratory of Sichuan Province, Chengdu, China
3 School of Mechanical and Electrical Engineering, University of Electronic Science and Technology of China, Chengdu, China

***Corresponding Author:** Qing GUO, guoqinguestc@163.com*

Abstract:
For the 2- Degree of Freedom (DOF) lower limb exoskeleton, to ensure the system robustness and dynamic performance, a linear-extended-state-observer-based (LESO) robust sliding mode control is proposed to not only reduce the influence of parametric uncertainties, unmodeled dynamics, and external disturbance but also estimate the unmeasurable real-time joint angular velocity directly. Then, via Lyapunov technology, the stability of the corresponding LESO and controller is proven. The appropriate and reasonable simulation was carried out to verify the effectiveness of the proposed LESO and exoskeleton controller.

Keywords: *lower limb exoskeleton; linear-extended-state-observer; robust sliding model control; uncertain nonlinearity*

1 Introduction

For the 2- Degree of Freedom (DOF) lower limb exoskeleton, a linear-With the development of the world economy, and the improvement of human living level, wearable robots have played the key role in the field of medical rehabilitation and industrial production. The exoskeleton, a typical wearable robot, can help specific groups of people complete specific human-machine collaboration tasks, such as assisting hemiplegic patients with rehabilitation training or assisting workers to complete heavy tasks. However, since the complexity and fragility of the human environment, the requirements for the dynamic performance and robustness of the exoskeleton robot are relatively high.

To improve the robustness and dynamic tracking performance of the exoskeleton robot system, many advanced nonlinear controllers have been investigated, such as fuzzy adaptive control [1], repetitive learning control [2], RBFNN adaptive control [3], and discrete-time extended state observer-based intelligent PD control [4]. The training mechanism has been roughly divided into two categories for the exoskeleton: active mechanism and passive mechanism [5]. More specifically, the designed training trajectory is predefined for the passive mechanism without considering the real-time human motion intention [6-7]. Conversely, the training trajectory is designed based on the current human's motion intention for the active mode. The impedance control [8] and admittance control [9] usually are adopted to ensure compliance between humans and the exoskeleton. Li *et al.* [10] assumed admittance control to deal with a human subject's intention. Yu *et al.* [11] proposed an adaptive impedance control strategy to compensate for dynamic uncertainties.

To deal with the parameter uncertainty and external disturbance, designing the related observer to estimate the unknown form is used as the controller design compensation. The disturbance observer mainly includes sliding mode disturbance observer [12], extended state observer (ESO) [13], and so on. In [14], an extended state observer-based integral sliding mode control is adopted in the underwater robot. For the electro-hydraulic system, Guo *et al.* [15] proposed an ESO-based backstepping controller. Furthermore, Sun *et al.* [16] proposed a sliding-mode-disturbance-observer-based tracking control strategy for Euler–Lagrange systems modeling uncertainties and external disturbances.

In this paper, as shown in figure 1, to improve the robustness and dynamic performance of the 2-DOF lower limb exoskeleton, a linear-extended-state-observer-based (LESO) robust sliding mode control is proposed to estimate the unmeasurable joint angular velocity and the error consisting of dynamic deviation and external disturbance. Finally, the related simulation experiment was carried out to verify the effectiveness of the controller.

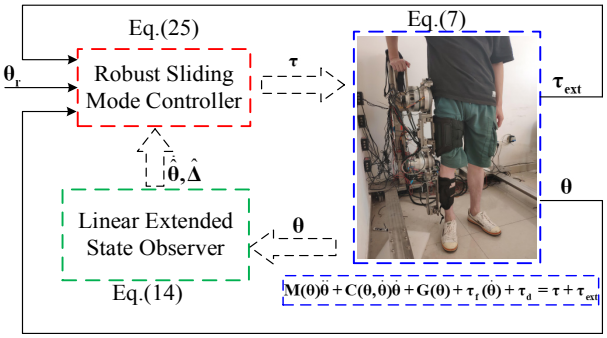

Figure 1 Robust sliding mode control diagram of 2-DOF lower limb exoskeleton

2 Sliding Mode Control for 2-DOF Lower Limb Exoskeleton

2.1 Dynamic of the 2-DOF lower limb exoskeleton

The 2-DOF lower limb exoskeleton that needs to be modeled is shown in the right subgraph of figure 2. According to the human lower limb's physiological structure, the mechanical structure of the prototype is composed of thigh arm, shank arm, hip joint motor, and knee joint motor, and the hip joint motor is fixed on the bracket. Then, the operator and exoskeleton are connected by the bandage and 3-Dimension (3-D) force sensor. Furthermore, the real-time joint position is measured by the absolute encoder, but the joint velocity is measured directly.

At figure 2, O represents the origin of the coordinate system, $\theta_1$and $\theta_2$denote the angular positions of the hip joint and knee joint, $m_{th}$and m_{sh}denote the weights of the thigh arm and shank arm, $a_{th}$and a_{sh}denote the length of the thigh arm and shank arm, $l_{th}$and l_{sh}denote the centroid distance, and g denote the gravity constant.

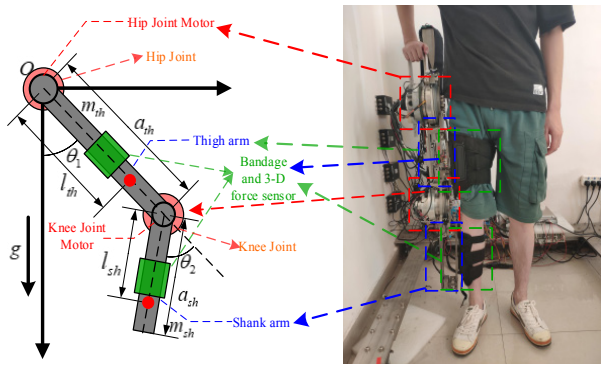

Figure 2 Mechanical structure diagram and physical diagram of 2-DOF lower limb exoskeleton.

According to the [17], the ideal Lagrangian dynamic of the exoskeleton with human-robot interaction and joint friction is model as

$$\mathbf{M}(\boldsymbol{\theta})\ddot{\boldsymbol{\theta}}+\mathbf{C}(\boldsymbol{\theta},\dot{\boldsymbol{\theta}})\dot{\boldsymbol{\theta}}+\mathbf{G}(\boldsymbol{\theta})+\boldsymbol{\tau}_f(\dot{\boldsymbol{\theta}})=\boldsymbol{\tau}+\boldsymbol{\tau}_{ext} \tag{1}$$

where the $\boldsymbol{\theta}=[\theta_1;\theta_2]$ denote the joint angular position, $\boldsymbol{\tau}\in\mathbb{R}^2$denote the joint driving torque, $\boldsymbol{\tau}_{ext}\in\mathbb{R}^2$denote the real-time human-robot interaction torque.$\mathbf{M}(\boldsymbol{\theta})\in\mathbb{R}^{2\times2}$, $\mathbf{C}(\boldsymbol{\theta},\dot{\boldsymbol{\theta}})\in\mathbb{R}^{2\times2}and\mathbf{G}(\boldsymbol{\theta})\in\mathbb{R}^2$ are the symmetric and positive definite inertia matrix, Coriolis matrix and gravity torque in joint space, and the specific forms is shown as follow

$$\mathbf{M}(\boldsymbol{\theta})=\begin{bmatrix} I_{th}+I_{sh}+m_{th}l_{th}^2+m_{sh}a_{th}^2+m_{sh}l_{sh}^2+2m_{sh}a_{th}l_{sh}\cos\theta_2 & I_{sh}+m_{sh}a_{th}l_{sh}\cos\theta_2+m_{sh}l_{sh}^2 \\ I_{sh}+m_{sh}l_{sh}^2+m_{sh}a_{th}l_{sh}\cos\theta_2 & I_{sh}+m_{sh}l_{sh}^2 \end{bmatrix} \tag{2}$$

$$\mathbf{C}(\boldsymbol{\theta},\dot{\boldsymbol{\theta}})=\begin{bmatrix} -2m_{sh}a_{th}l_{sh}\sin\theta_2\dot{\theta}_2 & -m_{sh}a_{th}l_{sh}\sin\theta_2\dot{\theta}_2 \\ m_{sh}a_{th}l_{sh}\sin\theta_2\dot{\theta}_1 & 0 \end{bmatrix} \tag{3}$$

$$\mathbf{G}(\boldsymbol{\theta})=\begin{bmatrix} l_{th}m_{th}g\sin\theta_1+m_{sh}a_{th}g\sin\theta_1+l_{sh}m_{sh}g\sin(\theta_1+\theta_2) \\ l_{sh}m_{sh}g\sin(\theta_1+\theta_2) \end{bmatrix} \tag{4}$$

Furthermore, $\boldsymbol{\tau}_f(\dot{\boldsymbol{\theta}})\in\mathbb{R}^2$ is adopted to describe hip and knee joint friction, which is shown as

$$\boldsymbol{\tau}_f(\dot{\boldsymbol{\theta}})=\begin{bmatrix} k_{1,1}\,\mathrm{sgn}(\dot{\theta}_1)+k_{1,2}\dot{\theta}_1 \\ k_{2,1}\,\mathrm{sgn}(\dot{\theta}_2)+k_{2,2}\dot{\theta}_2 \end{bmatrix} \tag{5}$$

where $k_{1,1}$and $k_{2,1}$ are the coulomb friction coefficient, $k_{1,2}$ and $k_{2,2}$ are the viscous friction coefficient, respectively.

Generally speaking, the minimum inertia parameter from,

$$\mathbf{M}(\boldsymbol{\theta})\ddot{\boldsymbol{\theta}}+\mathbf{C}(\boldsymbol{\theta},\dot{\boldsymbol{\theta}})\dot{\boldsymbol{\theta}}+\mathbf{G}(\boldsymbol{\theta})+\boldsymbol{\tau}_f(\dot{\boldsymbol{\theta}})=\mathbf{Y}(\boldsymbol{\theta},\dot{\boldsymbol{\theta}},\ddot{\boldsymbol{\theta}})\boldsymbol{\Phi} \tag{6}$$

where $\mathbf{Y}\in\mathbb{R}^{2\times8}$ and $\boldsymbol{\Phi}\in\mathbb{R}^8$ denote the regression matrix and unknown parameter vector. Further, according to the dataset, $\boldsymbol{\Phi}$ can be obtained by many algorithms, such as least squares method, ridge regression or heuristic algorithm.

2.2 Linear Extended State Observer Design

In this paper, the nominal values of the parameter vector $\boldsymbol{\Phi}$ are utilized in the linear extended state observer and sliding mode controller designed, which usually is obtained by model parameter identification or generated by CAD software, such as SolidWorks and so on. However, the value of the parameter vector obtained by the above methods is often inaccurate in practice. Meanwhile, external disturbance may also affect the dynamic performance of the exoskeleton system. To address this problem, the LESO is designed to ensure the robustness of the 2-DOF lower limb exoskeleton. Considering the external disturbance , the real dynamic can be described as follow:

$$\mathbf{M}(\boldsymbol{\theta})\ddot{\boldsymbol{\theta}}+\mathbf{C}(\boldsymbol{\theta},\dot{\boldsymbol{\theta}})\dot{\boldsymbol{\theta}}+\mathbf{G}(\boldsymbol{\theta})+\boldsymbol{\tau}_f(\dot{\boldsymbol{\theta}})+\boldsymbol{\tau}_d=\boldsymbol{\tau}+\boldsymbol{\tau}_{ext} \tag{7}$$

Assumption 1: The parameter matrices or vectors $\mathbf{M}(\boldsymbol{\theta})$, $\mathbf{C}(\boldsymbol{\theta},\dot{\boldsymbol{\theta}})$, $\mathbf{G}(\boldsymbol{\theta})$ and $\boldsymbol{\tau}_f(\dot{\boldsymbol{\theta}})$can be expressed as follow:

$$\begin{cases} \mathbf{M}(\boldsymbol{\theta})=\mathbf{M}_0(\boldsymbol{\theta})+\mathbf{M}_\Delta(\boldsymbol{\theta}), & \mathbf{C}(\boldsymbol{\theta},\dot{\boldsymbol{\theta}})=\mathbf{C}_0(\boldsymbol{\theta},\dot{\boldsymbol{\theta}})+\mathbf{C}_\Delta(\boldsymbol{\theta},\dot{\boldsymbol{\theta}}), \\ \mathbf{G}(\boldsymbol{\theta})=\mathbf{G}_0(\dot{\boldsymbol{\theta}})+\mathbf{G}_\Delta(\boldsymbol{\theta}), & \boldsymbol{\tau}_f(\dot{\boldsymbol{\theta}})=\boldsymbol{\tau}_{f,0}(\dot{\boldsymbol{\theta}})+\boldsymbol{\tau}_{f,\Delta}(\dot{\boldsymbol{\theta}}). \end{cases} \tag{8}$$

where $\mathbf{M}_0(\boldsymbol{\theta})$, $\mathbf{C}_0(\boldsymbol{\theta},\dot{\boldsymbol{\theta}})$, $\mathbf{G}_0(\boldsymbol{\theta})$ and $\boldsymbol{\tau}_{f,0}(\dot{\boldsymbol{\theta}})$ are the nominal and known matrices and vectors, and $\mathbf{M}_0(\boldsymbol{\theta})$ is the symmetric and positive definite matrices. Meanwhile, the $\mathbf{M}_\Delta(\boldsymbol{\theta})$, $\mathbf{C}_\Delta(\boldsymbol{\theta},\dot{\boldsymbol{\theta}})$, $\mathbf{G}_\Delta(\boldsymbol{\theta})$ and $\boldsymbol{\tau}_{f,\Delta}(\dot{\boldsymbol{\theta}})$ are the unknown matrices.

Hence, (8) can be rewritten as

$$\mathbf{M}_0(\boldsymbol{\theta})\ddot{\boldsymbol{\theta}}+\mathbf{C}_0(\boldsymbol{\theta},\dot{\boldsymbol{\theta}})\dot{\boldsymbol{\theta}}+\mathbf{G}_0(\boldsymbol{\theta})+\boldsymbol{\tau}_{f,0}(\dot{\boldsymbol{\theta}})+\Delta=\boldsymbol{\tau}+\boldsymbol{\tau}_{ext} \tag{9}$$

where the error Δ denotes the lumped uncertainty, which is defined as

$$\Delta=\mathbf{M}_\Delta(\boldsymbol{\theta})\ddot{\boldsymbol{\theta}}+\mathbf{C}_\Delta(\boldsymbol{\theta},\dot{\boldsymbol{\theta}})\dot{\boldsymbol{\theta}}+\mathbf{G}_\Delta(\boldsymbol{\theta})+\boldsymbol{\tau}_{f,\Delta}(\dot{\boldsymbol{\theta}})+\boldsymbol{\tau}_d \tag{10}$$

For the 2-DOF lower limb exoskeleton system, defined state variables as $\mathbf{x}=[\mathbf{x}_1,\mathbf{x}_2]^T=[\boldsymbol{\theta},\dot{\boldsymbol{\theta}}]$. Consequently, the corresponding state space model is expressed as follow

$$\begin{cases} \dot{\mathbf{x}}_1=\mathbf{x}_2 \\ \dot{\mathbf{x}}_2=\mathbf{M}_0^{-1}\left(\boldsymbol{\tau}+\boldsymbol{\tau}_{ext}-\mathbf{C}_0\mathbf{x}_2-\mathbf{G}_0-\boldsymbol{\tau}_{f,0}\right)-\mathbf{M}_0^{-1}\Delta \end{cases} \tag{11}$$

In order to accomplish the design missions discussed in Section 2.1, the addition lumped uncertainty $\mathbf{M}_0^{-1}\boldsymbol{\Delta}$ is extended as an additional state variable. Then, the extended state space model can be written as

$$\begin{cases}\dot{\mathbf{x}}_1 = \mathbf{x}_2 \\ \dot{\mathbf{x}}_2 = \mathbf{M}_0^{-1}\left(\boldsymbol{\tau} + \boldsymbol{\tau}_{ext} - \boldsymbol{\varphi}(\mathbf{x}) - \mathbf{G}_0\right) - \mathbf{x}_3 \\ \dot{\mathbf{x}}_3 = \boldsymbol{\delta}(t)\end{cases} \tag{12}$$

where $\boldsymbol{\delta}(t)$ represent the time derivative of the state variable $\mathbf{x}_3$,$\boldsymbol{\varphi}(\mathbf{x}) = \mathbf{C}_0\mathbf{x}_2 + \boldsymbol{\tau}_f$.

Assumption 2: The function $\boldsymbol{\varphi}(\mathbf{x})$ is global Lipschitz with respecting to $\mathbf{x}_2$ in its practical range; and addition lumped uncertainty $\boldsymbol{\Delta}$and its time derivative $\dot{\boldsymbol{\Delta}}$ are both bounded.

The mission target of the LESO is not only observing the unmeasured state variable $\mathbf{x}_2$but also the estimating the lumped uncertainty state variable $\mathbf{x}_3$ for controller compensation in real time and to guarantee the robustness and dynamic performance of the system.

In this paper, $\hat{\mathbf{x}}_i$(i=1,2,3) denotes the estimate value of state $\mathbf{x}$, and $\tilde{\mathbf{x}}_i = \mathbf{x}_i - \hat{\mathbf{x}}_i$ denotes the estimate error for the i-th state. We rewrite the extended state space model (12) as

$$\dot{\mathbf{x}} = \mathbf{A}_0\mathbf{x} + \mathbf{B}_0\mathbf{u} - \boldsymbol{\Phi}(\mathbf{x}) + \mathbf{D}(t) \tag{13}$$

where

$$\mathbf{A}_0 = \begin{bmatrix}\mathbf{0}_{2\times2} & \mathbf{I}_{2\times2} & \mathbf{0}_{2\times2} \\ \mathbf{0}_{2\times2} & \mathbf{0}_{2\times2} & \mathbf{I}_{2\times2} \\ \mathbf{0}_{2\times2} & \mathbf{0}_{2\times2} & \mathbf{0}_{2\times2}\end{bmatrix},\quad \mathbf{B}_0 = \begin{bmatrix}\mathbf{0}_{2\times2} \\ \mathbf{M}_0^{-1}(\mathbf{x}) \\ \mathbf{0}_{2\times2}\end{bmatrix},\quad \boldsymbol{\Phi}(\mathbf{x}) = \begin{bmatrix}\mathbf{0}_{2\times1} \\ \boldsymbol{\varphi}(\mathbf{x}) \\ \mathbf{0}_{2\times1}\end{bmatrix},\quad \mathbf{D}(t) = \begin{bmatrix}\mathbf{0}_{2\times1} \\ \mathbf{0}_{2\times1} \\ \boldsymbol{\delta}(t)\end{bmatrix},$$

$\mathbf{I}_{2\times2}$ presents a unit matrix with the size of $^{\boldsymbol{\nu}}{}_{2\times2}$, and $\mathbf{0}_{2\times2}$ presents a zero unit matrix with the size of 2×2.

Then, corresponding LESO model is designed as follows

$$\dot{\hat{\mathbf{x}}} = \mathbf{A}_0\hat{\mathbf{x}} + \mathbf{B}_0\mathbf{u} - \hat{\boldsymbol{\Phi}}(\mathbf{x}) + \mathbf{H}(\mathbf{x}_1 - \hat{\mathbf{x}}_1) \tag{14}$$

where $\hat{\boldsymbol{\Phi}}(\mathbf{x})=\boldsymbol{\Phi}(\mathbf{x}_1,\mathbf{x}_2) - \boldsymbol{\Phi}(\mathbf{x}_1,\hat{\mathbf{x}}_2)$ denotes the estimate error, $\mathbf{H}=[3\omega_0\ 3\omega_0^2\ \omega_0^3]^T$, which $\mathbf{H}$ is the observer gain, $\tilde{\mathbf{X}}$ denotes the a type of observer tuning gain, which is selected as a positive parameter.

Subtract (14) from (13), the state space model of $\tilde{\mathbf{x}}$ is shown as follow

$$\dot{\tilde{\mathbf{x}}} = \mathbf{A}_0\tilde{\mathbf{x}} - \tilde{\boldsymbol{\Phi}}(\mathbf{x}) + \mathbf{D}(t) - \mathbf{H}(\mathbf{x}_1 - \hat{\mathbf{x}}_1) \tag{15}$$

Let $\boldsymbol{\varepsilon}_1 = \tilde{\mathbf{x}}_1$, $\boldsymbol{\varepsilon}_2 = \tilde{\mathbf{x}}_2/\omega_0$, and $\boldsymbol{\varepsilon}_2 = \tilde{\mathbf{x}}_3/\omega_0^2$ denote the scaled estimation error, then (15) can be rewritten as

$$\dot{\boldsymbol{\varepsilon}} = \omega_0\mathbf{A}\boldsymbol{\varepsilon} - \mathbf{B}_2\frac{\mathbf{M}_0^{-1}\tilde{\boldsymbol{\varphi}}(\mathbf{x})}{\omega_0} + \mathbf{B}_3\frac{\boldsymbol{\delta}(t)}{\omega_0^2}, \tag{16}$$

$$\mathbf{A} = \begin{bmatrix}-3*\mathbf{I}_{2\times2} & \mathbf{I}_{2\times2} & \mathbf{0}_{2\times2} \\ -3*\mathbf{I}_{2\times2} & \mathbf{0}_{2\times2} & \mathbf{I}_{2\times2} \\ -\mathbf{I}_{2\times2} & \mathbf{0}_{2\times2} & \mathbf{0}_{2\times2}\end{bmatrix},\quad \mathbf{B}_3 = \begin{bmatrix}\mathbf{0}_{2\times2} \\ \mathbf{0}_{2\times2} \\ \mathbf{I}_{2\times2}\end{bmatrix},\quad \mathbf{B}_3 = \begin{bmatrix}\mathbf{0}_{2\times2} \\ \mathbf{0}_{2\times2} \\ \mathbf{I}_{2\times2}\end{bmatrix}$$

where the , and $\boldsymbol{\varepsilon} = [\boldsymbol{\varepsilon}_1\ \boldsymbol{\varepsilon}_2\ \boldsymbol{\varepsilon}_3]^T$.

Obviously, matrix $\mathbf{A}$ is Hurwitz. Hence, there exists a positive definite matrix $\mathbf{P}$ satisfying below qualification.

$$\mathbf{A}^T\mathbf{P} + \mathbf{P}\mathbf{A} = -2*\mathbf{I} \tag{17}$$

Theorem 1: For the LESO (14), when the **Assumption 2** hold, the state estimation errors will reach and stay in a predefined region with the appropriate constant ω_0.

Proof of Theorem 1: For the LESO (14), considering the following positive definite Lyapunov function:

$$\mathbf{V}_O = \boldsymbol{\varepsilon}^T\mathbf{P}\boldsymbol{\varepsilon} \tag{18}$$

Then, the time derivative of $\mathbf{V}_O$is

$$\begin{aligned}\dot{\mathbf{V}}_O &= \dot{\boldsymbol{\varepsilon}}^T\mathbf{P}\boldsymbol{\varepsilon} + \boldsymbol{\varepsilon}^T\mathbf{P}\dot{\boldsymbol{\varepsilon}} \\ &= \left(\omega_0\mathbf{A}\boldsymbol{\varepsilon} - \mathbf{B}_2\frac{\mathbf{M}_0^{-1}\tilde{\boldsymbol{\varphi}}(\mathbf{x})}{\omega_0} + \mathbf{B}_3\frac{\boldsymbol{\delta}(t)}{\omega_0^2}\right)^T\mathbf{P}\boldsymbol{\varepsilon} + \boldsymbol{\varepsilon}^T\mathbf{P}\left(\omega_0\mathbf{A}\boldsymbol{\varepsilon} - \mathbf{B}_2\frac{\mathbf{M}_0^{-1}\tilde{\boldsymbol{\varphi}}(\mathbf{x})}{\omega_0} + \mathbf{B}_3\frac{\boldsymbol{\delta}(t)}{\omega_0^2}\right) \\ &= \omega_0\left(\boldsymbol{\varepsilon}^T\mathbf{A}^T\mathbf{P}\boldsymbol{\varepsilon} + \boldsymbol{\varepsilon}^T\mathbf{P}\mathbf{A}\boldsymbol{\varepsilon}\right) + \left(-\mathbf{B}_2\frac{\mathbf{M}_0^{-1}\tilde{\boldsymbol{\varphi}}(\mathbf{x})}{\omega_0} + \mathbf{B}_3\frac{\boldsymbol{\delta}(t)}{\omega_0^2}\right)^T\mathbf{P}\boldsymbol{\varepsilon} + \boldsymbol{\varepsilon}^T\mathbf{P}\left(-\mathbf{B}_2\frac{\mathbf{M}_0^{-1}\tilde{\boldsymbol{\varphi}}(\mathbf{x})}{\omega_0} + \mathbf{B}_3\frac{\boldsymbol{\delta}(t)}{\omega_0^2}\right)\end{aligned} \tag{19}$$

Based on **Assumption 2**, the condition $\left|\tilde{\boldsymbol{\varphi}}(\mathbf{x})\right| \le \kappa\left\|\boldsymbol{\varepsilon}\right\|$ hold, and (19) can be rewritten as

$$\dot{\mathbf{V}}_O \le \left(-2\omega_0 + 2\frac{\lambda_1\kappa}{\omega_0}\left\|\mathbf{M}_0^{-1}\right\|\right)\left\|\boldsymbol{\varepsilon}\right\|^2 + 2\frac{\lambda_2}{\omega_0^2}\left|\boldsymbol{\delta}(t)\right|\left\|\boldsymbol{\varepsilon}\right\| \tag{20}$$

where $\lambda_i = \left\|\mathbf{P}\mathbf{B}_i\right\|, \mathbf{i} = 2,3$.

The time derivative of the Lyapunov function (19) is a negative function when (20) is established.

$$\left\|\boldsymbol{\varepsilon}\right\| \ge \frac{\lambda_2\left|\boldsymbol{\delta}(t)\right|}{\omega_0\left(\omega_0^2 - \lambda_1\kappa\left\|\mathbf{M}_0^{-1}\right\|\right)} \tag{21}$$

Considering (21), when the bandwidth $\boldsymbol{\omega}_0$ is big enough, the estimation error $\left\|\boldsymbol{\varepsilon}\right\|$ can quickly converge to a smaller range, which is acceptable in practical applications.

2.3 Robust Sliding Mode Controller Design

In this section, the robust sliding mode controller is adopted based on LESO (14) to ensure the robustness and dynamic performance of the 2-DOF lower limb exoskeleton. For the system state space model (11) and (12), let $\mathbf{x}_r$ express the desired trajectory. Obviously, the objective is to make the tracking error $\mathbf{e}=\mathbf{x}-\mathbf{x}_r$ converge to zero.

Define an auxiliary sliding mode error $\mathbf{s} \in \square^2$ as

$$\mathbf{s} = \dot{\mathbf{e}} + \boldsymbol{\alpha}\mathbf{e} \tag{22}$$

with $\boldsymbol{\alpha} \in \mathbb{R}^{2\times2}$ being a diagonal matrix with positive diagonal element. Then, substituting (11), the time derivative of $\mathbf{s}$ can be shown as

$$\begin{aligned}\dot{\mathbf{s}} &= \ddot{\mathbf{e}} + \boldsymbol{\alpha}\dot{\mathbf{e}} \\ &= \mathbf{M}_0^{-1}\left(\boldsymbol{\tau} + \boldsymbol{\tau}_{ext} - \mathbf{C}_0\mathbf{x}_2 - \mathbf{G}_0 - \boldsymbol{\tau}_{f,0}\right) - \mathbf{M}_0^{-1}\boldsymbol{\Delta} - \ddot{\mathbf{x}}_r + \boldsymbol{\alpha}\left(\mathbf{x}_1 - \ddot{\mathbf{x}}_r\right)\end{aligned} \tag{23}$$

Design a sliding mode tracking controller $\boldsymbol{\tau}$ as

$$\boldsymbol{\tau} = -\mathbf{M}_0\mathbf{K}\mathbf{s} - \boldsymbol{\tau}_{ext} + \mathbf{G}_0 + \boldsymbol{\varphi}(\mathbf{x}) + \boldsymbol{\Delta} + \mathbf{M}_0\ddot{\mathbf{x}}_r - \mathbf{M}\boldsymbol{\alpha}\left(\mathbf{x}_1 - \ddot{\mathbf{x}}_r\right) \tag{24}$$

where $\mathbf{K}$ is the designed positive control gain. $\boldsymbol{\varphi}(\mathbf{x})$ is defined in Section 2.2.

Since value of lumped uncertainty $\boldsymbol{\Delta}$ is unknown and real-time joint angular velocity $\mathbf{x}_2$ is unmeasurable, based on the LESO (14), the robust sliding mode controller is redesigned as

$$\boldsymbol{\tau} = -\mathbf{M}_0\mathbf{K}\hat{\mathbf{s}} - \boldsymbol{\tau}_{ext} + \mathbf{G}_0 + \hat{\boldsymbol{\varphi}}(\mathbf{x}) + \mathbf{M}_0\hat{\mathbf{x}}_3 + \mathbf{M}_0\ddot{\mathbf{x}}_r - \mathbf{M}\boldsymbol{\alpha}\left(\mathbf{x}_1 - \ddot{\mathbf{x}}_r\right) \tag{25}$$

The total Lyapunov function is defined as

$$\mathbf{V} = \frac{1}{2}\mathbf{s}^T\mathbf{s} + \mathbf{V}_O \tag{26}$$

Substituting (23), and it's time derivative is shown as

$$\begin{aligned}\dot{\mathbf{V}} &= \mathbf{s}^T\dot{\mathbf{s}} + \dot{\mathbf{V}}_O \\ &= \mathbf{s}^T\left[\mathbf{M}_0^{-1}\left(\boldsymbol{\tau} + \boldsymbol{\tau}_{ext} - \boldsymbol{\varphi}(\mathbf{x}) - \mathbf{G}_0\right) - \mathbf{M}_0^{-1}\boldsymbol{\Delta} - \ddot{\mathbf{x}}_r + \boldsymbol{\alpha}\left(\mathbf{x}_1 - \ddot{\mathbf{x}}_r\right)\right] + \dot{\mathbf{V}}_O\end{aligned} \tag{27}$$

Substituting (25) into (27), considering Young's inequality, (27) can be rewritten as

$$\begin{aligned}\dot{\mathbf{V}} &= -\mathbf{s}^T\mathbf{K}\mathbf{s} + \mathbf{s}^T\mathbf{K}\tilde{\mathbf{s}} + \mathbf{s}^T\left[-\mathbf{M}_0^{-1}\tilde{\boldsymbol{\varphi}}(\mathbf{x}) + \tilde{\mathbf{x}}_3 + \boldsymbol{\alpha}\tilde{\mathbf{x}}_2\right] + \dot{\mathbf{V}}_O \\ &= -\mathbf{s}^T\mathbf{K}\mathbf{s} + \mathbf{s}^T\left[(\mathbf{K}+\boldsymbol{\alpha})\tilde{\mathbf{x}}_2 - \mathbf{M}_0^{-1}\tilde{\boldsymbol{\varphi}}(\mathbf{x}) + \tilde{\mathbf{x}}_3\right] + \dot{\mathbf{V}}_O \\ &\le -\mathbf{s}^T\mathbf{K}\mathbf{s} + \mathbf{s}^T\left[(\mathbf{K}+\boldsymbol{\alpha})\tilde{\mathbf{x}}_2 - \mathbf{M}_0^{-1}\tilde{\boldsymbol{\varphi}}(\mathbf{x}) + \tilde{\mathbf{x}}_3\right] + \left(-2\omega_0 + 2\frac{\lambda_1\kappa}{\omega_0}\left\|\mathbf{M}_0^{-1}\right\|\right)\left\|\boldsymbol{\varepsilon}\right\|^2 + 2\frac{\lambda_2}{\omega_0^2}\left|\boldsymbol{\delta}(t)\right|\left\|\boldsymbol{\varepsilon}\right\| \\ &\le -\mathbf{s}^T\left(\mathbf{K} - \frac{1}{2}\mathbf{I}\right)\mathbf{s} + \frac{1}{2}\tilde{\boldsymbol{\Delta}}_{dis}^T\tilde{\boldsymbol{\Delta}}_{dis} + \left(-2\omega_0 + 2\frac{\lambda_1\kappa}{\omega_0}\left\|\mathbf{M}_0^{-1}\right\|\right)\left\|\boldsymbol{\varepsilon}\right\|^2 + 2\frac{\lambda_2}{\omega_0^2}\left|\boldsymbol{\delta}(t)\right|\left\|\boldsymbol{\varepsilon}\right\|\end{aligned} \tag{28}$$

where $\tilde{\boldsymbol{\Delta}}_{dis} = (\mathbf{K}+\boldsymbol{\alpha})\tilde{\mathbf{x}}_2 - \mathbf{M}_0^{-1}\tilde{\boldsymbol{\varphi}}(\mathbf{x}) + \tilde{\mathbf{x}}_3$, which expresses the

lumped estimated error term.

Considering the discussion of LESO (14) in section 2.2 and (28), the amplitude of $\tilde{\boldsymbol{\Delta}}_{\mathbf{dis}}^{\mathbf{T}}\tilde{\boldsymbol{\Delta}}_{\mathbf{dis}}$ is determined by the performance of LESO (14), which is related to the value of parameter $\boldsymbol{\omega}_0$. Meanwhile, the rate of convergence depends on control gain $\mathbf{K}$ and observer bandwidth $\boldsymbol{\omega}_0$. Then, if $\mathbf{K}$ is large enough and $\boldsymbol{\omega}_0$ is big enough, the satisfactory tracking effect can be obtained.

3 Simulation

In order to verify the effectiveness of the proposed robust sliding mode control, the simulation model is built to realize the passive mechanism of exoskeleton by Matlab/Simulink, which is shown in figure 3.

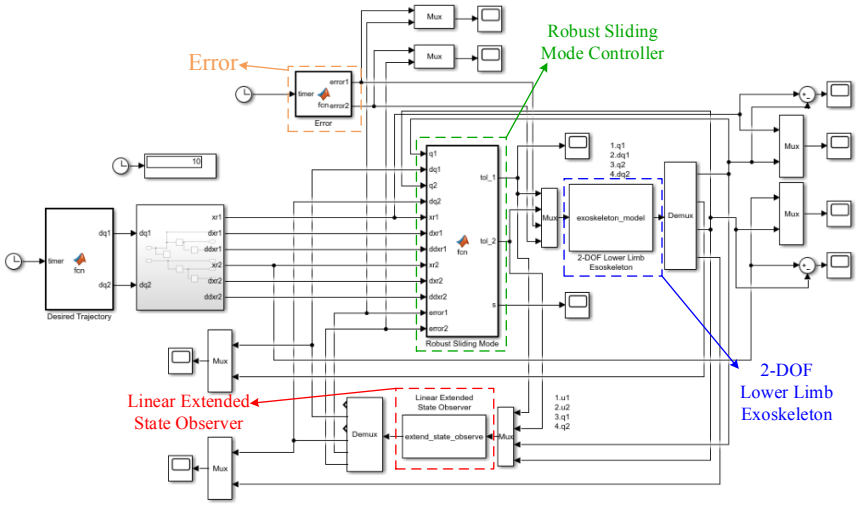

Figure 3 Configuration of the simulation for the 2-DOF lower limb exoskeleton

Then, the dynamic model of 2-DOF lower limb exoskeleton is set as follows

$$\mathbf{M}_0(\boldsymbol{\theta})\ddot{\boldsymbol{\theta}}+\mathbf{C}_0(\boldsymbol{\theta},\dot{\boldsymbol{\theta}})\dot{\boldsymbol{\theta}}+\mathbf{G}_0(\boldsymbol{\theta})+\boldsymbol{\tau}_{\mathbf{f},0}(\dot{\boldsymbol{\theta}})+\Delta=\boldsymbol{\tau}+\boldsymbol{\tau}_{\mathbf{ext}} \tag{29}$$

where, $\mathbf{M}_0=[27.22+3.32\cos\theta_2, 8.28+1.66\cos\theta_2; 8.28+1.66\cos\theta_2, 8.28]$ $\mathbf{C}_0=[-3.32\sin\theta_2\dot{\theta}_2, -1.66\sin\theta_2\dot{\theta}_2; 1.66\sin\theta_2\dot{\theta}_1, 0]$ $\mathbf{G}_0=[41.76\sin(\theta_1+\theta_2)+184.92\sin\theta_1; 41.76\sin(\theta_1+\theta_2)]$, $\boldsymbol{\tau}_{\mathbf{f},0}=[27.81\mathrm{sgn}(\theta_1)+24.09\theta_1; 37.24\mathrm{sgn}(\theta_2)+41.38\theta_2]$ Δ is designed as follow

$$\begin{cases}\Delta_1 = \frac{1}{2}\sin(\frac{3}{2}\pi t);\\ \Delta_2 = \frac{1}{2}\sin(\frac{3}{2}\pi t+\frac{1}{2}\pi);\end{cases} \tag{30}$$

Then, according to the controller (25), the human-robot interaction torque $\boldsymbol{\tau}_{\mathbf{ext}}$ is challenging to design and will be compensated by the controller so $\boldsymbol{\tau}_{\mathbf{ext}}$ is set as 0 in the simulation experiment. Furthermore, the desirable trajectory $\boldsymbol{\theta}_{\mathbf{r}}$ of the exoskeleton is set as the human natural walking gait given by

$$\begin{cases}\theta_{r,1}=\sum_{k=1}^{4}\left(a_{k,1}\sin(k\omega t)+b_{k,1}\cos(k\omega t)\right)+\theta_{0,1};\\ \theta_{r,2}=\sum_{k=1}^{4}\left(a_{k,2}\sin(k\omega t)+b_{k,2}\cos(k\omega t)\right)+\theta_{0,2};\end{cases} \tag{31}$$

where $\omega=0.4\pi$, $b_{k,1}(k=1,2,3,4)$ are -2.874, -2.423, 1.227 and -0.1462, $b_{k,1}(k=1,2,3,4)$ are 18.52, -2.016, -0.3704 and 0.201, $\theta_{0,1}=10.07$, $b_{k,2}(k=1,2,3,4)$ are 17.62, -2.469, -3.82 and -0.1346, $b_{k,2}(k=1,2,3,4)$ are -1.494, 11.72, 1.014 and 0.2165, and $\theta_{0,2}=-17.49$.

With considering the gait trajectory (31), the parameters of robust sliding mode controller are set as $\boldsymbol{\alpha}=\mathrm{diag}\{25,25\}$, $\mathbf{K}=\mathrm{diag}\{1000,1000\}$. Meanwhile, the parameter of LESO is set as $\boldsymbol{\omega}_0=\mathrm{diag}\{1000,1000\}$. Then, in simulation experiment, the simulation step is set as 0.001 sec.

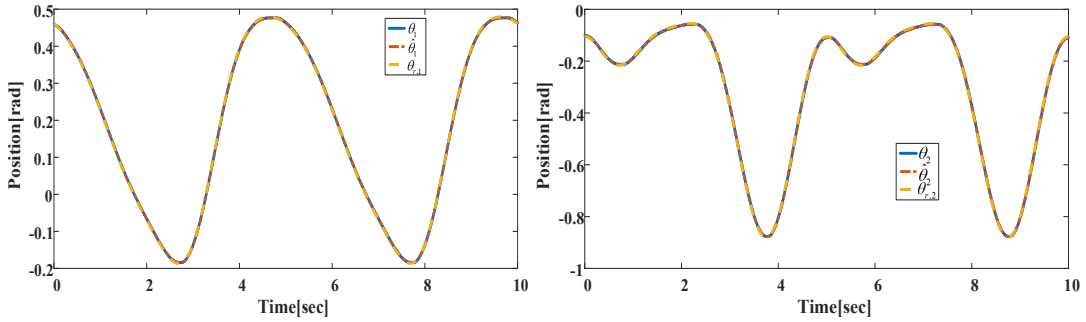

Figure 4 Tracking performance and estimating performance of two joint position trajectories

Figure 4 shows the desired trajectory $\theta_r=[\theta_{r,1},\theta_{r,2}]^T$, estimating trajectory $\hat{\theta}=[\theta_1,\theta_2]^T$, and actual trajectory $|e_i|<3.2\times10^{-3}$ of two joints. Then, the tracking deviation $|e_1|<3.2\times10^{-3}$ and $|e_2|<5.8\times10^{-3}$, and the estimating deviation $|\theta_1-\hat{\theta}_1|<2.4\times10^{-9}$ and $|\theta_2-\hat{\theta}_2|<2.4\times10^{-9}$. It can be seen that the tracking performance of controller and the

estimating performance of the LESO are satisfactory.

Figure 5 shows the setting lumped uncertainty $\boldsymbol{\Delta}=[\Delta_1,\Delta_2]^T$ and estimating lumped uncertainty $\hat{\boldsymbol{\Delta}}=[\hat{\Delta}_1,\hat{\Delta}_2]^T$ of two joints. More specifically, the estimating deviation of lumped uncertainty $|\Delta_1|\le 7.1\times10^{-3}$ and $|\Delta_2|\le 7.2\times10^{-3}$ It can be seen that the lumped uncertainty estimating performance of the LESO are satisfactory.

Figure 6 shows the actual velocity trajectory $\dot{\theta}=[\dot{\theta}_1,\dot{\theta}_2]^T$ and estimating velocity trajectory $\dot{\hat{\theta}}=[\dot{\hat{\theta}}_1,\dot{\hat{\theta}}_2]^T$ of two joints. More specifically, the estimating deviation of $\left|\dot{\theta}_1-\dot{\hat{\theta}}_1\right|<7.07\times10^{-6}$ and $\left|\dot{\theta}_2-\dot{\hat{\theta}}_2\right|<7.07\times10^{-6}$ It can be seen that the velocity deviation estimating performance of the LESO are satisfactory.

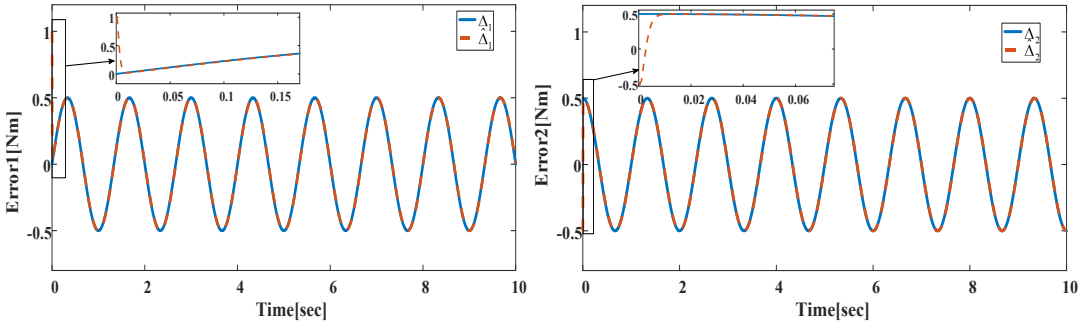

Figure 5 Estimating performance of the lumped uncertainty of two joints

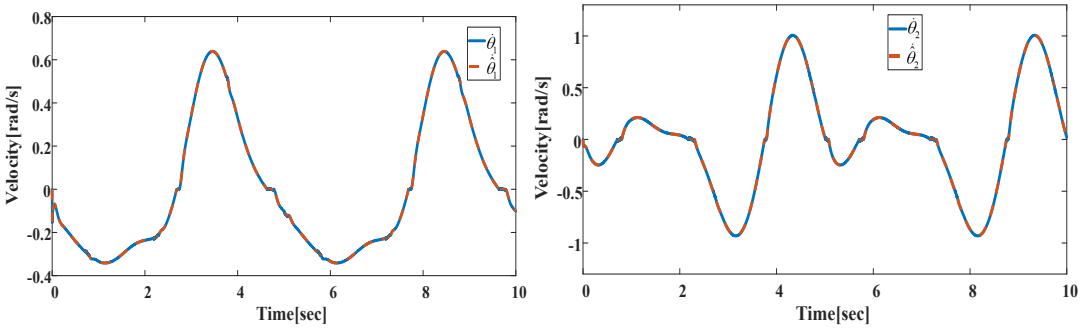

Figure 6 Estimating performance of two joint velocity trajectories

4 Conclusion

In this paper, a LESO-based robust sliding mode controller (25) is designed to improve the robustness and dynamic performance, and the LESO (14) is designed to estimate the unmeasurable state variable and lumped uncertainty consisting of parametric uncertainties, unmodeled dynamics, and external disturbance. For the exoskeleton controller designed, system state estimation and disturbance compensation are adopted to ensure the system's robustness and dynamic performance. For further research plans, the nonlinear ESO will be considered in the exoskeleton controller designed.

Author Contributions: Zhenlei CHEN: Writing draft, Implement, Data verification; Qing GUO: Conceptualization, Methodology; Yao YAN: Result Checking; Dan JIANG: Validation.

Conflict of Interest: The authors declare that they have no competing interests.

Acknowledgments: This work was supported by National Natural Science Foundation of China (No. 51775089 and 11872147), Sichuan Science and Technology Program (No. 2018JY0565 and 2020YFG0137).

References

[1] Li Z, Su C Y, Li G, et al. Fuzzy approximation-based adaptive backstepping control of an exoskeleton for human upper limbs[J]. IEEE Transactions on Fuzzy Systems, 2014, 23(3), 555-566.

[2] Yang Y, Ma L, Huang D. Development and repetitive learning control of lower limb exoskeleton driven by electrohydraulic actuators[J]. IEEE transactions on industrial electronics, 2016, 64(5), 4169-4178.

[3] He W, Li Z, Dong Y, et al. Design and adaptive control for an upper limb robotic exoskeleton in presence of input saturation[J]. IEEE transactions on neural networks and learning systems, 2018, 30(1), 97-108.

[4] Han S, Wang H, Tian Y. A linear discrete-time extended state observer-based intelligent PD controller for a 12 DOFs lower limb exoskeleton LLE-RePA[J]. Mechanical Systems and Signal Processing, 2020, 138, 106547.

[5] Meng W, Liu Q, Zhou Z, et al. Recent development of mechanisms and control strategies for robot-assisted lower limb rehabilitation[J]. Mechatronics, 2015, 31, 132-145.

[6] Hussain S, Xie S Q, Jamwal P K. Robust nonlinear control of an intrinsically compliant robotic gait training orthosis[J]. IEEE Transactions on Systems, Man, and Cybernetics: Systems, 2012, 43(3), 655-665.

[7] Saglia J A, Tsagarakis N G, Dai J S, et al. Control strategies for patient-assisted training using the ankle rehabilitation robot (ARBOT)[J]. IEEE/ASME Transactions on Mechatronics, 2012, 18(6), 1799-1808.

[8] Hogan N. Impedance control: An approach to manipulation. 1984 American control conference. IEEE, 1984, 304-313.

[9] Keemink A Q L, van der Kooij H, Stienen A H A. Admittance control for physical human–robot interaction. The International Journal of Robotics Research, 2018, 37(11), 1421-1444.

[10] Li Z, Huang B, Ye Z, et al. Physical human–robot interaction of a robotic exoskeleton by admittance control[J]. IEEE Transactions on Industrial Electronics, 2018, 65(12), 9614-9624.

[11] Yu X, He W, Li Y, et al. Bayesian Estimation of Human Impedance and Motion Intention for Human-Robot Collaboration. IEEE Transactions on Cybernetics, 2019.

[12] Na J, Ren X, Zheng D. Adaptive control for nonlinear pure-feedback systems with high-order sliding mode observer[J]. IEEE transactions on neural networks and learning systems, 2013, 24(3), 370-382.

[13] Guo B Z, Zhao Z. On the convergence of an extended state observer for nonlinear systems with uncertainty[J]. Systems & Control Letters, 2011, 60(6), 420-430.

[14] Cui R, Chen L, Yang C, et al. Extended state observer-based integral sliding mode control for an underwater robot with unknown disturbances and uncertain nonlinearities[J]. IEEE Transactions on Industrial Electronics, 2017, 64(8), 6785-6795.

[15] Guo Q, Zhang Y, Celler B G, et al. Backstepping control of electro-hydraulic system based on extended-state-observer with plant dynamics largely unknown[J]. IEEE Transactions on industrial Electronics, 2016, 63(11), 6909-6920.

[16] Sun T, Cheng L, Wang W, et al. Semiglobal exponential control of Euler–Lagrange systems using a sliding-mode disturbance observer[J]. Automatica, 2020, 112, 108677.

[17] Siciliano B, Sciavicco L, Villani L, et al. Robotics: modelling, planning and control. Springer Science & Business Media, 2010: 2.

Viser Technology Pte. Ltd.
Mechanical Engineering Science
doi: 10.33142/mes.v2i2.3161

Research Article Open Access

Dynamic optimization analysis of hydraulic pipeline system based on a developed response surface method

Hongquan QU[1], Jianlin SUN[1], Xu YAN[1], Yuanlin ZHANG[1], Xuefeng LIU[1], Tao YU[1*], Huawei HAN[2], Langjun XU[2]

1 School of Electromechanical and Automotive Engineering, Yantai University, Yantai 264005, China
2 Yantai CIMC Raffles Offshore Limited, Yantai 264670, China

***Corresponding Author:** Tao YU, Corresponding address, 30, Qingquan RD, Laishan District, Yantai, China; email address: yutao@ytu.edu.cn*

Abstract:
When designing a complex pipeline with long distance and multi-supports for offshore platform, it is necessary to analyze the vibration characteristics of the complex pipeline system to ensure that there is no harmful resonance in the working conditions. Therefore, the optimal layout of support is an effective method to reduce the vibration response of hydraulic pipeline system. In this paper, a developed dynamic optimization method for the complex pipeline is proposed to investigate the vibration characteristics of complex pipeline with multi-elastic supports. In this method, the Kriging response surface model between the support position and pipeline is established. The position of the clamp in the model is parameterized and the optimal solution of performance index is obtained by genetic algorithm. The number of clamps and the interval between clamps are considered as the constraints of layout optimization, and the optimization objective is the natural frequencies of pipeline. Taking a typical offshore pipeline as example to demonstrate the effectiveness of the proposed method, the results show that the vibration performance of the hydraulic pipeline system is distinctly improved by the optimization procedure, which can provide reasonable guidance for the design of complex hydraulic pipeline system.

Keywords: *Hydraulic pipeline; Multi-Support; Response surface method; Optimization analysis*

1 Introduction

The hydraulic pipeline system is usually employed to transmit power in drilling platform. It has the characteristics of complex configuration, long span and multi-supports. When the pipeline is excited by external mechanical load and internal fluid, the large vibration of the pipeline system occurs, which will directly lead to fatigue failure, displacement deformation, loosening of clamp and fatigue fracture of connecting parts. The design of offshore platform pipeline is of great significance to maintain productivity operation and ensure the safety of the platform. With the deepening of drilling depth, the vibration problem of pipeline system becomes more prominent. The vibration analysis of pipeline is of great significance to the layout of pipeline and the optimization of supports.

The investigation for the dynamic optimization characteristics of pipeline has received extensive attention in recent years. For example, Kwong et al. [1] proposed a novel genetic algorithm to optimize the support position for reducing vibration in hydraulic systems. A simple hydraulic rig was conducted as an example. Numerical and experimental results showed that the significant reductions in vibration was obtained by the optimal support location. Wang et al. [2-3] presented an evolutionary shift method to solve optimization of support positions with a fixed grid mesh, three numerical examples were conducted to demonstrate the effectiveness of the optimization method. In order to avoid dangerous forced vibrations or resonance, the clamp numbers and locations of a pipe-joint system were optimized by Liu et al [4]. The results showed that the optimized pipe-joint system has better anti-vibration ability. Li et al. [5] presented a chaotic swarm particle optimization algorithm to determine optimal clamp locations for hydraulic pipelines in aircraft. Results showed that the value of objective function was decreased by 77.67% compared to the original system by optimal clamp locations. The global sensitivity analysis based on the Sobol method was presented to determine the influence of clamp position on the natural frequency of pipeline system. The simulation and experiment results showed that the proposed optimization method can reduce the vibration of the pipeline system significantly. [6]

From the reviewed references, the current optimization method is time-consuming for the global optimal solution of long span pipeline. A popular approach for global optimization is proposed in which the simulation model generates data for the construction of simpler model as a source of computer experiment. The early research about the response surface method is proposed to improve the calculation optimization efficiency [7]. In recent years, the response surface method has been applied in many fields [8–20]. For example, Xiao et al. [8] proposed response surface method to study the effects of the different content of Si_3N_4 particles in the plating solution. Zhang et al. [9] presented the response surface method to solve the problem of slope stability. Xue et al. [16] proposed the improved response surface method to solve the various related deck landing parameters on sinking velocity for carrier-based aircraft. In order to improve the calculation efficiency of the vibration characteristics of turbine blade disharmony, an improved substructure mode synthesis method based on the extreme response surface method is proposed by Bai et al. [18]. Su et al. [19] proposed a response surface method to study the fatigue reliability for metal dual inline packages under random vibration. Considering the integrality and locality of long span and multi-elastic support of pipelines on offshore platforms, the response surface method can be used to optimize the support locations for hydraulic pipeline system.

To the author's best knowledge, there is almost no literature reporting on the response surface method for the design optimization of hydraulic pipelines with support. As a promising global optimization method, it is the first time to investigate the dynamic optimization analysis of hydraulic pipeline system with multi-supports. Firstly, the method of mathematical statistics combined with pipeline dynamics analysis was adopted to analyze the influence of the clamps layout. Then the developed response surface method is used to establish the optimization model. By simulating the implicit relation between variables and performance indexes, the optimal solution of performance indexes is obtained by genetic algorithm. Taking a typical offshore pipeline as an example to demonstrate the effectiveness of the presented method, an optimization procedure for pipeline is conducted. The dynamic optimization process for complex pipeline with multi-elastic supports are discussed further.

2 Optimization method

The mathematical equation of design variables and response quantities can be expressed as:

$$g(x) = y + \varepsilon = f(x_1, x_2, x_3 \cdots x_n) + \varepsilon \tag{1}$$

where g(x) is the amount of response, y is the function of objective and ε is the fitting error between g(x) and y.

The multi-level function relations can be written as:

$$\tilde{y} = \alpha_0 + \sum_{j=1}^{n} \alpha_j x_j + \sum_{j=n+1}^{2n} \alpha_j x_{j-k}^2 + \sum_{i=1}^{n-1} \sum_{j=i+1}^{n} \alpha_{ij} x_i x_j \tag{2}$$

where n is the number of design variable, α_0 is the undetermined constant term, α_j is the undetermined coefficient of the linear term, and α_{ij} is the undetermined coefficient of the quadratic term.

By variable transformation, the equation (2) can be expressed as:

$$\begin{cases} x_0 = 1 \\ x_1 = x_1, x_2 = x_2, \cdots x_n = x_n \\ x_{n+1} = x_1^2, x_{n+2} = x_2^2, \cdots x_{2n} = x_n^2 \\ x_{2n+1} = x_1, x_{2n+1} = x_1, \cdots x_{k-1} = x_{n-1} x_n \end{cases} \tag{3}$$

$$\begin{cases} \beta_0 = \alpha_0 \\ \beta_1 = \alpha_1, \beta_2 = \alpha_2, \cdots \beta_n = \alpha_n \\ \beta_{n+1} = \alpha_{n+1}, \beta_{n+2} = \alpha_{n+2}, \cdots \beta_{2n} = \alpha_{2n} \\ \beta_{2n+1} = \alpha_{12}, \beta_{2n+2} = \alpha_{13}, \cdots \beta_{k-1} = \alpha_{(n-1)n} \end{cases} \tag{4}$$

By substituting equation (3) and equation (4) into equation (2), it can be obtained:

$$\tilde{y} = \beta_0 + \sum_{i=1}^{k-1} \beta_i \alpha_i \tag{5}$$

The response of the corresponding matrix can be expressed as:

$$\begin{bmatrix} y_1 \\ y_2 \\ \vdots \\ y_n \end{bmatrix} = \begin{bmatrix} 1 & x_{11} & x_{21} & \cdots & x_{n1} \\ 1 & x_{12} & x_{22} & \cdots & x_{n2} \\ \vdots & \vdots & \vdots & \cdots & \cdots \\ 1 & x_{1k} & x_{2k} & \cdots & x_{nk} \end{bmatrix} \begin{bmatrix} \beta_0 \\ \beta_1 \\ \vdots \\ \beta_n \end{bmatrix} + \begin{bmatrix} \varepsilon_0 \\ \varepsilon_1 \\ \vdots \\ \varepsilon_n \end{bmatrix} \tag{6}$$

In order to obtain the response surface with the smallest error. The least-square method is used which can be expressed as:

$$s(\beta) = \sum_{j=1}^{m} \varepsilon_j^2 = \sum_{j=1}^{m} (\sum_{i=0}^{k-1} \beta_i x_i^{(j)} - y^{(j)})^2 \tag{7}$$

The minimum value can be expressed as:

$$\frac{\partial S}{\partial \beta_i} = 2 \sum_{j=1}^{m} \left(x_i^{(j)} \left(\sum_{i=0}^{k-1} \beta_i \alpha_i - y^{(j)} \right) \right) = 0 (l = 0, \cdots, k-1) \tag{8}$$

The equation (8) can be written as the matrix form:

$$\left(X\beta - y \right)^T X = 0 \tag{9}$$

The response surface model can be obtained by calculating β.

The satisfaction function of MOGA genetic algorithm is usually used to optimize multiple objectives. The multi-objective optimization is to find the compromise optimal solution by considering each objective synthetically in the constraint region. A multi-objective optimization problem without losing generality has n decision variables and m objective variables which can be expressed as:

$$\begin{cases} \min y = F(x) = \{ f_1(x), f_2(x), f_3(x), \cdots, f_m(x) \} \\ s.t. g_i(x) \le 0, i = 1, 2, \cdots, l \\ h_{j(x)} = 0, j = 1, 2, \cdots, k \end{cases} \tag{10}$$

Where x is n-dimensional decision vector, y=F(x) is the target vector of m dimension. l is the constraints of inequalities, k is equality constraints.

Pareto optimal solution can be defined as Ps. The surface composed of the target vectors corresponding to all Pareto optimal solutions can be written as P_F:

$$P_F = \left\{ F(x^*) = (f_1(x^*), f_2(x^*), f_3(x^*), \cdots, f_m(x^*))^T \mid x^* \in P_S \right\} \tag{11}$$

In order obtain the real surface, Box-Behnken design (BBD) scheme is the most potent screening design method in response surface optimization. In this method, the selecting points from the three-level factorial arrangement can obtain the efficient estimation of coefficients of the mathematical model. The distribution of three-level full factorial design is illustrated in figure 1.

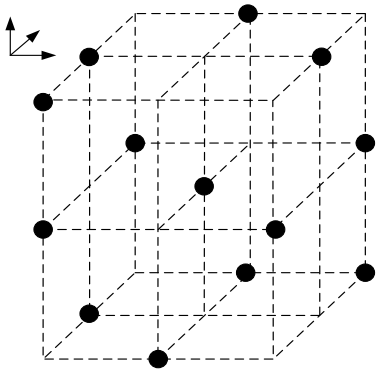

Figure 1 Distribution of three-level full factorial design [20]

3 Design and optimization of response surface method

For the optimizing support locations of pipeline system, the optimization objective should be determined firstly. The pump fluid fluctuation can induce serious pipeline vibration and cause pipeline failure. The pump fluid fluctuation frequency is 275 Hz by test in offshore platform. So the natural frequency of pipeline should be far away from the excited frequency 275Hz. Therefore, in order to avoid the pipeline mechanical resonance, the optimization objective is to avoid the resonance of the natural frequency of the pipeline system.

As shown in figure 2. The pipeline system consists three clamps, the vibration characteristics of pipeline has been analyzed, and the modal shapes have been obtained. The parameterization of pipeline system is shown in Table 1.

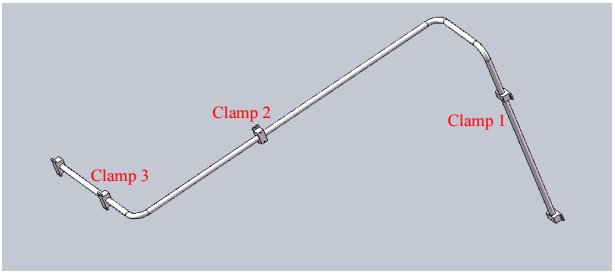

Figure 2 Diagram of piping system

Table 1 Parameterization of pipeline system

size	Numerical value	Estimate
DS_D1@distance 1	1200mm	1200mm
DS_D1@distance 2	1500mm	1500mm
DS_D1@distance 3	400mm	400mm

In order to optimize the clamp position of the pipeline system, the modal analysis for the pipeline system has been conducted to obtain the natural frequency of the pipeline system. The geometric parameter of the selected pipeline is shown in Table 2.

Table 2 Parameter of the pipeline

Designation	Symbol	Unit	Numerical
Elastic modulus	E	Pa	2.06×1011
Density	ρ	kg/m^3	7.9×103
Poisson's ratio	μ	-	0.3
Total length of pipeline	l	m	4.5
outer diameter	r1	m	0.04
inner diameter	r2	m	0.036

As shown in Figure 3. The 10th order natural frequency of the pipeline is 254.9 Hz and the 11th order natural frequency of the pipeline is 285.58 Hz. The test design table is obtained by the BBD scheme, respectively.

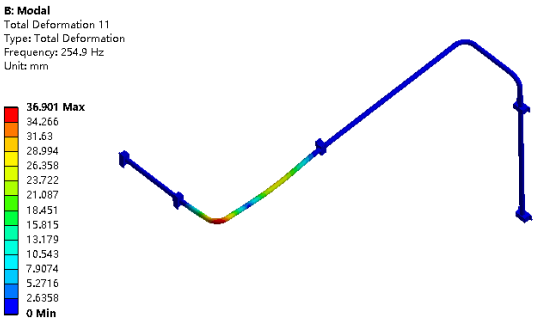

(a) 10th order natural frequency

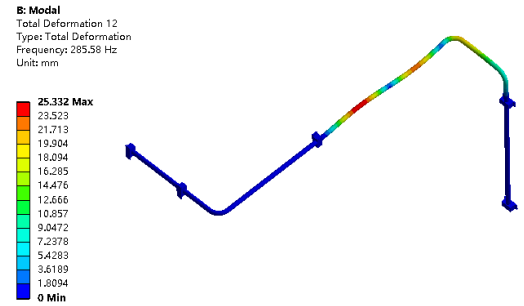

(b) 11th order natural frequency

Figure 3 Natural frequencies and mode shapes of pipeline system

The optimization process of pipeline system is shown in figure 4. As can be seen from figure 4. The parametric modeling should be established firstly, it consists of the variable scope, test design and sample point. Then the dynamic analysis of the pipeline has been conducted and the optimization objective can be obtained. The test design table can be established and the response surface model can be obtained. Finally, optimal solution for pipeline supports can be obtained by optimizing the parameters.

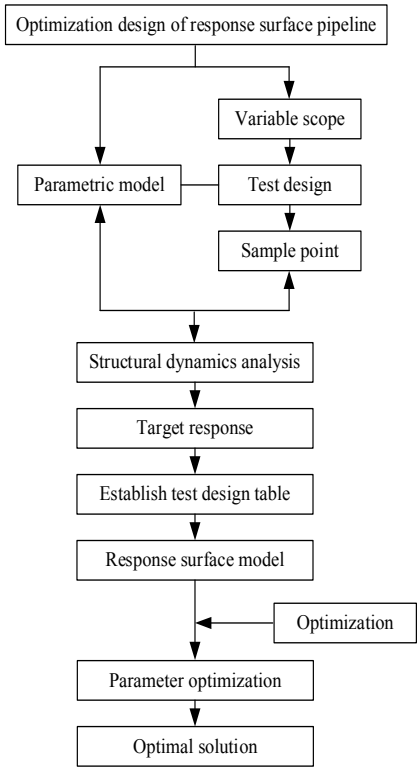

Figure 4 Optimization flow chart of response surface method

4 Test design table and response surface modelling

4.1 Test design table

In this section, the natural frequencies of pipeline are defined as the optimized response value, the Kriging response surface model of the clamp position is established, and the optimization position of the clamp position is obtained by the candidate points. The position of the clamp in the model is parameterized in the modeling software, and the design variables are shown in figure 5. The model is imported into the finite element analysis software, and modal analysis has been conducted. The maximum deformation is taken as the response target value. Using the BBD scheme, the change intervals of design variables are shown in Table 1, and the combination relationship of design variables are shown in Table 3 and Table 4, respectively.

According to the dynamic analysis of the design variable data listed in Table 2 and Table 3, the numerical change of the natural frequency of the pipeline can be obtained. The results are shown in Table 5. The P4 and P5 values in Table 5 are the basis parameters for establishing the response surface model.

Table 3 Change range of BBD variable

	Lower limit	Upper limit	Original size
distance 1/mm	1080	1320	1200
distance 2/mm	1350	1650	1500
distance 3/mm	360	440	400

Table 4 BBD test plan

1	Test number	P1-distance 1	P2- distance 2	P3- distance 3
2	1	1200	1500	400
3	2	1080	1500	360
4	3	1320	1500	360
5	4	1080	1500	440
6	5	1320	1500	440
7	6	1080	1350	400
8	7	1320	1350	400
9	8	1080	1650	400
10	9	1320	1650	400
11	10	1200	1350	360
12	11	1200	1350	440
13	12	1200	1650	360
14	13	1200	1650	440

Table 5 BBD test design table

1	Test number	P1-distance1	P2- distance2	P3- distance3	P4- 10th fixed frequency	P5- 11th fixed frequency
2	1	1200	1500	400	254.9	285.58
3	2	1080	1500	360	277.29	278.65
4	3	1320	1500	360	277.25	352.54
5	4	1080	1500	440	242.32	277.83
6	5	1320	1500	440	268.20	349.91
7	6	1080	1350	400	215.54	329.92
8	7	1320	1350	400	311.28	363.11
9	8	1080	1650	400	242.57	244.68
10	9	1320	1650	400	315.27	326.73
11	10	1200	1350	360	238.02	335.80
12	11	1200	1350	440	237.56	337.58
13	12	1200	1650	360	248.80	272.46
14	13	1200	1650	440	247.60	272.25

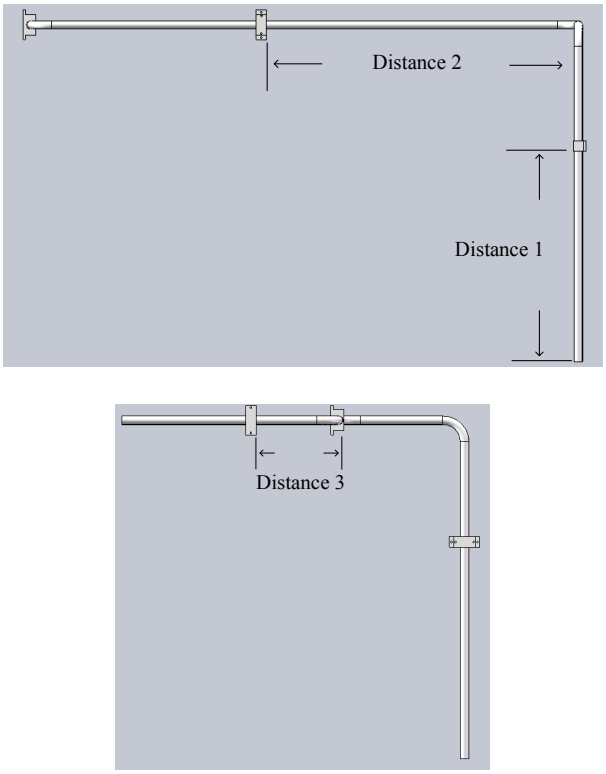

Figure 5 Design variables

4.2 Response surface modeling

According to the experimental design table, the response surface model type of the BBD scheme is defined as Kriging response surface. The Kriging method is used to solve the problem of error estimation. It is a spatial estimation technique of interpolation algorithm, and the fitting degree the sample points of the Kriging response surface and the predicted straight line is shown in figure 6. The real values of P4 and P5 can match closely with the predicted values, and the established response surface model can meet the optimization requirement.

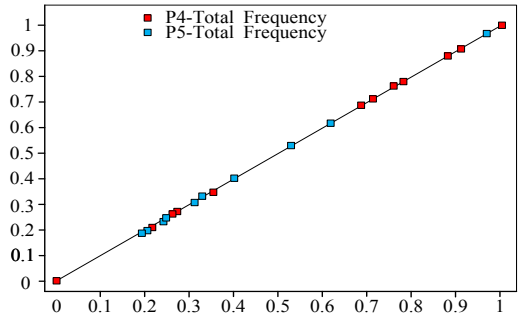

Figure 6 The fitting degree of the sample points of the Kriging response surface and the predicted straight line

The response surface model obtained by the BBD scheme is analyzed, as shown in figure 7. figure 7(a) is the response surface models of distance P1 and distance P2 with response target P4, figure 7(b) is the distance P1 and distance P3 with response target P4, figure 7(c) is the distance P2 and distance P3 with response target P4. Figure 7 (d) is the response surface models of distance P1 and distance P2 and response target P5. Figure 7 (e) is the distance P1 and distance P3 and response target P5. Figure 7 (f) is the distance P2 and distance P3 and response target P5.

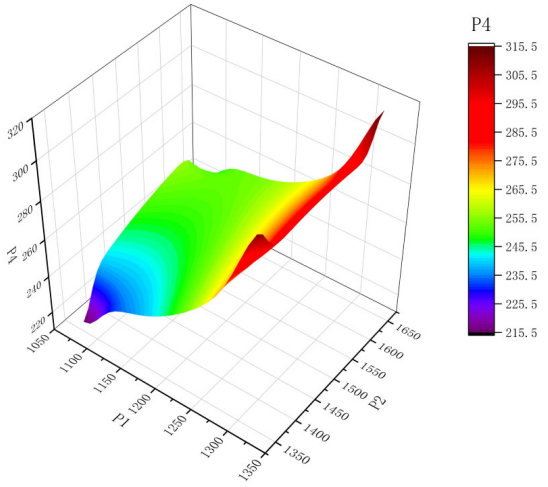

(a) P1-P2-P4 response surface model

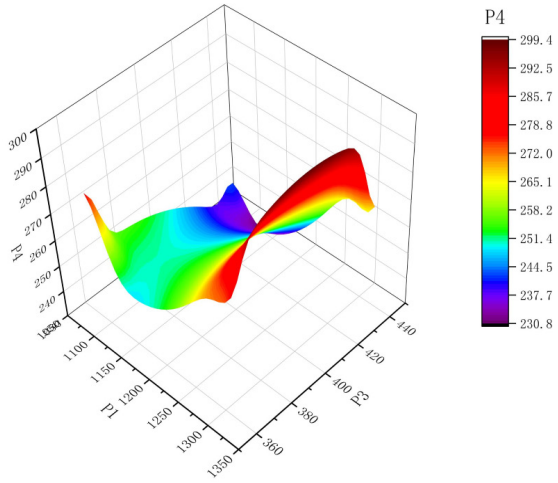

(b) P1-P3-P4 response surface model

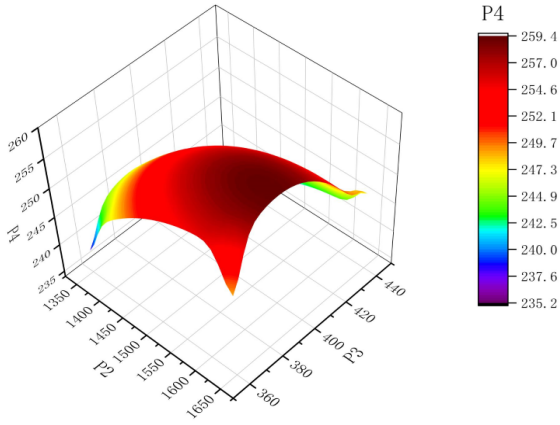

(c) P2-P3-P4 response surface model

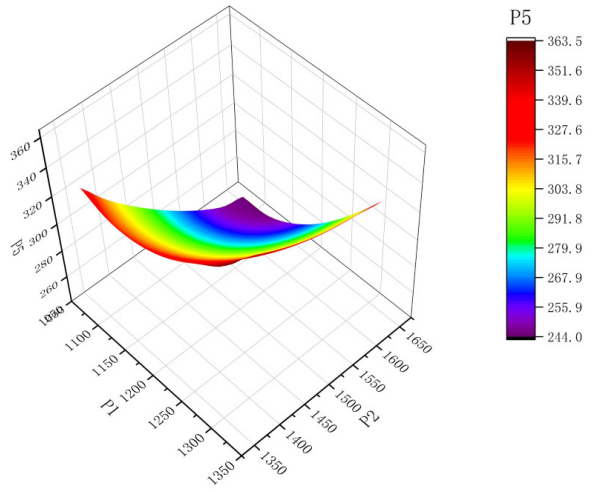

(d) P1-P2-P5 response surface model

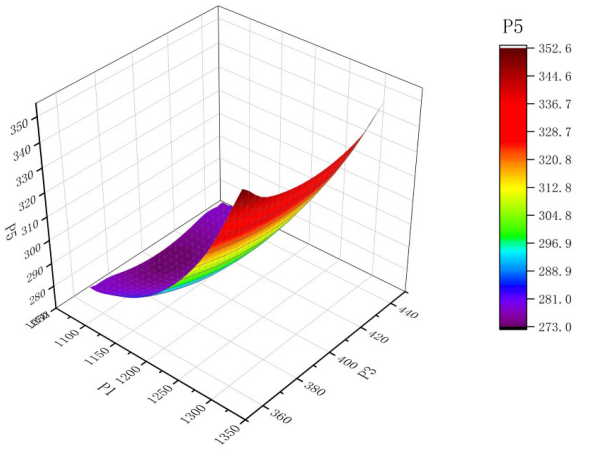

(e) P1-P3-P5 response surface model

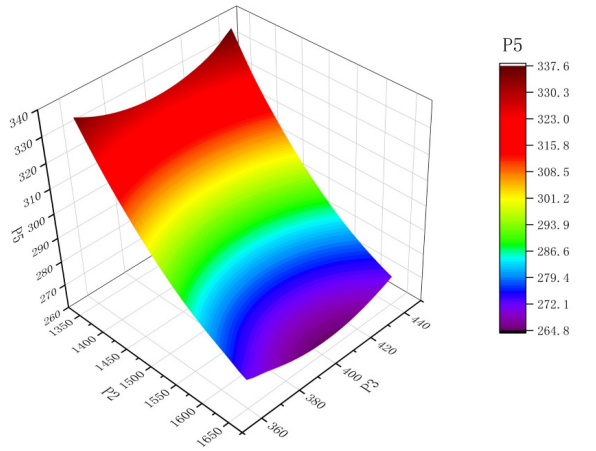

(f) P2-P3-P5 response surface model

Figure 7 Brig scheme Kriging response surface

From figure 7, the design variables and the optimized target response values show obvious nonlinear characteristics. It can be seen that with the increasing of the distance P1, the optimization targets P4 and P5 increase slowly at first. When the distance P1 increases around 1200, the increasing of P4 and P5 become faster, and the response surface model changes more drastically. When P2 gradually increases, the optimization target P4 increases rapidly and then slowly. When the distance P2 is around 1500, the response surface model changes more seriously. The optimization target P5 gradually decreases with the increasing of P2. When P3 gradually increases to 400, the optimization target P4 increases slowly at first. When P3 is greater than 400, the optimization target P4 decreases faster. The effect of P3 on P5 is gradually increased with the increasing of P3, and P5 decreases firstly and then increases with 400 as symmetry. In summary, the design variables and response values show complex nonlinear characteristics, and the response surface model can intuitively show the mutual relations.

5 Results and discussions

The effect of clamp position can change the natural frequencies of pipeline system. The pump excitation is 275Hz, when the natural frequency of the pipeline system are closer to pump excitation frequency, the mechanical resonance will occur. In order to avoid resonance, the natural frequency should be far away from 275 Hz. Therefore, the optimization objective can reach the independent optimal value due to the interaction between design variables and the relationship between optimization objectives. The satisfaction function of MOGA genetic algorithm is usually used to optimize multiple objectives. The following definitions are given for the optimal solution in multi-objective optimization problems. The solution of the constraint conditions is defined as feasible solution. Pareto optimal solution is used as the optimal solutions. The surface composed of the target vectors corresponding to all Pareto optimal solutions. After MOGA analysis, it can be concluded that picture of Pareto front is shown in figure 8, the blue dot value represents the best result.

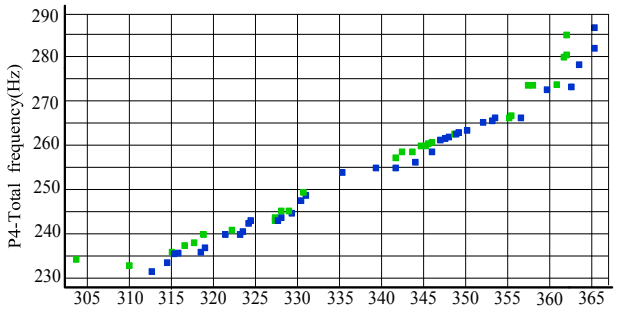

Figure 8 Pareto front

By Pareto front analysis, the optimal solution set can be obtained in which the blue point set is superior to the green point set. The candidate of BBD scheme can be obtained in the Kirging approximate response surface model, which are listed into Table 6.

Table 6 BBD Candidate

	Candidate 1	Candidate 2	Candidate 3
P1-Distance 1/mm	1081.2	1201.1	1231.2
P2-Distance 2/mm	1351.5	1351.3	1350.4
P3-Distance 3/mm	439.15	439.09	438.22
P4-10th natural frequency/Hz	214.66	238.92	245.19
P5-11th natural frequency/Hz	334.79	336.92	342.32

As shown in the Table6, in order to avoid the mechanical resonance of the pipeline, the optimal values of each multi-objective optimization and the comprehensive optimal values of multi-objective optimization can be obtained, as shown in Table 7.

Table 7 Optimal candidate

	P4 optimization	P5 optimization	Comprehensive optimization	Before optimization	Difference comparison
P1-Distance 1/mm	1081.2	1231.2	1081.2	1200.0	118.8
P2-Distance 2/mm	1351.5	1350.4	1351.5	1500.0	148.5
P3-Distance 3/mm	439.15	438.22	439.15	400.00	39.15
P4-10th natural frequency/Hz	214.66	245.19	214.66	254.90	40.24
P5-11th natural frequency/Hz	334.79	342.32	334.79	285.58	49.21

It can be seen from the Table 7 that the natural frequencies of pipeline system can be changed significantly by multi-objective optimization. If the response value is analyzed separately, different optimal design variables will be obtained. However, it is necessary to select a combination of design variables which are different from the natural frequency of the pipeline system and the pump fluid excitation frequency. The optimization objective is that the natural frequency of pipeline should be far away from the excited frequency 275Hz. Therefore, P1 = 1081.2mm, P2 = 1351.5mm, P3 = 439.15mm are the best combination of design variables. Moreover, the 10th natural frequency of pipeline decreases by 40.24Hz after optimization, and the 11th natural frequency increases by 49.21Hz after optimization. The calculation results of statistical candidate points meet the requirements of support optimization, which can improve the calculation time significantly.

6 Conclusion

This paper proposed a developed response surface method to reduce the vibration by optimizing the natural frequency of the pipeline system. The BBD scheme is presented to establish the response surface model between the design variable and the response. New results and conclusions are obtained.

The fitting degree of the sample points of the response surface between the simulation and prediction value is linear, and the predicted line is in good agreement with P4 and P5, which can verify the effectiveness of the response surface model. The response surface model shows complex nonlinear characteristics between P1, P2, P3 and P4 and P5 in order to obtain the optimal solution. The optimization results based on the response surface method can optimal the natural frequencies of pipeline significantly, which is more than 20% away from the pump excitation frequency.

In the design process of offshore pipeline system, the dynamic optimization analysis is essential to ensure that there is no harmful resonance in the working conditions. The proposed developed response surface method in this paper can not only improve the vibration performance of the hydraulic pipeline system, but also improve the calculation efficiency significantly. It provides a new practical optimization method for vibration analysis of offshore hydraulic pipeline system.

Conflict of Interest: The author declare that there is no conflict of interest regarding the publication of this paper.
Acknowledgments: This work is supported by Natural Science Foundation of Shandong Province (Grant no. ZR2018MEE021) and Equipment Pre Research Fund Project (Grant no. 61402100501).

References

[1] Kwong, A.H.M.; Edge, K.A. A method to reduce noise in hydraulic systems by optimizing pipe clamp locations. Proceedings of The Institution of Mechanical Engineers Part I Journal of Systems & Control Engineering, 1998, 212(4):267-280.

[2] Wang, D.; Jiang, J.S.; Zhang, W.H. Optimization of support positions to maximize the fundamental frequency of

structures. International Journal for Numerical Methods in Engineering, 2004, 61(10):1584-1602.

[3] Wang, D. Optimization of support positions to minimize the maximal deflection of structures. International Journal of Solids & Structures, 2004, 41(26):7445-7458.

[4] Liu, Y.S.; He, X.D.; Zhu, Y.H. et al. Dynamical strength and design optimization of pipe-joint system under pressure impact load. Proceedings of the Institution of Mechanical Engineers, 2012, 226(G8):1029-1040.

[5] Li, X.; Zhang, L.J.; Wang, S.P. et al. Impedance analysis and clamp locations optimization of hydraulic pipeline system in aircraft. International Conference on Fluid Power & Mechatronics, Ha Erbin, China, 2015.08.05, pp.1023-1028.

[6] Gao, P.X.; Li, J.W.; Zhai, J.Y. et al. A novel optimization layout method for clamps in a pipeline system. Applied Sciences. 2020, 10(1): 390.

[7] Box G, Wilson K. On the experimental attainment of optimum condition. Journal of the Royal Statistical Society, 1951, 13(1): 1-45.

[8] Xiao, M.H.; Shen, X.J.; Liu, X. Study on properties of 45 Carbon Steel Ni-P electroless plating reinforced by Si3N4-Al2O3 particle based on response surface method. Journal of Nanoscience and Nanotechnology. 2020, 20, 4761-4772.

[9] Zhang, T.; Zhou, X.P.; Liu, X.F. Reliability analysis of slopes using the improved stochastic response surface methods with multicollinearity. Engineering Geology. 2020, 271, doi: 10.1016/j.enggeo.2020.105617.

[10] Abba, S.I.; Usman A.G.; Isik, S. Simulation for response surface in the HPLC optimization method development using artificial intelligence models: A data-driven approach. Chemometrics and Intelligent Laboratory Systems. 2020,201, doi: 10.1016/j.chemolab.2020.104007.

[11] Gao, L.; Gegentana; Liu, Z.Z.; Sun. B.Z.; Li, S.H. Multi-objective optimization of thermal performance of packed bed latent heat thermal storage system based on response surface method. Renewable Energy. 2020, 153, pp. 169-180.

[12] Perwez, A.; Siddiqui, N.A.; Alqahtani, A.S.; Haque, A. Response surface methodology-based optimization of ultrasound-assisted extraction of beta-sitosterol and lupeol from astragalus atropilosus (roots) and validation by HPTLC method. Asian Pacific Journal of Tropical Biomedicine. 2020, 10, pp. 281-292.

[13] Heddam, S.; Keshtegar, B.; Kisi, O. Predicting total dissolved gas concentration on a daily scale using kriging interpolation, response surface method and artificial neural network: Case Study of Columbia River Basin Dams, USA. Natural Resources Research. 2020, 29, pp. 1801-1818.

[14] Xie, Y.W.; Hu, P.F.; Zhu, N.; Lei, F.; Xing, L.; Xu, .L.H. Collaborative optimization of ground source heat pump-radiant ceiling air conditioning system based on response surface method and NSGA-II. Renewable Energy.2020, 147, 149-167.

[15] Shirazi, M.; Khademalrasoul, A.; Ardebili, S.M.S. Multi-objective optimization of soil erosion parameters using response surface method (RSM) in the Emamzadeh watershed. Acta Geophysica.2020, 68, pp.505-517.

[16] Xue, X.F.; Wang, Y.Z.; Lu, C. Sinking velocity impact-analysis for the carrier-based aircraft using the response surface method-based improved kriging algorithm. Advances in Materials Science And Engineering. 2020, 202, 10.1155/2020/5649492.

[17] Solmaz, H.; Ardebili, S.M.S.; Aksoy, F.; Calam, A.; Yilmaz, E. Arslan. Optimization of the operating conditions of a beta-type rhombic drive stirling engine by using response surface method. Energy. 2020, 198, doi: 10.1016/j.energy.2020.117377.

[18] Bai, B.; Li, H.; Zhang, W.; Cui, Y.C. Application of extremum response surface method-based improved substructure component modal synthesis in mistuned turbine bladed disk. Journal of Sound and Vibration. 2020, 472, doi: 10.1016/j.jsv.2020.115210.

[19] Su, Y.; Fu, G. Wan, Bo. et al. Fatigue reliability design for metal dual inline packages under random vibration based on response surface method. Microelectronics Reliability, 2019, 100, 113404.

[20] Ferreira, S.; Bruns, R.; Ferreira, H. et al. Box-Behnken design: an alternative for the optimization of analytical methods. Analytica Chimica Acta, 2007, 597(2):179-186.

Viser Technology Pte. Ltd.
Mechanical Engineering Science
doi: 10.33142/mes.v2i2.3162

Research Article Open Access

Wind Turbine Speed Compound Control of a New-Type Wind-Electric Hybrid Power Pumping Unit

Chunyou ZHANG*, Lihua WANG

College of Engineering, Inner Mongolia University for Nationalities, Tongliao, China

***Corresponding Author:** Chunyou ZHANG, E-mail: zcy19801204@126.com*

Abstract:
Because the load of the oil beam pumping unit driven by pure electric motor changes sharply during operation, the power of the driving motor does not match and the energy efficiency is low. In this paper, a new type of wind-driven hydro-motor hybrid power system is proposed. The motor and the hydraulic motor are jointly driven, and the energy is recovered by a hydraulic pump with controllable displacement, so that the speed of the driving motor is relatively stable. In order to control the fan speed and keep up with the drastic changes of the outside wind speed, a control strategy of hybrid power system based on wind speed feed-forward compensation is proposed. Through simulation and experimental results, the following conclusions can be drawn: to begin with, the mathematic model is proved to be effective; next, simulation studies show that the proposed feed-forward control method can improve the response rate as well as reduce the response lag. This research can be a reference for the application of the feed-forward control method on the hybrid power system of beam pumping unit.system.

Keywords: *beam pumping unit; hydraulic-motor hybrid system; feed-forward control method; Fuzzy-PID control*

1 Introduction

Beam pumping unit is the most widely used engineering machineries in the petroleum production industry [1]. In order to periodically drive the pumping operation, the traditional method is using electromotor to directly drive the crank [2]. Due to the particularity of the oil rod job, the mechanical load characteristics of the driving unit are periodically and drastically changed [3], which makes the efficiency of the whole power system relatively low. The most recent studies on the power system of beam pumping unit mainly focused on the beam unit structure optimizations and control motor selection. Dong et al [4] simulated the dynamic performance of the beam pumping system, and the comprehensive optimization algorithm is proposed in order to improve the operation speed. Gibbs [5] declared that electrical predictions can be used in the mechanical models of oil pumping system. Lv et al [6] proposed an energy saving system for a beam pumping unit based on four types of networking sensors. However, structure optimizations can hardly change the operation mode of the beam unit. Moreover, control regulation and component selection can not in principle avoid the power mismatch problem of the drive motor. Therefore, the efficiency of the traditional direct-drive method is low, and the operational reliability is bad.

Recently, more and more researchers have focused on the study of the wind speed following control. Li et al [7] proposes a wind speed predictive method by neural network, and they improve the ability of small wind power generation system to capture wind energy by robust control of maximum power extraction for potential drift of wind turbine power coefficient curve. Soufi et al [8] proposes a particle swarm optimization method based on feedback linearization control in order to study the maximum power point tracking control (MPPT) of wind power generator set. In their research, the maximum wind energy absorption is the goal to achieve the maximum wind energy capture. However, the accuracy of the control methods can not be proved. Because the wind wheel machine belongs to system of large inertia and large lag, error of the traditional control method is large. Based on variable speed constant frequency wind power system, Ren et al [9] put forward the method of feed-forward and feedback control strategy for variable pitch control which can realize the constant power output above the rated wind speed. Chen et al [10] study the MPPT control strategy based on permanent magnet synchronous wind generator, and the MPPT control of wind wheel is realized by adjusting the on-line control parameters with feed-forward controller. Abo-Khalil et al [11] also research the wind power generation system based on doubly-fed

induction generator based on controlled MPPT by using feed-forward and feedback. Liang [12] et al propose a feed forward transient compensation (FFTC) control scheme based on doubly-fed induction generator with proportional integral resonant current regulator in order to enhance the low voltage crossing (LVRT) capability and adapt to unbalanced power grid faults. Verwaal [13] et al develop a more reliable wind speed measurement method to enhance the control performance of wind turbine by implementing feed-forward related control strategy. These studies all carry on the application of advance control method on the wind wheel power system. However, the studies mainly focus on the control method on the pumping unit with direct driven motor.

This paper proposes a new type of hydraulic-motor hybrid power system for the beam-pumping unit, and a new feed-forward control method. The principle of the hybrid power system is proposed, and the mathematical model is set up which is verified by experiment studies. In addition, the results of the feed-forward control on the hybrid power system of the beam pumping unit are compared with the traditional PID method.

2 Modelling and experiment

2.1 Configuration of the new kind of wind power hydraulic-motor hybrid power system of the beam-pumping unit

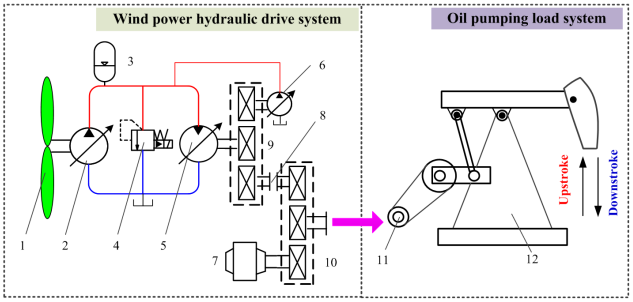

Figure 1 Structure of the oil pumping drive system based on wind power hydraulic

(1). Wind wheel. (2). Controlled hydraulic pump A. (3). Energy accumulator. (4). Relief valve.(5). Controlled hydraulic motor. (6). Controlled pump B. (7). Electrical motor. (8). Clutch.(9). Torque meshing gear group A. (10). Torque meshing gear group B.(11). Load shaft. (12). Beam pumping unit.

A new-kind of wind power hydraulic-motor hybrid power system special for beam pumping unit is designed, and its configuration is illustrated in figure 1. Structure The oil pumping drive system mainly consists two parts: one is wind power hydraulic drive system, and the other is oil pumping load system. The wind power hydraulic drive system is the main part and is mainly composed of a wind wheel, two discharged controlled hydraulic pumps, a controlled hydraulic motor, two meshing gear groups, an energy accumulator, and an electrical motor. The oil pumping load system is similar to the traditional beam pumping unit, which means this designed power system is common to the general beam pumping unit.

Main power source of the system is wind power, and it is directly gathered by the wind wheel. The rotating wind wheel drives hydraulic pump A, and then generates high pressure at the upstream side of the hydraulic motor. Both the torque meshing gear groups have three intercoupled gears. In addition, one of the three gears couples the torques of the other two gears, and it is called the sum gear. When hydraulic motor is driven, sum gear A drives the other two gears. One of the gears outputs torque to controlled pump B, and the other provides power to torque meshing gear group B. In order to avoid the lack of power of the system, an electric motor is added in controlled pump B as the torque compensation unit. Sum gear B directly drives load shaft of the oil pumping load system. What is more, the controlled pump B and the hydraulic accumulator can recycle excess energy from the load system when the sum gear B is over torqued.

According to figure 1, one working cycle of the beam pumping units mainly consists of up stroke and down stroke of the horse head. In addition, working cycles of the beam pumping unit and drive load shaft are synchronous. In another word, a circle work of sum gear B includes two working strokes of the beam pumping unit.

As is mentioned above, motor which directly drives the load shaft of the beam pumping unit will work at a relatively low efficiency. That is because during the start process the drive motor needs a very high power to put the beam pumping unit in motion, however when the unit keeps working regularly, the motor needs a relatively low power which is approximately half of the start power, and that will lead to a great mismatch of the engine power, which will result in a poor efficiency of the motor. This paper provides a method that uses wind power as the main power source, and the designed motor is applied as the auxiliary power supply. This kind of setting can avoid the motor working at a power which is far away from the rated power, and then avoid the inefficiency of the motor.

When the beam pumping unit works at the down stroke process, geopotential energy of the horse head rapidly transforms into kinetic energy. That will lead to prompt acceleration of the rotating speed of motor rotor, and motor will reversal which can interference the motor control. Another unique feature of the designed hybrid power system is that during the down stroke process of the beam pumping unit, through the torque meshing gear groups a large part of the kinetic energy of the horse head will transform to the output hydraulic energy of controlled pump B, and the accumulator will store the energy and then leave it to the upstroke process, which achieves energy recovery.

2.2 Modeling of the working process

According to the structure of the designed wind power hydraulic-motor hybrid system, mathematical model of the dynamic working process is built as follows.

2.2.1 Dynamic model of the wind rotor

According to the previous research [15], when the wind speed

is at a certain value, speed of the wind rotor has an optimal point which can keep the highest wind energy efficiency. In order to obtain as much wind power as possible at a certain wind speed, this paper assumes that the wind rotor is controlled within an interval of precision that can get an optimum tip speed ratio. The dynamic equation of the wind rotor is as shown in Eq. (1):

$$J_w\dot{\omega} = T_w - T_P' - T_{fw} - B_w\omega \tag{1}$$

where, J_w is inertia of the wind rotor, w is rotating speed of the rotor, T_w means the fan torque, T_P' is the restoring torque of the hydraulic pump, T_{fw} is coefficient of mechanical friction, and B_w is viscosity coefficient. The restoring torque of the hydraulic pump T_P' can be precisely controlled, and then the rotating speed of the wind rotor can be controlled to keep the rotor working at the best state.

2.2.2 Equations of the hydraulic pump

In this hydraulic system, there are two hydraulic pumps with the same working principle. The equation of the restoring torque of the hydraulic pump T_P' is as follows:

$$T_P' = i \cdot T_P = i \cdot (\Delta p \cdot D_P + J_p\dot{\omega} + B_p\omega) \tag{2}$$

where, i is transmission ratio of the speed increaser, T_p is drive torque of the hydraulic pump, Δp is pressure difference between the inlet and outlet of the pump, D_p is displacement of the pump, J_p is rotational inertia of the pump, and B_p is viscous friction coefficient of pump shaft.

Flow equation of the hydraulic motor can be described as:

$$q_p = D_p\omega_p - C_{ip}(p_h - p_l) - C_{ep}p_h - \frac{V_P}{\beta_e}\frac{dp_h}{dt} \tag{3}$$

where, q_p is the output flow of the pump, w_p means the rotating speed of the pump, C_{ip} and C_{ep} respectively are internal and external leakage parameters, p_h and p_l are pressures on the high and low sides of the pump, V_p is displacement of the variable pressure pump chamber, β_e is the effective bulk modulus of hydraulic oil.

2.2.3 Equation of the hydraulic motor

Similarly, the equation of the hydraulic motor can be obtained as follows. The flow of the hydraulic motor q_m is:

$$q_m = D_m\omega_m + C_{im}(p_h - p_l) + C_{em}p_h + \frac{V_m}{\beta_e}\frac{dp_h}{dt} \tag{4}$$

where, q_m is the output flow of the motor, w_m means the rotating speed of the motor, C_{im} and C_{em} are internal and external leakage parameters of the motor, respectively, p_h and p_l are pressures on the high and low sides of the motor, V_m is displacement of the variable pressure pump chamber.

2.2.4 Flow equation of the hydraulic accumulator

In this system, the hydraulic accumulator is used to recover and store the impact energy in the down stroke process of the horsehead of the beam pumping unit. Characteristics of the accumulator greatly affect the stability of the hybrid system. The flow equation of the accumulator is as follows:

$$q_a = \frac{V_0}{nP_0}\frac{dp}{dt} \tag{5}$$

where, q_a is the flow into the accumulator, V_0 is the initial volume of the accumulator, n is the air polytropic exponent, and P_0 is inflation pressure of the accumulator.

2.2.5 Flow equation of the whole system

According to the above equations, the flow formulation of the whole system can be derived as follows:

$$q_{pA} + q_{pB} + q_a = q_m \tag{6}$$

where, q_{pA} and q_{pB} is respectively the flow of controlled pump A and B. And it is assumed that the low pressure side of the hydraulic system is 0, and the effective bulk modulus of hydraulic oil is neglected. Then the flow equation can be obtained as follows:

$$D_{pA}\omega_{pA} + D_{pB}\omega_{pB} - D_m\omega_m + C_t p_h + \frac{V_0}{nP_0}\frac{dp_h}{dt} = 0 \tag{7}$$

where, w_{pA} and w_{pB} are rotating speeds of the hydraulic pumps, and D_{pA} and D_{pB} are displacements of the hydraulic pumps, respectively. C_t is calculated parameters as follows:

$$C_{ipA} + C_{epA} + C_{ipB} + C_{epB} - C_{im} - C_{em} = C_t \tag{8}$$

where, C_{ipA}, C_{epA}, C_{ipB} and C_{epB} respectively are internal and external leakage parameters of pump A and B.

2.2.6 Torque coupling equation

Torque coupling means in the coupling process, the output torque of two power sources is independent from each other, while the output speed must be equal before the dynamic coupling. The final synthetic torque is the superposition of output torque of two power sources. The structure of the coupling gears is as shown in figure 2.

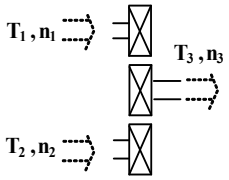

Figure 2 Structure of the coupling gear group

As is shown in figure 2, if the coupling gear group includes three gears, torque and rotating speed of the output gear are $\mathbf{T}_3$ and $\mathbf{n}_3$, and the corresponding parameters of the input gears are $\mathbf{T}_1$, $\mathbf{T}_2$, $\mathbf{n}_1$ and $\mathbf{n}_2$. The equations of the torque coupling are as follows:

$$\mathbf{n}_1 = \mathbf{n}_2 = \mathbf{n}_3 \tag{9}$$

$$\mathbf{T}_1 + \mathbf{T}_2 = \mathbf{T}_3 \tag{10}$$

Then according to figure 1, we can get the gear coupling equations of the hybrid system:

$$T_m = T_{PB} + T' \tag{11}$$

$$T_l = T' + T_{em} \tag{12}$$

where, T_m and T_{PB} is respectively the torque of the hydraulic motor and hydraulic pump B, T^* is the transmission torque between the two gear groups, T_l is the load torque, and T_{em} is toque of the electric motor. Then T_{em} can be derived:

$$(D_m - D_{pB}) \cdot P_h - (J_m + J_{pB}) \cdot \ddot{\theta}_m - (B_m + B_{pB}) \cdot \dot{\theta}_m - (G_m + G_{pB}) \cdot \theta_m + T_{em} = T_l \tag{13}$$

where, D_m and D_{pB} are displacements of hydraulic motor and pump B, J_m and J_{pB} are rotational inertia of hydraulic motor and pump B, B_m and B_{pB} are damping coefficients of hydraulic motor and pump B, G_m and G_{pB} are stiffness values of hydraulic motor and pump B,

and θ_m is rotation of the hydraulic motor. In addition, electromagnetic torque of the motor T_{em} is relative with θ_m.

2.3 Experimental verification

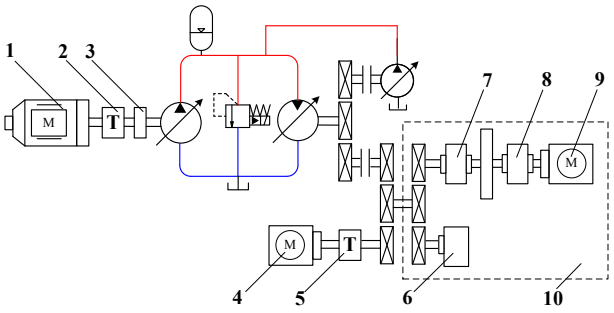

Figure 3 Sketch diagram of the test station

(1). Variable frequency motor. (2). Torque and speed sensor 1. (3). Speed changer. (4). Electromotor 1. (5). Torque and speed sensor 2. (6). Magnetic powder brake. (7). Magnetic powder clutch 1. (8). Magnetic powder clutch 2. (9). Electromotor 2. (10). Load simulation part.

As is shown in figure 3 and 4, in order to demonstrate the mathematical model above, a test station of the hybrid system is built. In this experiment, a variable frequency motor is selected in order to simulate the wind rotor, and between the variable frequency motor and hydraulic pump there is a torque and speed sensor which can measure the input torque of the simulated power source. That is because in this paper the wind source is considered as a torque-controlled device, and in the experiment the power value of the source is needed. As can be seen of the picture, an electromotor 1 is added in the gear group which is treated as the assisted motor, and a torque and speed sensor is directly connected between them in order to detect the output characteristics of the assisted motor. As is shown from this figure, load of the beam pumping unit is simulated by part 10. The simulated load should be accordance with the dynamic loading process which is shown in figure 5. One cycle of the dynamic torque of the mechanical load is obtained by regular working equations of beam pumping unit. The simulation method is periodic servo control of the output load torque.

As is shown in figure 4, rated power of the variable frequency motor is 1.2KW, rated power of electromotor A is 550W, and rated power of the electromotor B is 2.2KW. That is because electromotor B is used for the torque compensation, and in order to ensure the working efficiency of the motor approximately optimal, the rated output power of electromotor B is selected larger, and prepare for future type selection optimization.

Table 1 Several parameter values of the experimental station

Parameter	Value	Parameter	**Value**
Depth of plunger (m)	10000	Rated power of original motor (kW)	37
Working fluid level (m)	600	Rated power of replaced motor (kW)	22
Diameter of rod (mm)	22	Diameter of pump (mm)	57
Stroke(m)	2	Diameter of tube (mm)	76
Water cut (%)	100	Frequency of stroke(1/min)	6

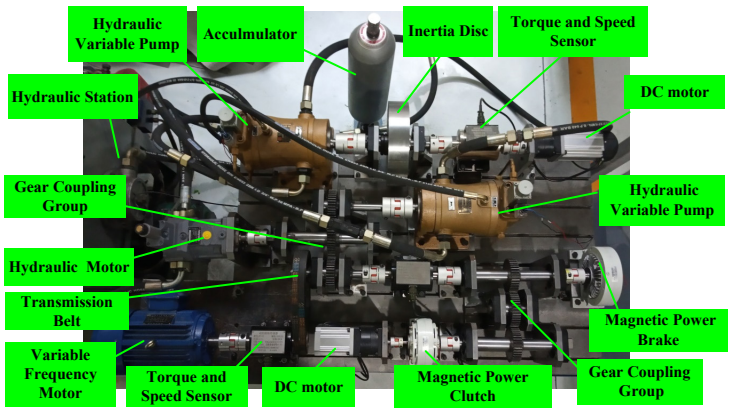

Figure 4 Experimental station of the wind-electric hybrid system

Figure 4 is the experimental station of the wind-electric hybrid system according to principle of Figure 3. In the process of the experiments, so as to demonstrate the mathematical model at the same time considering the safety and the common performance of the hydraulic system, displacements of the hydraulic motor and pump are settled stable. The working speed of the hybrid system is set to about 700 RPM to ensure the stability. Torque sensor 2 is adopted to measure the output torque of the beam pumping unit, and the working process of the beam pumping unit is simulated by close-loop controlling its output torque with the feedback of the torque sensor. A group of torque data of the beam pumping unit of model CYJ10-3-37HB is obtained. According to the principle of

the dynamic torque of the actual project, the control result of the torque is scaled down at the same proportion which can be seen in Figure 5.

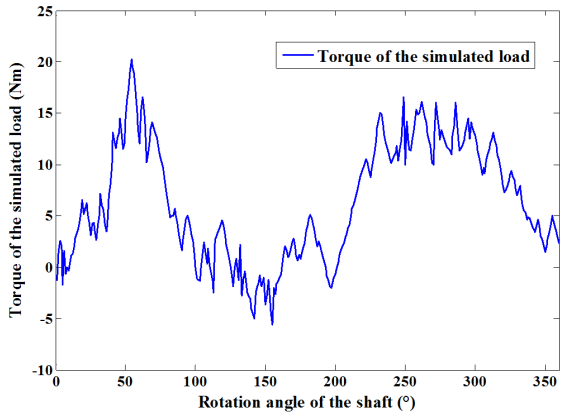

Figure 5 Experimental result of the simulated load torque

Test process:

(1) Start the motor and set all the clutches to the off state;

(2) Adjust the clutch to the closed state to simulate the pumping unit load;

(3) Start the variable frequency motor and adjust the pump displacement to simulate the wind turbine;

(4) All clutches are closed to simulate the wind-electric hybrid process.

(5) The experimental data are collected through the test system.

The measurement and control system of the experimental station mainly includes industrial control computer (IPC), PCI bus communication, data acquisition card, signal conditioning circuit and control board card. This experimental system uses RTX as the lower machine and Lab Windows as the upper computer. The control cycle of the real-time measurement and control system can reach 0.5ms. Experimental station control system is shown as Figure 6.

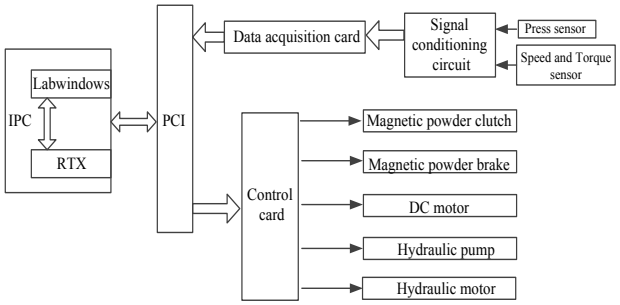

Figure 6 Experimental station control system

The experimental data curve is shown in Figure 7. The motor output power is stable by changing the displacement of pump and hydraulic motor. This helps to the improvement of motor efficiency. When wind speed is 9m/s, the output power of the electromotor varies around 580W. When wind speed is 11m/s, the electric power varies around 300W. Simulation and experiment results indicate the stable output power of the motor is different under different wind speed. The wind power increases, the electric power decreases. The correctness of the mathematical model and energy saving method is verified by numerical simulation and experiment.

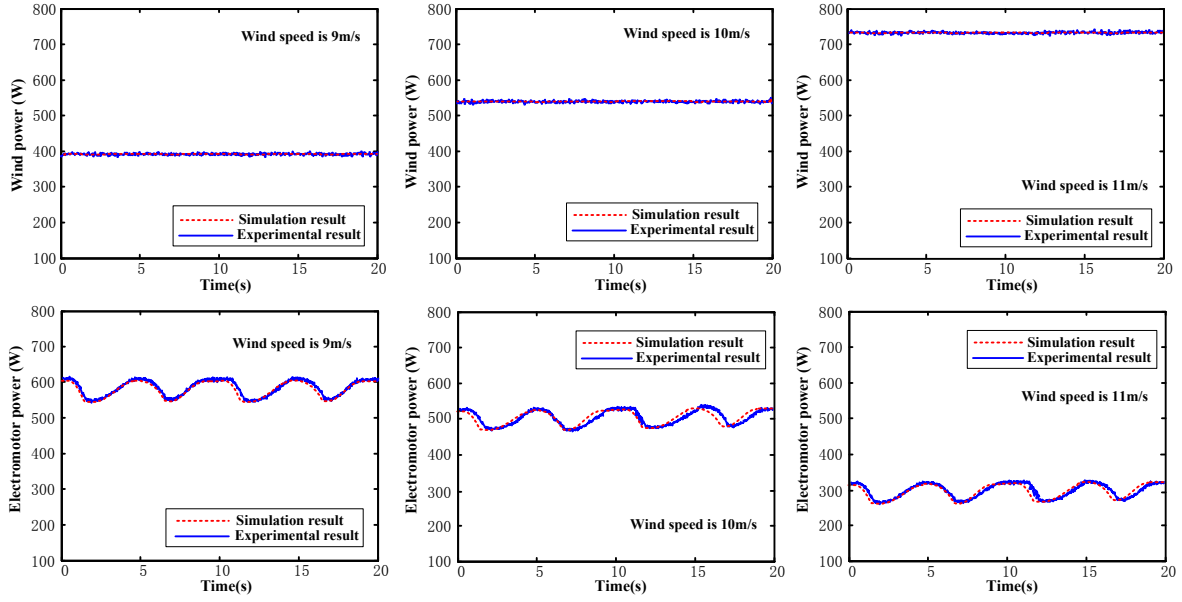

Figure 7 Power contrast curves under different wind speed

3 Wind speed following control method and analysis

According to the application, in order to make the wind wheel work at the optimum velocity ratio under different wind speed, the optimal working speed of the wind wheel should be controlled so as to get the highest efficiency. The optimal equation is as follows:

$$\lambda_{opt} = \frac{R \cdot \omega_{opt}}{v} \tag{14}$$

where, v represents the wind speed, and w_{opt} is the corresponding optimal angular velocity of the wind wheel, R is the radius of the wind wheel.

Structure of the control system based on feed forward control

As can be seen in Figure 8, main structure of the hybrid power system is a feed forward and closed-loop system. The Feed forward control part is from the wind speed branch current, and the function is expressed as $F_n(s)$. Controlling unit of the hybrid system is expressed as $G(s)$, and then the basic control principle is as follows.

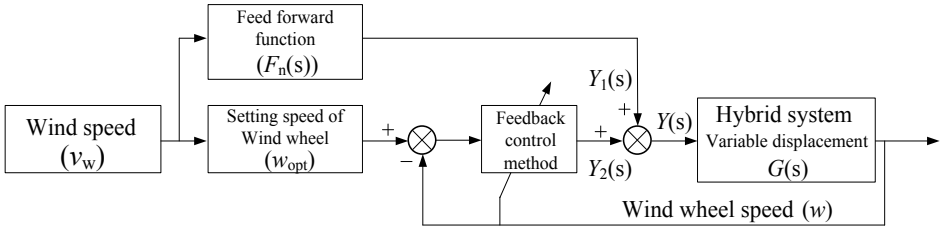

Figure 8 Flow chart of the feed-forward control method of the hybrid system

Dynamic change of the wind speed can be treated as disturbance part, and the feedback control method in the middle part is expressed as $C(s)$. Therefore, the output function of the wind wheel speed is:

$$w = G(s)\cdot Y(s) = G(s)\cdot(Y_1(s)+Y_2(s)) \tag{15}$$

$$Y_1(s) = v_w \cdot F_n(s) \tag{16}$$

$$e(\mathrm{k}) = \omega_{set}(\mathrm{k}) - \omega(\mathrm{k}-t_d/T) \tag{17}$$

then, the transfer function from the disturbance part to the output part is:

$$\frac{w}{v_w} = \frac{(F_n(s)+w_{opt}C(s))\cdot G(s)}{1+G(s)\cdot C(s)} \tag{18}$$

then the error transfer function is:

$$\frac{v_w\cdot w_{opt}-w}{v_w\cdot w_{opt}} = \frac{w_{opt}-F_n(s)\cdot G(s)}{w_{opt}(1+G(s)\cdot C(s))} \tag{19}$$

If the error is controlled to zero, then $w_{opt}-F_n(s)\cdot G(s)=0$.

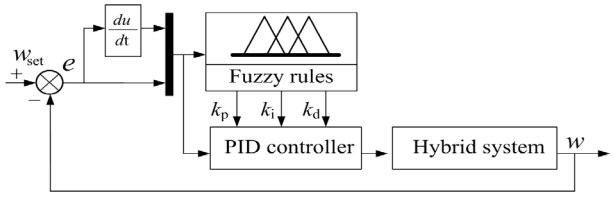

Figure 9 Diagram of the fuzzy-PID control system

The fuzzy-PID part is shown in Figure 9. The hybrid system is directly controlled by P_w, and P_w can be calculated by the following equations:

$$D_w(\mathrm{k}) = D_{in} + D_{com}(\mathrm{k}) \tag{20}$$

$$D_{com}(\mathrm{k}) = k_p e(\mathrm{k}) + k_i T\sum_{j=0}^{k} e(\mathrm{j}) + k_d(e(\mathrm{k})-e(\mathrm{k}-1))/T \tag{21}$$

$$e(\mathrm{k}) = \omega_{set}(\mathrm{k}) - \omega(\mathrm{k}-t_d/T) \tag{22}$$

where e is the error of the control signal, k is the step number, T is sampling time, P_{in} is the settled initial pulse width, and P_{com} means the pulse width compensation.

3.2 Fuzzy rules

The fuzzy rules are self-adjusted according to the fuzzy relations between k_p, k_i, k_d, and e, e_c. Fuzzy outputs are k'_p, k'_i, k'_d, and:

$$k'_p = (k_p - k_{p\min})/(k_{p\max}-k_{p\min}) \tag{23}$$

$$k'_i = (k_i - k_{i\min})/(k_{i\max}-k_{i\min}) \tag{24}$$

$$k'_d = (k_d - k_{d\min})/(k_{d\max}-k_{d\min}) \tag{25}$$

Where, k_{pmin} means the minimum value of k_p, and k_{pmax} means the maximum value. In addition, k'_p, k'_i, $k'_d \in [0,3]$.

Fuzzy adjustment tables of k'_p, k'_i, k'_d are shown as the following table. As shown in Table 2, NB, NM, NS, ZO, PS, PM and PB mean negative big, negative middle, negative small, zero, positive small, positive middle and positive big, respectively. In addition, as is shown in figure 10 and 11, it is the fuzzy membership functions.

Table 2 Diagram of the fuzzy-PID control system

e_c \ e	NB	NM	NS	ZO	PS	PM	PB
NB	PB	PB	PB	PS	PS	PS	PS
NM	PM	ZO	PB	PB	PB	PS	PS
NS	PM	ZO	PB	PB	PB	PS	PS
ZO	PM	ZO	PB	PB	PB	PB	PS
PS	PM	ZO	ZO	PB	PB	PB	PB
PM	PM	PM	ZO	PB	PB	PB	PB
PB	ZO	PM	PM	PM	PM	PM	PM

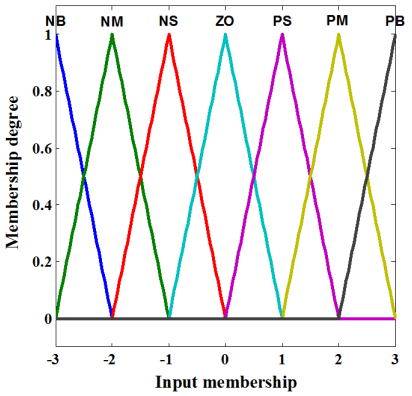

Figure 10 Fuzzy membership function of the input parameter

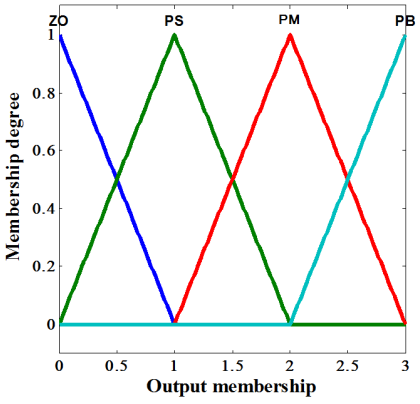

Figure 11 Fuzzy membership function of the output parameter

4 Control analysis

In order to analyze the control effect of the feed forward control, the results are compared with the traditional PID control method. According to the actual measurement of the dynamic wind speed, frequency of the wind is set to 0.1, 0.2, 0.3, and 0.5 Hz, and amplifier of the wind is set to 1, 3, and 5 m/s.

When the frequency of the wind speed is set to 0.1Hz, and the amplifier is 3m/s, then the frequency is relatively low, and the amplifier is relatively small. As is shown in Figure 12, when the hybrid control system applies the normal PID method, the highest over shoot of the revolving speed of the wind wheel is over 40%, and the control result curve slightly lags behind the control signal. However, as is shown in Figure 13, when the feed forward control method is applied, the overshoot basically disappears, and the lag hardly exist, which shows good control following features.

In the real application, when variation of the wind speed is higher, in the simulation the frequency of the wind speed is set to 0.2Hz, and the amplifier is 3m/s. As is shown in Figure 14, when the frequency is relatively high, and the system is controlled by PID control method, the overshoot is about 30%, and the lag behind the control signal is about 2 seconds. As is shown in Figure 15, it can be seen that the overshoot is greatly reduced, and the control result curve lag is eliminated.

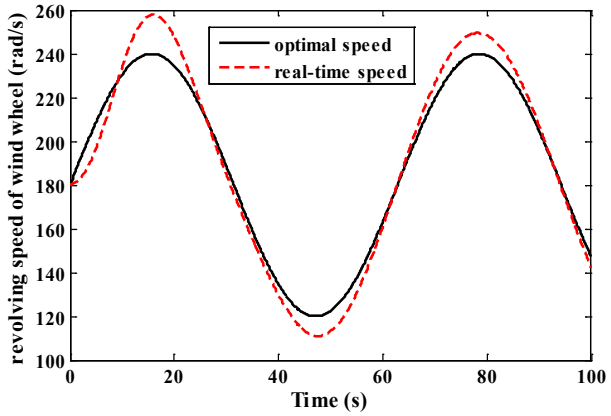

Figure 12 PID control method (Frequency is 0.1 Hz, and Amplifier is 3 m/s)

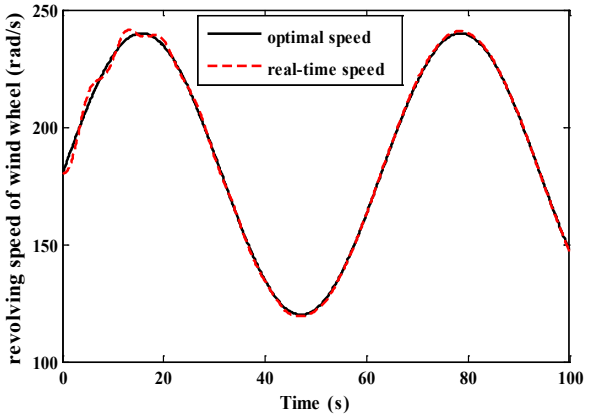

Figure 13 Feed forward control method (Frequency is 0.1 Hz, and Amplifier is 3 m/s)

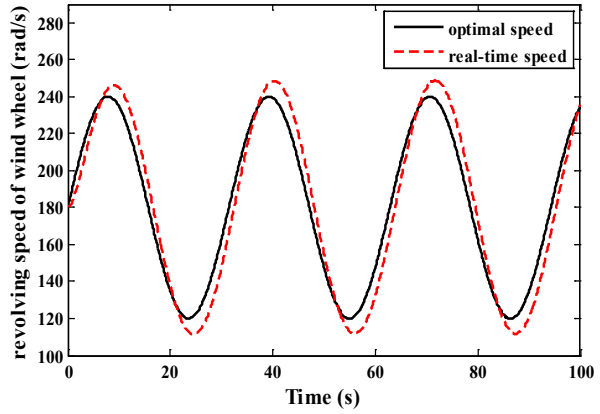

Figure 14 PID control method (Frequency is 0.2 Hz, and Amplifier is 3 m/s)

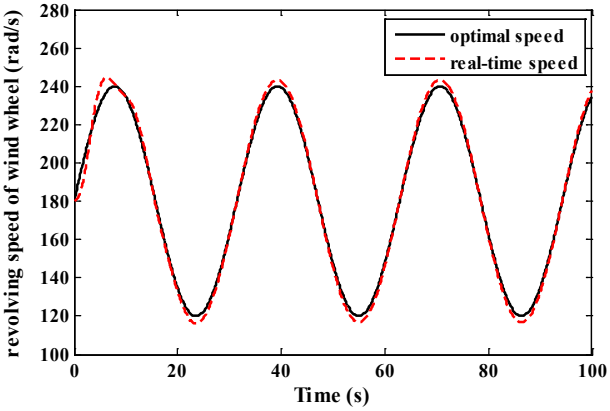

Figure 15 Feed forward control method (Frequency is 0.2 Hz, and Amplifier is 3 m/s)

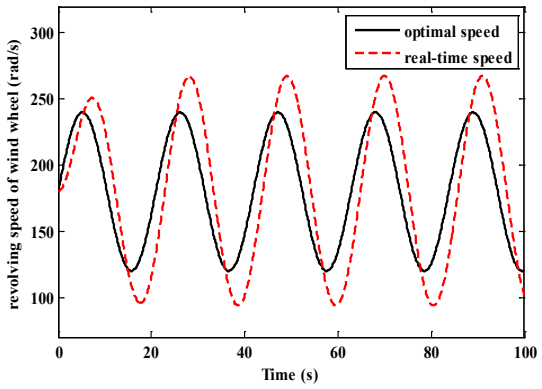

Figure 16 PID control method (Frequency is 0.3 Hz, and Amplifier is 3 m/s)

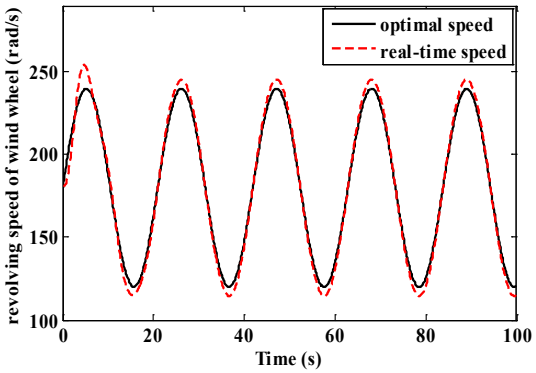

Figure 17 Feed forward control method (Frequency is 0.3 Hz, and Amplifier is 3 m/s)

When the frequency of the wind speed is set to 0.3Hz, and the amplifier is 3m/s, from Figure 16 it can be seen that under the PID control method the overshoot is much serious which can be up to over 50%. In addition, the output signal lags behind the control signal by 4 seconds to the maximum. In the real application, when the output speed can hardly follow the control signal, the efficiency will always be at a low condition. However, the feed forward control method can greatly solve this problem. In Figure 17, when the feed forward control method is applied, the control overshoot can be reduced by 3over 80%. In addition, the lag can also be eliminated, too.

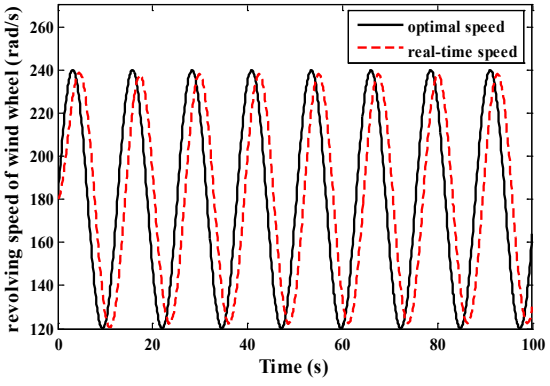

Figure 18 PID control method (Frequency is 0.5 Hz, and Amplifier is 3 m/s)

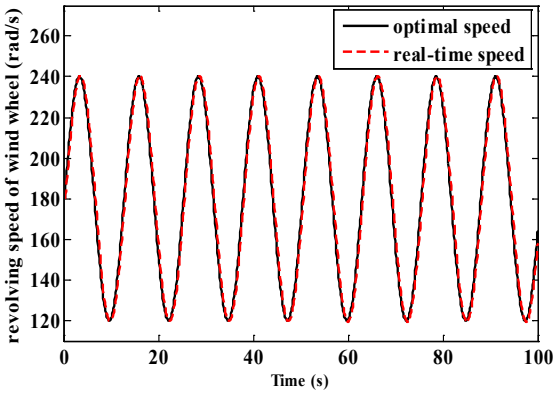

Figure 19 Feed forward control method (Frequency is 0.5 Hz, and Amplifier is 3 m/s)

The highest real frequency of the wind speed can up to 0.5Hz. When the frequency of the wind speed is set to 0.5Hz and the amplifier is 3m/s, the PID control method shows a significant lag between the control and output signals. The lagging time is about 2 seconds, so it accounts for about 35% of the whole period. This paper applies feed forward control method, and it obviously solves the lagging problem, the follow-through level reaches a good level.

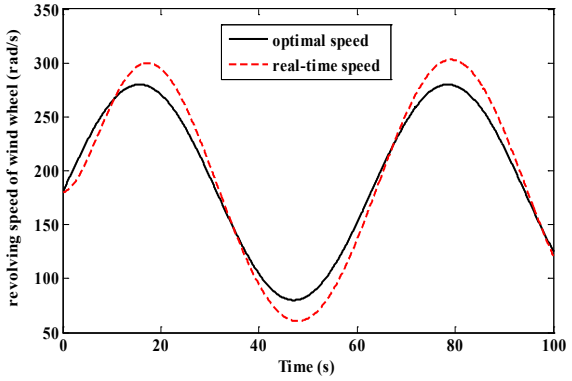

Figure 20 PID control method (Frequency is 0.1 Hz, and Amplifier is 5 m/s)

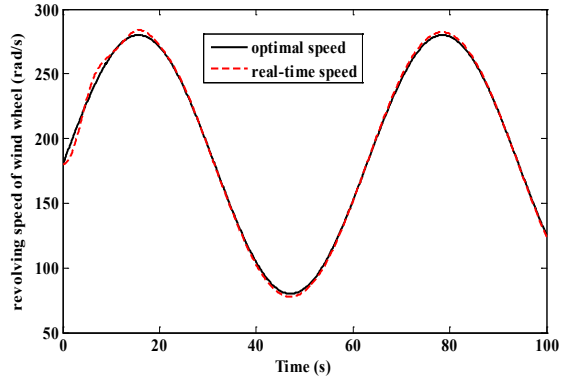

Figure 21 Feed forward control method (Frequency is 0.1 Hz, and Amplifier is 5 m/s)

When the amplifier is set relatively high to 5m/s, through PID control method it mainly appears overshoot

and lagging problem. The overshoot value is about 25%, however, the lagging problem is not very serious. From Figure 22, the Feed forward control method can greatly solve the overshoot problem.

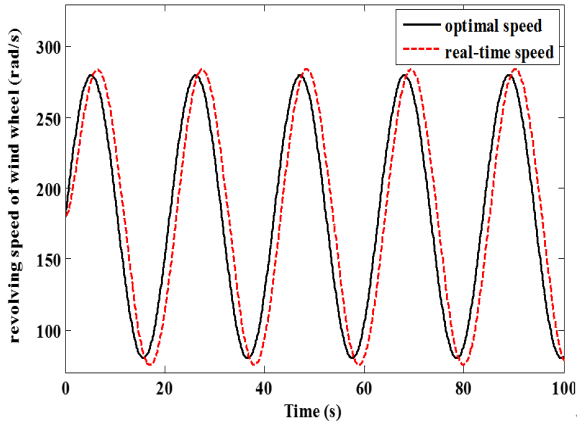

Figure 22 PID control method (Frequency is 0.3 Hz, and Amplifier is 5 m/s)

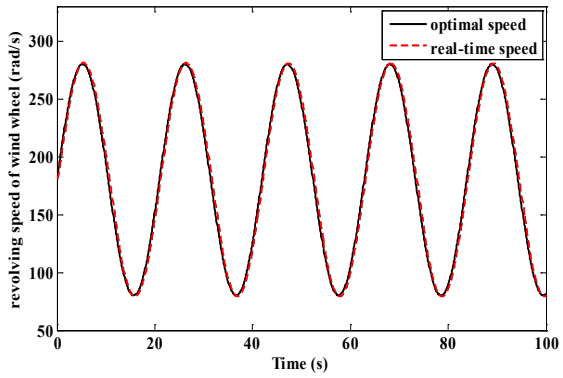

Figure 23 Feed forward control method (Frequency is 0.3 Hz, and Amplifier is 5 m/s)

When the frequency is relatively high and the amplifier is high, too, lagging time with the PID control method is approximately 20%. From Figure 23, the Feed forward control method can also solve the lagging problem, which is the same as the above results.

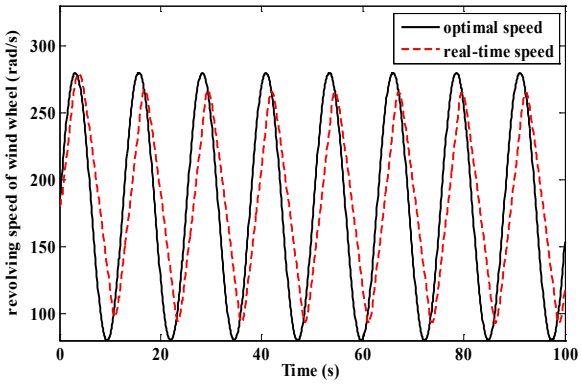

Figure 24 PID control method (Frequency is 0.5 Hz, and Amplifier is 5 m/s)

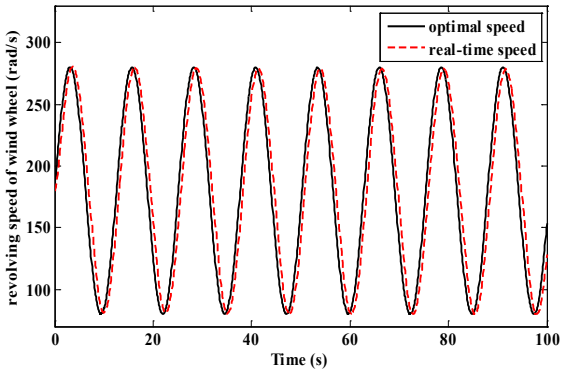

Figure 25 Feed forward control method (Frequency is 0.5 Hz, and Amplifier is 5 m/s)

When the frequency is 0.5Hz and the amplifier is 5 m/s, the dynamic control characteristics show poor performance with traditional PID control. Furthermore, the real-time speed can not reach the amplifier of the optimal speed, and the phase position of the output speed greatly lags behind the optimal signal. As is shown in Figure 25, the feed forward control method can obviously reduce the lag. What is more, precisely the real-time speed can also follow the optimal signal.

5 Conclusion

This paper provides a control method of wind power hydraulic-motor hybrid power system of beam pumping unit based on feed-forward control in order to improve the wind energy efficiency by controlling the revolving speed of wind wheel to follow the optimal control speed. Mathematical model of the wind power hydraulic-motor hybrid power system is built, and experimental station of the hybrid system is setup to verify the mathematical model. Wind speed following control method is analyzed by simulation which can be concluded that: to begin with, according to the experiment results, the mathematic model is proved to be effective; next, simulation studies show that the proposed feed-forward control method can improve the response rate as well as reduce the response lag. This research can be a reference for the application of the feed-forward control method on the hybrid power system of beam pumping unit.

Conflict of Interest: The authors declare that they have no competing interests.

Acknowledgments: This project was supported by the Science Research Foundation of Inner Mongolia University for the nationalities grant no.NMDGP1704 the Inner Mongolia nature Science Foundation (grant no.2016MS0622) National nature Science Foundation grant no.51865046,Science and technology innovation leading project of Inner Mongolia grant no.KCBJ2018028.

References

[1] M.Z..; et al. The Detailed Calculation Model of the Friction between Sucker Rod and the Liquid in the Sucker Rod

Pump Lifting System of Heavy Oil. Applied Mechanics & Materials,2014, 694.1:346-349.

[2] S.W.;et al. The design and simulation of beam pumping unit.. International Conference on Automation and Computing IEEE, 2015:1-4.

[3] L.Y.; et al. A Multifunction Energy-Saving Device With a Novel Power-Off Control Strategy for Beam Pumping Motors. IEEE Transactions on Industry Applicatio ns,2011,47.4:1605-1611.

[4] D.S.; et al. The Dynamic Simulation Model and the Comprehensive Simulation Algorithm of the Beam Pumping System. International Conference on Mechanical and Automation Engineering IEEE, 2013:118-122.

[5] G. S.G.; D.L. M. Inferring power consumption and electrical performance from motor speed in oil-well pumping units. Petroleum and Chemical Industry Conference, 1995. Record of Conference Papers. Industry Applications Society IEEE, 1997:277-283.

[6] L. H.Q; et al. An Energy Saving System for a Beam Pumping Unit. Sensors (Basel, Switzerland) 16.5(2016):685.

[7] L. H.; K.L. S; P. G. M.. Neural-network-based sensorless maximum wind energy capture with compensated power coefficient."IEEE transactions on industry applications 41.6 (2005): 1548-1556.

[8] S. Y.;S.K.; M. B.. Feedback linearization control based particle swarm optimization for maximum power point tracking of wind turbine equipped by PMSG connected to the grid. International journal of hydrogen energy 41.45 (2016): 20950-20955.

[9] R. H.; et al. A novel constant output powers compound control strategy for variable-speed variable-pitch wind turbines. IEEE Access 6 (2018): 17050-17059.

[10] J. C., C.J., and Chunying Gong. Constant-bandwidth maximum power point tracking strategy for variable-speed wind turbines and its design details. IEEE Transactions on Industrial Electronics 60.11 (2012): 5050-5058.

[11] A.K.; A. G.; et al. Current controller design for DFIG-based wind turbines using state feedback control. IET Renewable Power Generation (2019).

[12] L.J.; et al. Feedforward transient compensation control for DFIG wind turbines during both balanced and unbalanced grid disturbances. IEEE Transactions on Industry Applications 49.3 (2013): 1452-1463.

[13] V. N. W.;G. J.; and J. W.. Predictive control of an experimental wind turbine using preview wind speed measurements. Wind Energy 18.3 (2015): 385-398.

Viser Technology Pte. Ltd.
Mechanical Engineering Science
doi: 10.33142/mes.v2i2.3163

Research Article Open Access

Experimental Simulation and Verification of Position Servo Control of Mechanical Rodless Cylinder

Yeming ZHANG, Kaimin LI, Hongwei YUE, Shuangyang HE, Dongyuan LI, Kun LYU, Feng WEI

School of Mechanical and Power Engineering, Henan Polytechnic University, Jiaozuo, China

**Corresponding Author: Yeming ZHANG, E-mail: tazhangyeming@163.com*

Abstract:
In order to improve the position control accuracy of rodless cylinder, the valve control cylinder system based on pneumatic proportional servo is studied deeply. According to the working principle of the mechanical rodless cylinder control system, under the condition of uniform speed, the driving voltage of the proportional valve is changed to measure multiple sets of friction force and corresponding velocity data. Analyzed the physical structure of each component in pneumatic system, established the mathematical model of pneumatic system, and introduced MATLAB system identification toolbox to identify the parameters of the transfer function. and the experiment verifies its correctness.

Keywords: *mechanical rodless cylinder; friction characteristics; mathematical model; parameter identification*

1 Introduction

Pneumatic technology is the technology that uses compressed air as a working medium for energy and signal transmission. It is an important means to improve production efficiency and realize automation of production process in modern industry [1-3]. With the continuous progress and development of science and technology and industrial engineering, the requirements of precision operation in industrial occasions are becoming higher and higher, and the precise control of pneumatic technology is put forward higher requirements. In order to realize the accurate control of pneumatic system, it is necessary to analyze the system comprehensively. In the pneumatic valve control cylinder system, the linear model can control the mass flow equation of the valve according to the proportional direction, the mass flow continuity equation of the cylinder, and the dynamics of the cylinder. equation linearization treatment obtained [4-6].

The Pedro Luis Andrighetto[7] Lee E.Schroeder1[8], Brazil in the United States and the laboratory of Beijing Institute of Technology [9] used the test scheme of driving the load cylinder motion directly with compressed air. Zhang Baihai of Beijing Institute of Technology [10] studied the effect of temperature on cylinder friction force, and its experimental results show that the maximum static friction force, viscosity the friction coefficient decreases with the increase of temperature, while the coulomb friction force is less affected by temperature. On the basis of experiments, T. Raparelli and G. Belfore et al. of Italy used the finite element method to analyze the friction force. Through the simulation of the force and deformation of the sealing ring and the verification of the experimental results, the changes of the force and friction force of the double O seal ring and the lip seal ring under different lubrication and working pressure conditions were studied [11-14].

Liu Xiangming et al .[15] of Wuhan University of Engineering identified the third order electro-hydraulic servo system model by using the M sequence of DAQ acquisition assistant as the excitation signal of the system in LabView environment. song tao et al.[16] of nanjing university of technology established a symmetrical cylinder hydraulic system model. the input and output data of the controlled object of the system were simulated in the MATLAB. the identification model of least square method was used to identify the system, which provided a more accurate system model for further research. Kong Xiangzhen [17] of Shandong University adopted the optimal design problem in the identification process, A pseudo random sequence similar to white noise is used as input signal to continuously excite the controlled object, and the whole system is identified. The input and output experimental data are identified by MATLAB the system identification toolbox. Finally, the transfer function of the whole closed-loop system is obtained. In industrial control, the theory of system identification has been developed

for decades, and the research and application are more and more extensive, but the research and application in pneumatic servo control need to be further excavated.

Based on the friction experiment, the Stribeck friction model of the rodless cylinder is established. The mass flow equation of proportional valve, the mass flow equation of cylinder and the dynamic equation are established and linearized in the middle position of cylinder. Based on the experimental test, the input and output data of valve control cylinder are obtained, and the parameters of the transfer function obtained are identified in the MATLAB system identification toolbox.

2 Construction of Control System

The working principle of pneumatic servo position control system with mechanical rodless cylinder as control object is shown in figure 1. The industrial control computer sends out the target displacement instruction, which converts the numerical signal to the analog voltage signal of 0-10 V through the D/A conversion module, and the analog voltage signal controls the valve opening in the proportional direction. A measuring system detects the displacement of the rodless cylinder in real time and transmits the displacement signal to the data acquisition card of the industrial control computer in the form of TTL level. The air compressor produces compressed air as a source of fluid power, and flows through pneumatic triplets (air filters, pressure relief valves, oil mist) to transmit clean compressed air into proportional control valves Inside. By using the feedback deviation control, the IPC processes the feedback detection signal and the deviation value of the target value of the displacement measurement system according to the software platform LabVIEW as the upper computer to adjust the valve opening size of the proportional direction control valve in real time, and then reduce the displacement deviation of the rodless cylinder, so that the movement of the rodless cylinder finally reaches the ideal target position. Through the above principle, the pneumatic proportional servo control system can control the precise position of the mechanical rodless cylinder.

According to the experimental principle, set up the following physical experimental platform, as shown in figure 2.

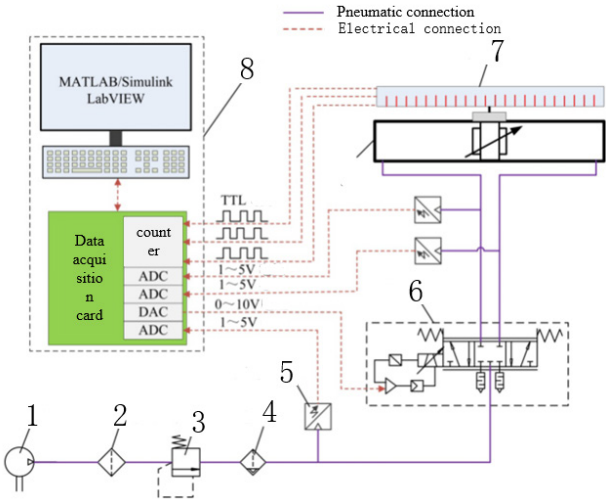

Figure 1 Schematic diagram of pneumatic servo position control system

(1-air compressor; 2-air filter; 3-air regulator; 4-air lubricator; 5-pressure transmitter; 6-proportional directional control valve; 7-Rodless cylinder; 8-IPC).

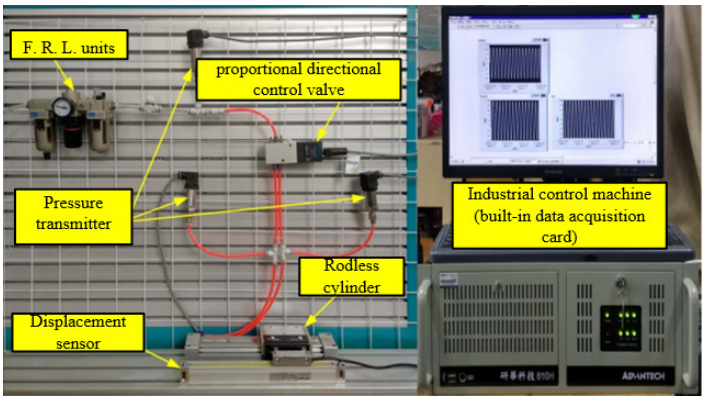

Figure 2 Experimental Platform of Servo Position Control System

This system proportional direction control valve selects the three-bit five-way proportional direction control valve produced by Germany FESTO Company as the control element, the power supply is DC 24 V, the pressure use range is 0~1 MPa, take the mechanical rodless cylinder as the end pneumatic actuator of the system. In order to ensure the accuracy of measurement and convenient installation, the displacement feedback element selected by this select the grating ruler line displacement sensor. Checking the displacement characteristics of the Slide valve requires measuring the displacement of the Side valve of the proportional control valve with the change of the driving voltage. Select the HG-C1050 model laser displacement sensor produced by Panasonic Japan is a measuring element. A pressure transducer of MIK-P300 type is selected as the measuring element. The models and parameters of each component are shown in Table 1.

Table 1 Types and working parameters of system components

Components	Model	Parameter
Air compressor	Medical Silent Piston Air Compressor	Working pressure0.4~0.7MPa
F. R. L. units	AC3000-03	Voltage regulation range0-1MPa
proportional directional control valve	MPYE-5-M5-010-B	5-bit 3-way valve, 0-10V driving voltage
Mechanical rodless cylinder	SMC MYC25G-110L	Travel itinerary110mm,Pressure range0.1-0.8MPa
Grating Displacement Sensor	JCXE-DC	Operating voltage5V,Travel itinerary 200mm
Laser displacement sensor	Panasonic HG-C1050	Scope of measurement±15mm, Precision 30μm
Pressure transmitter	MIK-P300	Range0-1.0MPa, Precision0.3%F.S.
Flow sensor	SFAB-200U-HQ8-2SV-M12	Range0-200L/min,Voltage voltage24V

3 Friction characteristics of rodless cylinder

3.1 Measurement method of friction parameters

In the servo system, the friction force always exists in the whole motion process. Compared with the driving force of compressed air, the friction force of pneumatic end actuator is relatively large, and the friction force presents nonlinearly in motion, which seriously affects the accurate positioning of cylinder position. The friction of the cylinder mainly exists in the friction between the piston and the inner wall of the cylinder, between the piston and the inner sealing belt, and between the sliding block and the external dust-proof sealing belt. When the rodless cylinder moves in a straight line at a constant speed, the acceleration is zero, and the driving force only works against friction. According to Newton's first law of motion, its mathematical expression is as follows:

$$F_f = A_a p_a - A_b p_b \quad (1)$$

Therefore, when the cylinder speed is constant, the pressure difference between the two chambers is the friction value to be measured. Under the condition of constant supply gas pressure, by changing the driving voltage of proportional valve to change the opening of valve port, the movement speed of piston will also change. In the experiment, the friction force at different speeds was measured, and the friction-velocity curve was obtained. In the Stribeck friction model, there is the maximum static friction force F_s、Coulomb friction F_c、Critical Stribeck velocity $\dot{y}_s$ And viscous friction coefficient σ A total of four parameters need to be measured [53]. The measurement method is as follows:

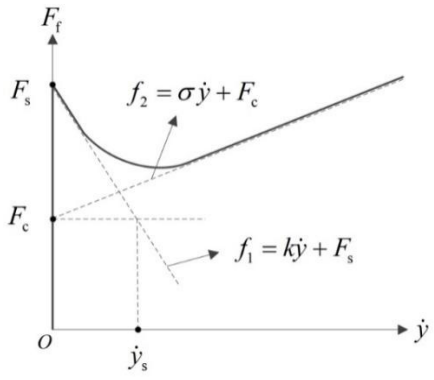

Figure 3 Stribeck friction model curve

In figure 3, in order to describe the state of friction model intuitively, auxiliary dotted lines are added. When the velocity of the piston is in the zero speed region, the total friction force is F_s. With the increase of the speed, the cylinder movement in the low speed stage can be approximately linear f_1 express. Let k is the slope of this line, and the intersection of the line and the ordinate axis is F_s. As the speed continues to increase. It is represented by a straight line σ, the slope is σ, the intersection point with the vertical axis is F_c. Cross the Coulomb friction f_2 coordinates point as the intersection point of the parallel line of the abscissa axis and the curve f_2, and then make a vertical line to the abscissa axis, the critical Stribeck velocity is the intersection of the vertical line and the abscissa axis $\dot{y}_s$.

3.2 Measurement and analysis of friction parameters

When the supply gas pressure is 0.6MPa, the pressure difference between the two chambers at different constant

speeds is measured by changing the driving voltage of the proportional directional control valve. The pressure difference of each group under uniform velocity is substituted into the corresponding friction force calculated by formula (1). Figure 4 shows the pressure difference and displacement curve of the cylinder at low speed when the driving voltage is 4.91V. The maximum static friction force can be obtained by substituting the maximum pressure difference into formula (1), and the friction force at this speed can be obtained by substituting the average pressure difference in the dotted box.It can be seen from the displacement curve that there is a small displacement before the continuous sliding of the cylinder, which is often called the displacement before sliding. The measured friction velocity of each group is summed up and fitted to form a relationship curve, as shown in figure 5. The four parameter values of Stribeck friction model obtained by making auxiliary lines are shown infigure 6. The specific parameter values are shown in table 2.

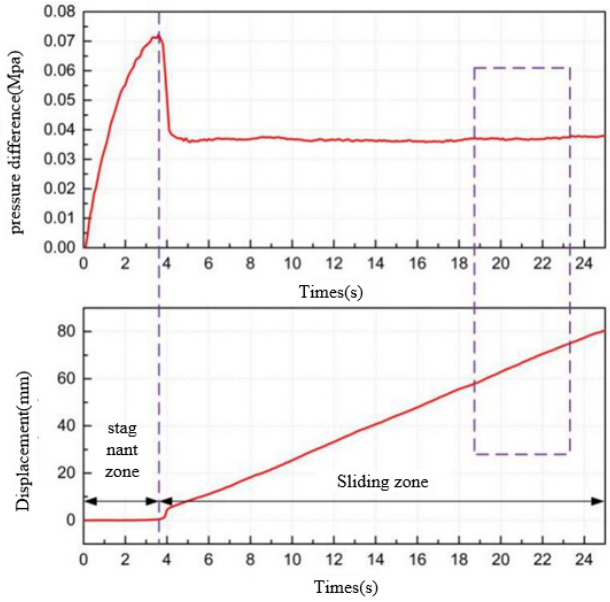

Figure 4 low speed operation process of cylinder

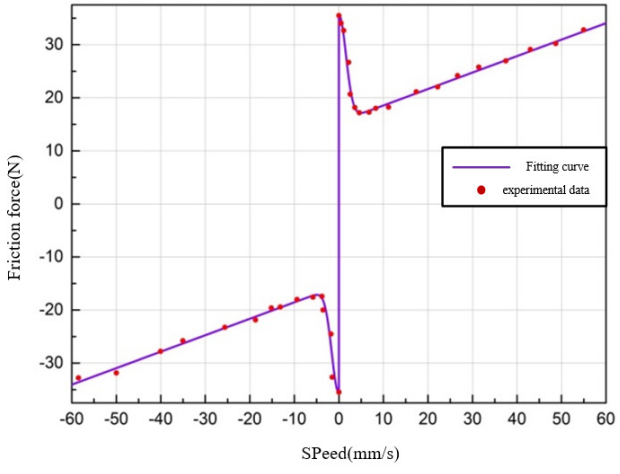

Figure 5 friction curve fitting

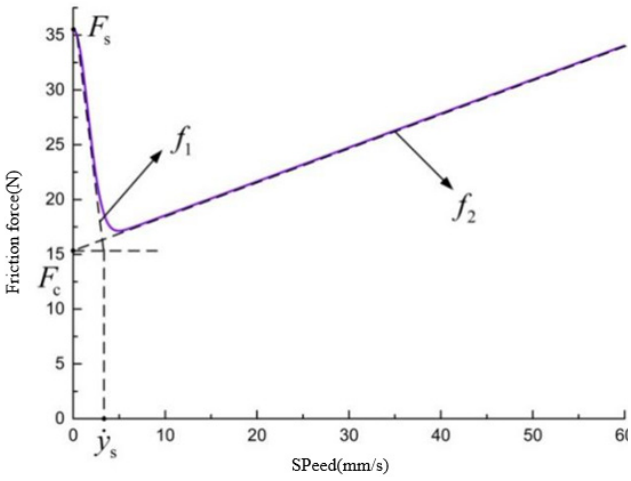

Figure 6 Friction parameter diagram

Table 2 Stribeck friction parameter values

Parameters	Value
F_s	35.48 (N)
F_c	15.31 (N)
$\dot{y}_s$	3.27 (mm/s)
σ	0.31 (N .s / mm)

4 Establishment of system model and parameter identification

4.1 Establishment of system model

By analyzing the physical structure and working principle of proportional directional control valve and rodless cylinder, the piston of rodless cylinder is connected with the external slider of cylinder mechanically, and the displacement of piston is the displacement of slider. The basic equations of valve controlled cylinder system are linearized in the middle position, and the mass flow equation of proportional valve, mass flow continuity equation of rodless cylinder and dynamic equation of are established respectively. Figure 7 describes the flow mechanism of the proportional valve controlled cylinder system. The left chamber of the proportional valve is connected with the chamber a of the cylinder, and the right chamber of the proportional valve is connected with the chamber B of the cylinder. Therefore, any chamber in the proportional valve and the corresponding connected cylinder chamber are regarded as a control body where the gas temperature and pressure are equal everywhere. The control body where the left chamber of the cylinder is located is chamber a, and the control body where the right chamber of the gas cylinder is located is chamber B. the gas flow process in the whole valve controlled cylinder system can be seen It is the process that the gas flows through the proportional valve to charge and deflate a and B cavities. Set the proportional spool slide to move to the right as a positive direction. When the valve core of the proportional directional valve moves in the positive direction, chamber

a is filled with air and cavity B is deflated, and the cylinder piston moves to the right.

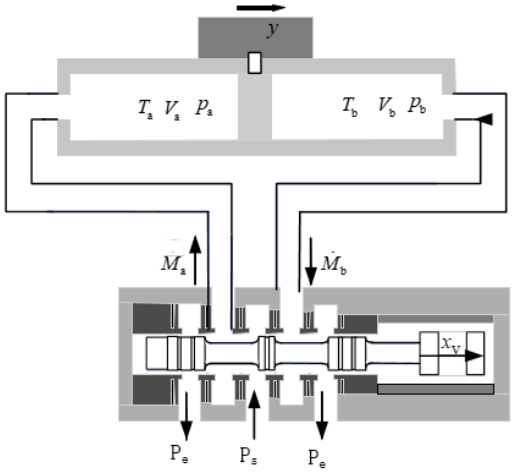

Figure 7 Flow mechanism of valve control cylinder

In figure 7, p_s indicates supply gas pressure, $\dot{M}_a$ and $\dot{M}_b$ indicates mass flow in A and B chambers respectively, p_a and p_b indicates the pressure in A and B chambers respectively, T_a and T_b indicates the temperature of A and B cavity respectively, V_a and V_b indicates the volume of A and B cavity respectively, x_v represents proportional spool displacement, y indicates cylinder piston displacement.

4.1.1 Proportional Valve Mass Flow Equation

Because the valve clearance is very small, the mass flow through the gas flow clearance is very small in actual application, so it can be ignored in establishing the model. It is assumed that the working medium is ideal gas satisfying the ideal gas state equation and the gas flow process is isentropic adiabatic process, neglecting the leakage of clearance between spool and sleeve. When the spool moves to the right, the gas in the a-chamber pushes the piston to the right and the piston drives the slider to move synchronously. Figure 8 shows the relative position of the circular orifice to the proportional shoulder.

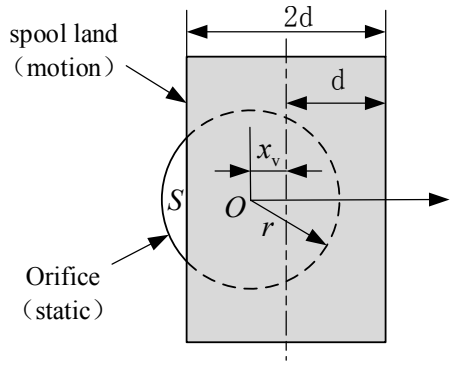

Figure 8 Relative motion position of the shoulder of proportional valve element and the orifice

In figure 8 , r indicates the radius of the orifice, $2d$ is the shoulder width of proportional spool, x_v indicates displacement of shoulder relative to orifice, S represents the geometric cross-sectional area of the orifice opening, From the geometric relation in the figure, the expression of the geometric section area S can be obtained as follows:

$$S=\begin{cases}0 & x_v \le d-r \\ r^2\arccos\dfrac{d-x_v}{r}-(d-x_v)\sqrt{r^2-(d-x_v)^2} & d-r<x_v\le d\end{cases} \tag{2}$$

Based on aerodynamics, considering the shrinkage and friction losses of the orifice, the mass flow through the cylinder a-chamber is as follows [54, 55]:

$$\dot{M}_a=\begin{cases}CS\dfrac{p_s}{\sqrt{RT_s}}\sqrt{\dfrac{2\kappa}{\kappa-1}\left[\left(\dfrac{p_a}{p_s}\right)^{\frac{2}{\kappa}}-\left(\dfrac{p_a}{p_s}\right)^{\frac{\kappa+1}{\kappa}}\right]} & \left(\dfrac{p_a}{p_s}\ge c_0\right) \\ CS\dfrac{p_s}{\sqrt{RT_s}}\sqrt{\dfrac{2\kappa}{\kappa+1}\left(\dfrac{2}{\kappa+1}\right)^{\frac{2}{\kappa-1}}} & \left(\dfrac{p_a}{p_s}<c_0\right)\end{cases} \tag{3}$$

The mass flow through the b-chamber of the cylinder is:

$$\dot{M}_b=\begin{cases}-CS\dfrac{p_b}{RT_b}\sqrt{\dfrac{2\kappa}{\kappa-1}\left[\left(\dfrac{p_e}{p_b}\right)^{\frac{2}{\kappa}}-\left(\dfrac{p_e}{p_b}\right)^{\frac{\kappa+1}{\kappa}}\right]} & \left(\dfrac{p_e}{p_b}\ge c_0\right) \\ -CS\dfrac{p_b}{RT_b}\sqrt{\dfrac{2\kappa}{\kappa+1}\left(\dfrac{2}{\kappa+1}\right)^{\frac{2}{\kappa-1}}} & \left(\dfrac{p_e}{p_b}<c_0\right)\end{cases} \tag{4}$$

In the formula, R is the gas constant, C is the flow coefficient of the gas through the orifice, κ is the isentropic index,critical pressure ratio $c_0=\left[\dfrac{\kappa+1}{2}\right]^{\frac{\kappa}{1-\kappa}}$.

From Taylor's linearization formulas (3) and (4):

$$\begin{cases}\Delta\dot{M}_a=c_1\Delta x_v-c_2\Delta p_a \\ \Delta\dot{M}_b=-c_1\Delta x_v-c_2\Delta p_b\end{cases} \tag{5}$$

In the formula, c_1 represents the mass flow gain of a proportional valve; c_2 denotes the mass flow pressure coefficient .Since symmetric proportional valves are used, c_1 and c_2 under initial steady state conditions are represented as follows:

$$\begin{cases}c_1=\left.\dfrac{\partial\dot{M}_a}{\partial x_v}\right|_{\substack{p_a=p_0\\x_{v=0}}}\approx-\left.\dfrac{\partial\dot{M}_b}{\partial x_v}\right|_{\substack{p_b=p_0\\x_{v=0}}} \\ c_2=-\left.\dfrac{\partial\dot{M}_a}{\partial p_a}\right|_{\substack{x_{v=0}\\p_a=p_0}}\approx-\left.\dfrac{\partial\dot{M}_b}{\partial p_b}\right|_{\substack{x_{v=0}\\p_b=p_0}}\end{cases} \tag{6}$$

Equation (5) can also be written

$$\Delta\dot{M}_a-\Delta\dot{M}_b=2c_1\Delta x_v-c_2\left(\Delta p_a-\Delta p_b\right) \tag{7}$$

4.1.2 Mass flow equation of cylinder

According to the law of conservation of mass flow, under the isentropic condition, the mass flow of the two chambers in a cylinder is equal to the gas mass in and out of the two chambers in a unit time [56].

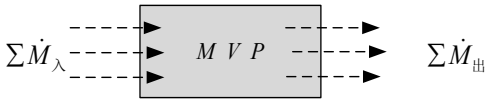

Figure 9 compressed flow into and out of a control body

$$\sum \dot{M}_{入}-\sum \dot{M}_{出}=\frac{\mathrm{d}M}{\mathrm{d}t}=\frac{\mathrm{d}(\rho V)}{\mathrm{d}t}=\rho\frac{\mathrm{d}V}{\mathrm{d}t}+V\frac{\mathrm{d}\rho}{\mathrm{d}t} \tag{8}$$

The continuous equation for the mass flow of the cylinder cavities A and B is as follows:

$$\begin{cases}\dot{M}_{\mathrm{a}}=\rho_{\mathrm{a}}\dfrac{\mathrm{d}V_{\mathrm{a}}}{\mathrm{d}t}+V_{\mathrm{a}}\dfrac{\mathrm{d}\rho_{\mathrm{a}}}{\mathrm{d}t}\\ \dot{M}_{\mathrm{b}}=\rho_{\mathrm{b}}\dfrac{\mathrm{d}V_{\mathrm{b}}}{\mathrm{d}t}+V_{\mathrm{b}}\dfrac{\mathrm{d}\rho_{\mathrm{b}}}{\mathrm{d}t}\end{cases} \tag{9}$$

The ideal state equation $\rho = p / RT$ of gas is substituted by formula (9) to obtain:

$$\begin{cases}\dot{M}_{\mathrm{a}}=\dfrac{1}{RT_{\mathrm{a}}}\left(p_{\mathrm{a}}\dfrac{\mathrm{d}V_{\mathrm{a}}}{\mathrm{d}t}+V_{\mathrm{a}}\dfrac{\mathrm{d}p_{\mathrm{a}}}{\mathrm{d}t}-\dfrac{p_{\mathrm{a}}V_{\mathrm{a}}}{T_{\mathrm{a}}}\dfrac{\mathrm{d}T_{\mathrm{a}}}{\mathrm{d}t}\right)\\ \dot{M}_{\mathrm{b}}=\dfrac{1}{RT_{\mathrm{b}}}\left(p_{\mathrm{b}}\dfrac{\mathrm{d}V_{\mathrm{b}}}{\mathrm{d}t}+V_{\mathrm{b}}\dfrac{\mathrm{d}p_{\mathrm{b}}}{\mathrm{d}t}-\dfrac{p_{\mathrm{b}}V_{\mathrm{b}}}{T_{\mathrm{b}}}\dfrac{\mathrm{d}T_{\mathrm{b}}}{\mathrm{d}t}\right)\end{cases} \tag{10}$$

From the isentropic condition:

$$T=T_0\left(\frac{p}{p_0}\right)^{\frac{\kappa-1}{\kappa}} \tag{11}$$

In the formula, T_0 represents the initial temperature, p_0 represents initial pressure.Formula (12) can be derived from time by formula (11):

$$\frac{\mathrm{d}T}{\mathrm{d}t}=\frac{\kappa-1}{\kappa}\frac{T_0}{p_0}\left(\frac{p}{p_0}\right)^{\frac{1}{k}}\frac{\mathrm{d}p}{\mathrm{d}t}=\frac{\kappa-1}{\kappa}\frac{T_0}{p}\left(\frac{p}{p_0}\right)^{\frac{\kappa-1}{\kappa}}\frac{\mathrm{d}p}{\mathrm{d}t}=\frac{\kappa-1}{\kappa}\frac{T}{p}\frac{\mathrm{d}p}{\mathrm{d}t} \tag{12}$$

Formula (12) can be obtained by substituting it for formula (10):

$$\begin{cases}\dot{M}_{\mathrm{a}}=\dfrac{1}{RT_{\mathrm{a}}\kappa}\left(V_{\mathrm{a}}\dfrac{\mathrm{d}p_{\mathrm{a}}}{\mathrm{d}t}+\kappa p_{\mathrm{a}}\dfrac{\mathrm{d}V_{\mathrm{a}}}{\mathrm{d}t}\right)\\ \dot{M}_{\mathrm{b}}=\dfrac{1}{RT_{\mathrm{b}}\kappa}\left(V_{\mathrm{b}}\dfrac{\mathrm{d}p_{\mathrm{b}}}{\mathrm{d}t}+\kappa p_{\mathrm{b}}\dfrac{\mathrm{d}V_{\mathrm{b}}}{\mathrm{d}t}\right)\end{cases} \tag{13}$$

Because the piston position in the middle of the cylinder is representative of the dynamic characteristics[57], assuming that the parameter of the cylinder piston at the stable working point in the middle is set to the initial value under small interference, the formula (14) can be obtained. The lower corners 0a and 0b indicate the initial state of chamber a and b, respectively, T_{s} for supply air temperature, V_0 is half the total cylinder volume, p_0 is the initial equilibrium pressure of the two chambers when the piston is in steady state.

$$\begin{cases}\dot{M}_{\mathrm{a}}=0+\Delta\dot{M}_{\mathrm{a}},\quad \dot{M}_{\mathrm{b}}=0+\Delta\dot{M}_{\mathrm{b}}\\ p_{\mathrm{a}}=p_{0\mathrm{a}}+\Delta p_{\mathrm{a}},\quad p_{\mathrm{b}}=p_{0\mathrm{b}}+\Delta p_{\mathrm{b}}\\ V_{\mathrm{a}}=V_{0\mathrm{a}}+\Delta V_{\mathrm{a}},\quad V_{\mathrm{b}}=V_{0\mathrm{b}}+\Delta V_{\mathrm{b}}\\ T_{\mathrm{a}}=T_{0\mathrm{a}}+\Delta T_{\mathrm{a}},\quad V_{\mathrm{b}}=T_{0\mathrm{b}}+\Delta T_{\mathrm{b}}\end{cases} \tag{14}$$

Initial values and have the following relationships:

$$\begin{cases}\Delta\dot{V}_{\mathrm{a}}=-\Delta\dot{V}=A\Delta\dot{y}\\ T_{0\mathrm{a}}=T_{0\mathrm{b}}=T_{\mathrm{s}}\\ V_{0\mathrm{a}}=V_{0\mathrm{b}}=V_0\\ p_{0\mathrm{a}}=p_{0\mathrm{b}}=p_0\end{cases} \tag{15}$$

Since the incremental values of each physical quantity are small relative to the initial values under small disturbances, they can be neglected in the calculation[58]. Therefore, the incremental expression of the continuous equation for the gas mass flow in the cylinder is as follows:

$$\begin{cases}\Delta\dot{M}_{\mathrm{a}}=\dfrac{1}{RT_{\mathrm{s}}\kappa}\left[V_0\dfrac{\mathrm{d}(\Delta p_{\mathrm{a}})}{\mathrm{d}t}+\kappa p_0 A\Delta\dot{y}\right]\\ \Delta\dot{M}_{\mathrm{b}}=\dfrac{1}{RT_{\mathrm{s}}\kappa}\left[V_0\dfrac{\mathrm{d}(\Delta p_{\mathrm{b}})}{\mathrm{d}t}-\kappa p_0 A\Delta\dot{y}\right]\end{cases} \tag{16}$$

Equation (16) can also be written:

$$\Delta\dot{M}_{\mathrm{a}}-\Delta\dot{M}_{\mathrm{b}}=\frac{1}{RT_{\mathrm{s}}\kappa}\left\{V_0\left[\frac{\mathrm{d}(\Delta p_{\mathrm{a}})}{\mathrm{d}t}-\frac{\mathrm{d}(\Delta p_{\mathrm{b}})}{\mathrm{d}t}\right]+2\kappa p_0 A\Delta\dot{y}\right\} \tag{17}$$

4.1.3 Dynamic equation of cylinder

In figure 7, according to Newton's second theorem, the pressure difference between the chambers a and B is the power that drives the piston movement. The dynamic equation of the cylinder is as follows:

$$A\left(p_{\mathrm{a}}-p_{\mathrm{b}}\right)=M_{\mathrm{L}}\ddot{y}+F_{\mathrm{L}}+F_{\mathrm{f}} \tag{18}$$

Inside, M_{L} represents the mass of the piston and its moving parts, F_{L} is the external load force, F_f represents the total friction force in motion.

4.1.4 Block diagram and transfer function of valve controlled cylinder system

The linear model of the whole system can be composed of the mass flow equation of proportional directional control valve (7), the mass flow continuity equation of cylinder (17), and the dynamic equation of cylinder (18).

$$\begin{cases}\dot{M}_{\mathrm{a}}-\dot{M}_{\mathrm{b}}=2c_1x_{\mathrm{v}}-c_2\left(p_{\mathrm{a}}-p_{\mathrm{b}}\right)\\ \dot{M}_{\mathrm{a}}-\dot{M}_{\mathrm{b}}=\dfrac{1}{RT_{\mathrm{s}}\kappa}\left[V_0\left(\dfrac{\mathrm{d}p_{\mathrm{a}}}{\mathrm{d}t}-\dfrac{\mathrm{d}p_{\mathrm{b}}}{\mathrm{d}t}\right)+2\kappa p_0 A\dot{y}\right]\\ A\left(p_{\mathrm{a}}-p_{\mathrm{b}}\right)=M_{\mathrm{L}}\ddot{y}+F_{\mathrm{L}}+F_{\mathrm{f}}\end{cases} \tag{19}$$

Make the pressure difference $p_{\mathrm{L}}=p_{\mathrm{a}}-p_{\mathrm{b}}$, Mass flow difference $\dot{M}_{\mathrm{L}}=\dot{M}_{\mathrm{a}}-\dot{M}_{\mathrm{b}}$,The formula (19) is transformed by pulling:

$$\begin{cases}\dot{M}_{\mathrm{L}}(s)=2c_1x_{\mathrm{v}}(s)-c_2p_{\mathrm{L}}(s)\\ \dot{M}_{\mathrm{L}}(s)=\dfrac{1}{RT_{\mathrm{s}}\kappa}\left[V_0sp_{\mathrm{L}}(s)+2\kappa p_0Asy(s)\right]\\ Ap_{\mathrm{L}}(s)=M_{\mathrm{L}}s^2y(s)+F_{\mathrm{L}}(s)+F_{\mathrm{f}}(s)\end{cases} \tag{20}$$

The block diagram of valve controlled cylinder system can be obtained from formula (20), as shown in figure 10.

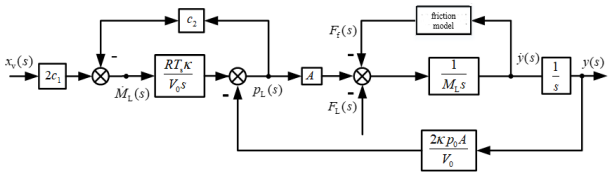

Figure 10 Block diagram of the valve-controlled cylinder system

The transfer function of the valve controlled cylinder system can be obtained by solving the simultaneous basic equations or by simplifying the block diagram.

(1) Transfer function of spool displacement x_v to cylinder output displacement y.

When F_f=0 and $F_L = 0$, the transfer function of spool displacement x_v to output displacement y can be obtained as follows:

$$\frac{y_x(s)}{x_v(s)} = \frac{K_T\omega_n^2}{s\left(s^2 + 2\zeta\omega_n s + \omega_n^2\right)} \tag{21}$$

Among, the gain K_T is:

$$K_T = \frac{c_1 R T_s}{p_0 A} \tag{22}$$

The damping ratio ζ is:

$$\zeta = \frac{c_2 R T_s}{2A}\sqrt{\frac{\kappa M_L}{2V_0 p_0}} \tag{23}$$

The natural frequency ω_n is:

$$\omega_n = \sqrt{\frac{2\kappa p_0 A^2}{V_0 M_L}} \tag{24}$$

When x_v=0 and $F_L = 0$, it can be obtained that the transfer function of the friction force F_f to the output displacement y is:

$$\frac{y_f(s)}{F_f(s)} = -\frac{\frac{K_T\omega_n^2}{2c_1 A}\left(\frac{V_0}{RT_s\kappa}s + c_2\right)}{s\left(s^2 + 2\zeta\omega_n s + \omega_n^2\right)} \tag{25}$$

In the same way, when $F_f = 0$ and $F_f = 0$, it can be obtained that the transfer function of friction force y to output displacement y is:

$$\frac{y_L(s)}{F_L(s)} = -\frac{\frac{K_T\omega_n^2}{2c_1 A}\left(\frac{V_0}{RT_s\kappa}s + c_2\right)}{s\left(s^2 + 2\zeta\omega_n s + \omega_n^2\right)} \tag{26}$$

Therefore, the total transfer function of the valve controlled cylinder system is:

$$y(s) = y_x(s) + y_f(s) + y_L(s)$$

$$= \frac{K_T\omega_n^2 x_v(s) - \frac{K_T\omega_n^2\left[F_f(s) + F_L(s)\right]}{2c_1 A}\left(\frac{V_0}{RT_s\kappa}s + c_2\right)}{s\left(s^2 + 2\zeta\omega_n s + \omega_n^2\right)} \tag{27}$$

Because the proportional directional valve has strong linear characteristics, the transfer function can be described as follows:

$$\frac{x_v(s)}{U(s)} = K_v \tag{28}$$

In the formula, K_v represents proportional gain, U indicates the drive voltage of the valve.

The transfer function of the proportional amplifier is:

$$\frac{U(s)}{y_{in}(s) - y(s)} = K_a \tag{29}$$

In the formula, K_a represents proportional gain, y_{in} represents the input displacement.

Friction compensation is used to reduce the influence of friction on the system. According to the formulas (27), (28), (29), the block diagram of the cylinder servo system can be obtained as shown in figure 11.

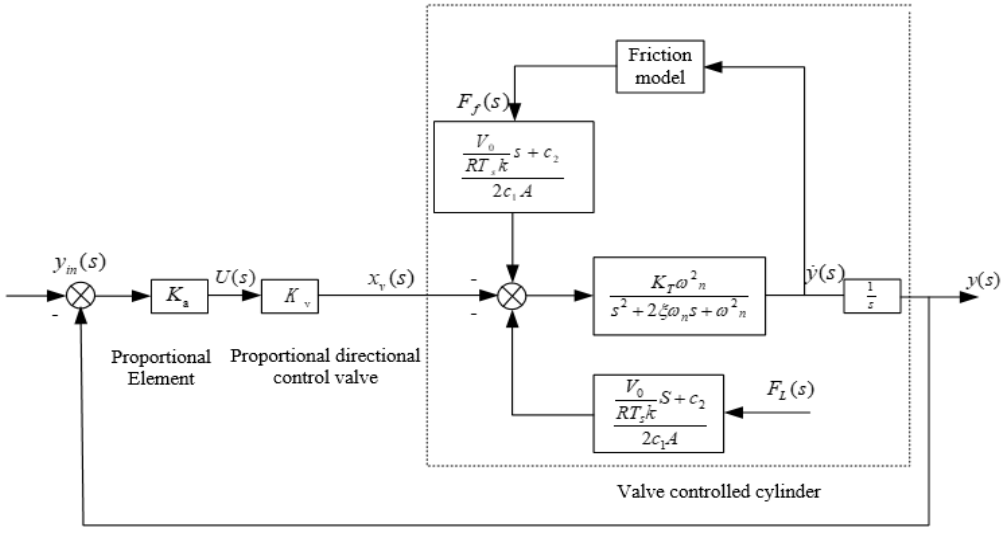

Figure 11 Block Diagram of Cylinder Position Servo System

Therefore, the open-loop transfer function of the system is:

$$H(z) = \frac{b_1 z^3 + b_2 z^2 + b_3 z + b_4}{a_1 z^3 + a_2 z^2 + a_3 z + a_4} \tag{30}$$

Formula (4-29) is discretized and its open-loop transfer function is obtained as follows:

$$H(z) = \frac{b_1 z^3 + b_2 z^2 + b_3 z + b_4}{a_1 z^3 + a_2 z^2 + a_3 z + a_4} \tag{31}$$

In the formula, b_1, b_2 , b_3 , b_4 and a_1 , a_2 , a_3, a_4 are constant values.

4.2 Valve-controlled cylinder system identification

4.2.1 System Identification Process

System identification can be divided into open loop identification and closed loop identification. Closed-loop identification methods are divided into closed-loop direct identification and closed-loop indirect identification. The closed-loop indirect identification method is to identify the closed-loop transfer function of the whole system first,

then subtract the feedback link of the system to obtain the open-loop transfer function of the system. This method is cumbersome due to the elimination of intermediate links. Closed-loop direct identification method is to identify the open-loop transfer function of controlled object under closed-loop condition. Since the linearized system model is a third-order model and the proportional valve-controlled cylinder system has an integral part and is an open-loop unstable system, this paper uses closed-loop condition to directly identify the open-loop transfer function of the system.

M-sequence is a binary pseudo-random code sequence of approximate white noise signals as shown in figure 12. M-sequence as interference signal can fully excite the characteristics of the controlled object. The input signal is the superposition of the controller output signal and M-sequence signal, and the output signal is the cylinder displacement signal. To identify the input signal and output displacement before and after the object, the open loop system of the system is identified. Figure 13 is the identification test schematic.

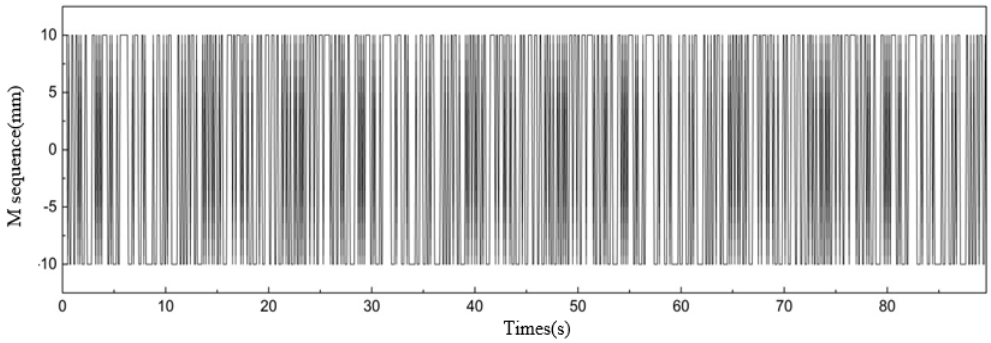

Figure 12 M-sequence signal

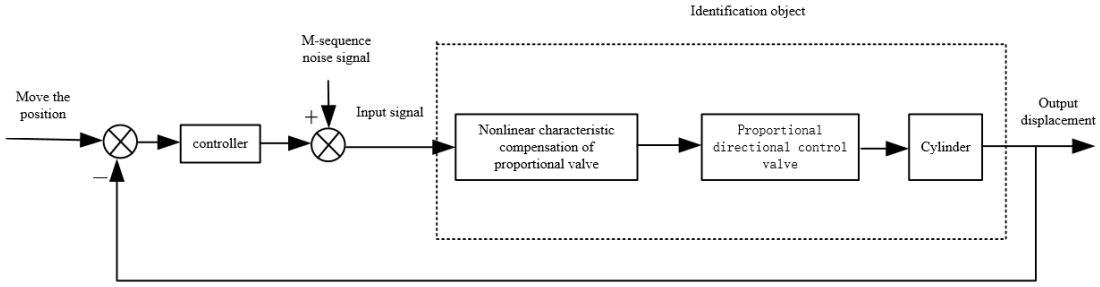

Figure 13 Identification test schematic diagram

For nonlinear systems, a parametric linearization model can be established based on the perturbation theory. During the identification process, the cylinder piston is allowed to move to the left and right, and the "near disturbance" of the input signal to the system should be in both positive and negative directions. The amplitude of input signal is not too small, it will slow down the response of the system, not fully excite the dynamic characteristics of the system and make the system identify distortion, but it should not be too large, so the input signal should be selected reasonably. Identified input and output signals are shown in figure 14.

In MATLAB, input signal and output signal are imported separately. ARX discrete transfer function model is selected for identification in time domain. The identification results are shown in figure 15.

The identified system model is:

$$H(z) = \frac{0.1496z^2 - 0.03607z + 0.1678}{z^3 - 1.4276z^2 + 0.85537z - 0.4243} \quad (32)$$

4.2.2 Experimental verification of system identification model

According to the system schematic diagram built as shown in figure 16, the input step signal and sinusoidal displacement signal are experimentally verified. Figure 17 is a comparison diagram of the results of simulation and experiment. It can be concluded that the identified system model can well reflect the dynamic characteristics of the control system.

From the previous section 4.1 (Establishment of system model) the theoretical model of the system is obtained. Under the standard input signal (step signal and sinusoidal signal), the position control of the rodless cylinder is studied experimentally, and the actual input and output data curve of the rodless cylinder is obtained. Based on the input and output data of the rodless cylinder system, the identification model of the rodless cylinder system is obtained by using the MATLAB system identification toolbox. Finally, with the identification model as the system and the standard input signal as the excitation, the experimental curve and the simulation curve are tracked.

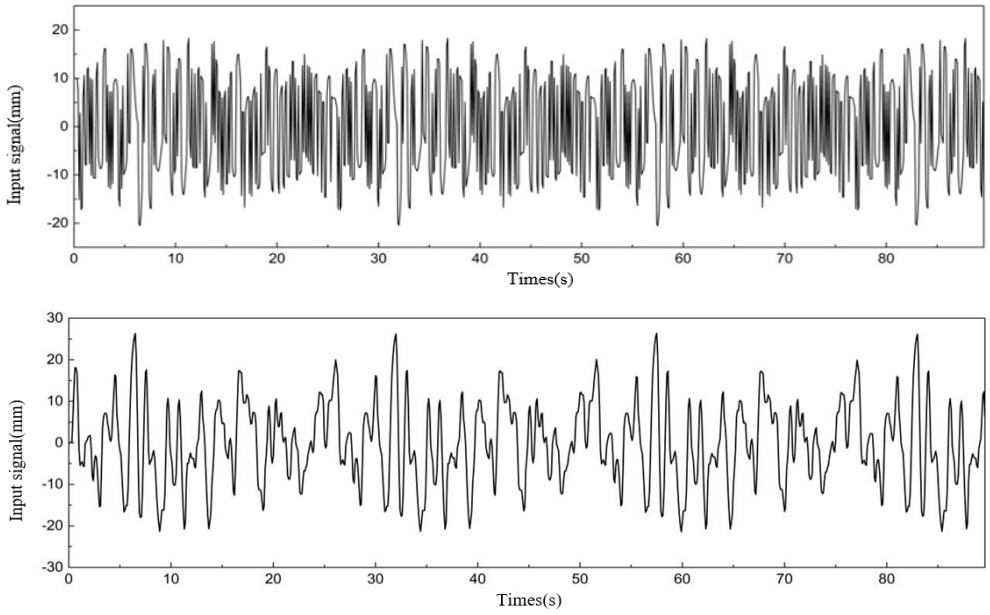

Figure 14 identification of input and output signals

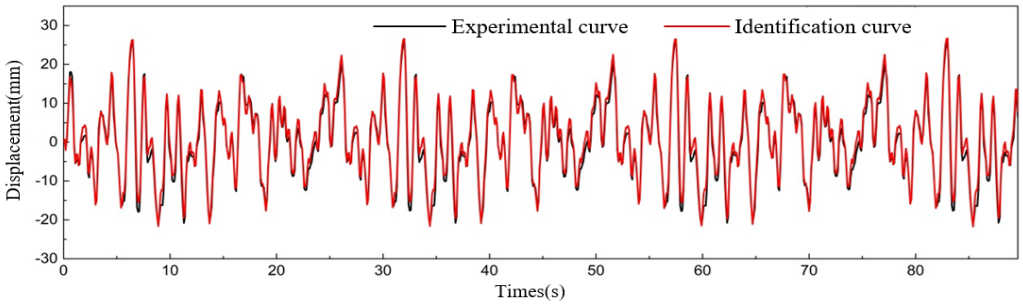

Figure 15 Identification result

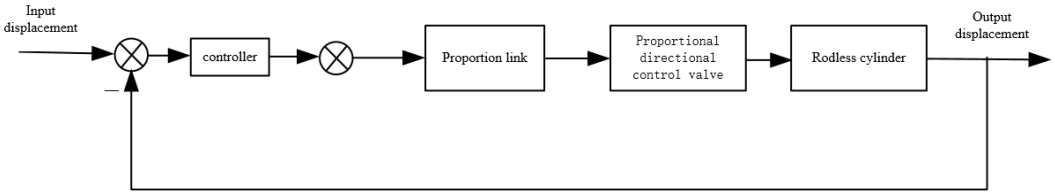

Figure 16 system principle block diagram

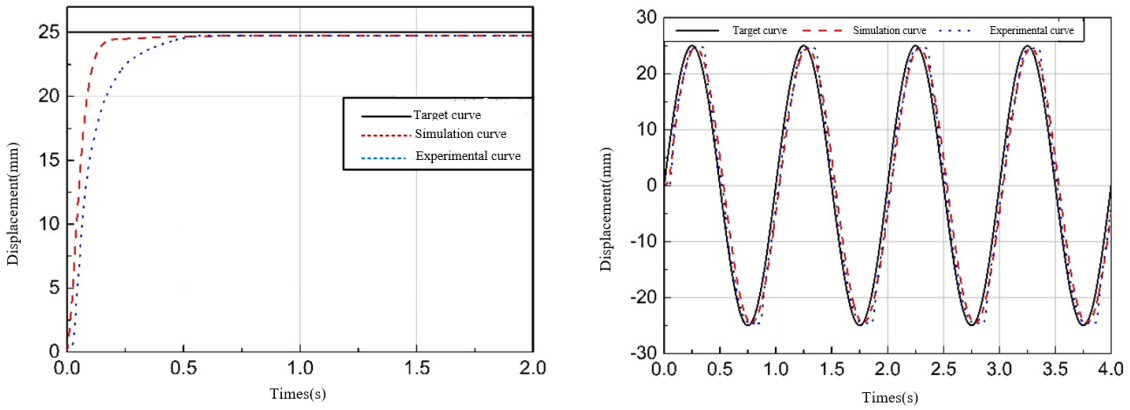

(a) Positioning result; (b) Position tracking result

Figure 17 Comparisons between simulation and experiment

5 Conclusions

Based on the experimental system of position servo control of rodless cylinder, the conclusion is as follows :(1) The friction model of Stribeck mechanical rodless cylinder is established. (F_s=35.48N, F_c=15.31N ,$\dot{y}_s$=3.27*mm/s*, σ=3.27*mm/s*) ; (2) By establishing the mass flow equation of proportional control valve, mass flow equation and dynamic equation of cylinder, and reducing the influence of friction on the system by friction compensation, the accurate mathematical model of proportional control cylinder system is finally established .(3) The input and output data of valve control cylinder are obtained by experimental test, and the parameters of the system transfer function obtained by MATLAB system box identification to used to verify the correctness of the system model.

Author Contributions: Conceptualization, Yeming ZHANG and Hongwei YUE; Data curation, Kaimin LI; Funding acquisition, Yeming ZHANG; Project administration, Yeming ZHANG; Software, Shuangyang HE and Dongyuan LI; Supervision, Kun LYU and Feng WEI; Writing—original draft, Kaimin LI and Hongwei YUE; Writing—review & editing, Yeming ZHANG and Kaimin LI.

Conflict of Interest: The authors declare no conflict of interest.

Funding: The paper is Supported by Henan Province Science and Technology Key Project (Grant No. 202102210081), the Fundamental Research Funds for Henan Province Colleges and Universities (Grant No. NSFRF140120), Doctor Foundation of Henan Polytechnic University (Grant No.B2012-101).

Acknowledgments: The authors would like to thank Henan Polytechnic University and Beihang University for providing the necessary facilities and machinery to build the prototype of the pneumatic servo system. The authors are sincerely grateful to the reviewers for their valuable review comments, which substantially improved the paper.

References

[1] SMC (China) Co., Ltd. Modern Practical Pneumatic Technology[M]. Beijing: Machinery Industry Press ,2008.

[2] Ming Y. Air compressor efficiency in a Vietnamese enterprise [J]. Energy Policy, 2009, 37(6): 2327-2337.

[3] Zhang Yeming, Cai Maolin. Overall Life Cycle Comprehensive Assessment of Pneumatic and Electric Actuator[J]. Chinese Journal of Mechanical Engineering, 2014, 27(3):584-594.

[4] Zhang Y, Li K, Wei S, et al. Pneumatic Rotary Actuator Position Servo System Based on ADE-PD Control [J]. Applied Sciences, 2018, 8(3): 406.

[5] Yeming Zhang, Ke Li, Geng Wang, Maolin Cai. Nonlinear model establishment and experimental verification of a pneumatic rotary actuator position servo system[J]. Energies 2019, 12(6), 1096.

[6] Yeming Zhang, Hongwei YUE, Ke Li, Maolin Cai. Analysis of power matching on energy saving of pneumatic rotary actuator servo-control system[J]. Chinese Journal of Mechanical Engineering, 2020, 33:30.

[7] Pedro Luís Andrighetto, Antonio Carlos Valdiero, Leonardo Carlotto. Study of the frictionbehavior in industrial pneumatic actuators. ABCM Symposium Series in Mechatronics,2006, 2: 369-376.

[8] Lee E. Schroederl. Experimental Study of Friction in a Pneumatic Actuator at ConstantVelocity. Journal of Dynamic Systems, Measurement, and Control, 1993, 9,Vol. 115:575-577.

[9] Zhang Baihai, Cheng Haifeng, Ma Yanfeng. Experimental study of cylinder friction. Beijing Institute of Technology Journal ,2005,(6):483-487.

[10] Zhang Baihai, Peng Guangzheng, Liu Qiong, Study on the Influence of Temperature on Friction Characteristics of Cylinder.

[11] T. Raparelli, A. Manuello, Bertettot and L. Mazzat. Experimental and Numerical Study ofFriction in an Electrometric Seal for Pneumatic Cylinders. Tribology International. 1997,Volume 30 Number 7: 547-557.

[12] Belforte. G Raparelli. T, Velardocchia. M. Study of the Behavior of Lip Seals in PneumaticActuators.. Lubr. Eng,1993, 45: 775-780.

[13] Conte M, Manuello A, Mazza L, Visconte C. Measurement of contact pressure in pneumaticactuator seals. In: Proceedings of the AITC-AIT 2006 international conference on tribology,2006.

[14] G. Belforte, M. Conte, A. Manuello Bertetto, L. Mazza, C. Visconte. Experimental andnumerical evaluation of contact pressure in pneumatic seals. Tribology International. 2009,42:169- 175.

[15] Liu Xiangming, Li Liang. LabVIEW Electro-hydraulic System Identification [J]. Machine and Hydraulic ,2007,35(9):143-145.

[16] Song Tao, Yu Cungui. Simulation based on MATLAB/ Simulink hydraulic servo system identification [J]. Hydraulic and Pneumatic ,2015,(10):120-123.

[17] Kong Xiangzhen. Dynamic Characteristics and Control of Pneumatic Proportional System [D]. Jinan; Shandong University ,2007.

Viser Technology Pte. Ltd.
Mechanical Engineering Science
doi: 10.33142/mes.v2i2.3164

Research Article Open Access

Integration of measurement and simulation of film pressure for estimating deformation of a glass sheet on a noncontact air conveyor

Rui YANG[1,2], Wei ZHONG[1,2*], Rongyue WANG[1,2], Chong LI[1,2], Jiwen FANG[3]

1. School of Mechanical Engineering, Jiangsu University of Science and Technology, Zhenjiang, China
2. Jiangsu Provincial Key Laboratory of Advanced Manufacturing for Marine Mechanical Equipment, Jiangsu University of Science and Technology, Zhenjiang, China

**** Corresponding author:*** *Wei ZHONG, Email: zhongwei@just.edu.cn*

Abstract:
Recently, large and thin glass substrates are transported by air film conveyors to reduce surface damage. On the production line, the glass substrates are desired to be transported flatly on the conveyor to ensure the quality inspection. A method by feedbacking film pressure to the theoretical model is proposed for estimation of the deformation of the glass sheet, and the validity of the method is theoretically and experimentally verified. First, a theoretical model including the flow behavior through a porous-walled gap is established, and the film pressure distribution can be predicted by solving the model. Then, an experimental setup that can simultaneously measure the film pressure and the flatness of the glass sheet is established, and, the validity of the model is verified experimentally. Next, with the pressure points at the grooves as the boundary and the pressure points at the flange area as the feedback, an algorithm is applied to shape the one-dimensional deformation at the centerlines in accordance with a quadratic curve. Furthermore, two-dimensional deformation of the glass sheet can then be estimated by an interpolation operation. Comparisons of the calculated results with the experimental data verify the effectiveness of the estimating method.

Keywords: *Deformation of glass sheet; air conveyor; air film; pressure distribution; pressure feedback*

1 Introduction

Surface scratching and damage easily occur during transportation of glass substrates for liquid-crystal display (LCD). Contactless transport using pneumatic technology can eliminate these problems since air flow is magnetic free and clean[1–4]. For example, air tracks with arrays of bearing elements equipped on the surface are in use to supply pressurized air beneath flat objects. The air flow into the gap and form a pressurized film to levitate the object at a certain height, which is determined by the supply flow rate. This method is extremely suitable for the transport of large and fragile glass substrates.

Manufacturers intend to increase the size of the glass substrate to reduce costs[5]. The tenth generation thin flat panel glass substrate reaches a size of 3.1 m long by 2.8 m wide. On the production line, high-speed cameras are used to inspect the quality defects of the glass panel. Figure 1 gives a sketch of a noncontact transport system for inspecting the surface quality of the glass substrate. In the case that there exists an apparent deformation at some places, the detecting position cannot be clearly imaged due to the low focus depth of the camera. Figure 1 shows the situation that the deformation place cannot be clearly imaged. As a result, there is crucial need to monitor the deformation rapidly and accurately. Although multiple laser sensors can be used to achieve this, it is difficult to realize rapid measurement over a wide range.

Researchers have developed non-contact conveyor systems for transporting large glass substrates. Im et al. [6] studied the influences from nozzles of different shapes to the air cushion and determined the optimum design. Amano et al. [7] employed porous media to replace the orifice in order to eliminate the wave deformation. Oiwa et al. [8] designed a contactless air conveyor using porous pads as restrictors, and reported the numerical results of the deformation of the glass sheet. Miyatake et al. [9] studied the relation between the deformation and the supply pressure during transportation of the glass sheet. Above research indicate that the film pressure is closely related to the glass deformation.

Finite element method (FEM) software can be used to calculate the deformation of the glass sheet. However, the calculation takes a long time, and, the actual practice needs a fast estimating method. Researchers sought methods to integrate the measured experimental data with the computation not only to enhance the calculation accuracy but also to reduce the time cost. [10-13]. Commonly, the calculation conditions are updated at time intervals based on past calculated results and measured data. Hayase T [14] developed a simulation integrated experiment method to reproduce the real flow rate and analyzed the error.

Imagawa and Hayase [15] introduced a measurement-simulation integration method for a turbulent flow to reduce the calculation consumption and also increase accuracy. Li et al [16] indirectly estimated the suction force of a vacuum gripper (swirling air type) by measuring the film pressure distribution. Nakao et al [17] suggested a measurement integrated simulation method to investigate unsteady flow through an orifice in a pipe.

This paper introduces an indirect method for predicting the deformation of the large, thin glass sheet by measuring film pressure. A theoretical model for calculating the film pressure is built, and the deformation curve is shaped to make the calculated result close to the measured pressure data. The method is adopted to estimate a two-dimensional deformation, and the effectiveness of the method is verified experimentally.

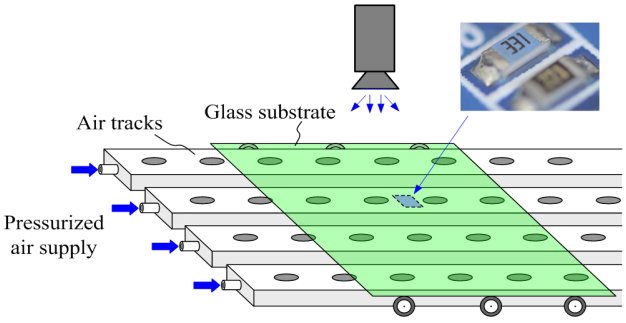

Figure 1 A noncontact transportation system of large glass panels for the inspection process

2 Construction of the air conveyor

Figure 2 shows a sketch of a porous pads equipped air conveyor system that has three conveyor lines. Multiple air conveyor lines are used to ease fabrication and adjustment. For those extremely large, thin glass sheets, air tracks with multiply array of porous pad can be used to produce a uniform film pressure distribution. Pressurized air is provided by the porous pads so that an air film can be formed under the glass sheet. With surface areas like sails, supporting force are formed to levitate the glass sheet on the conveyor. Such non-contact mode during the conveying process can keep the surface clean and prevent surface scratch which are easily caused by traditional method with mechanical contact. In this way, the glass panels are moved by the friction force provided by the installed rollers. In this application, the contact points for the rollers with the surface locate near the edge, and this would not damage the surface quality.

The geometry of a representative area of the noncontact air conveyor is also illustrated in figure 2. Air supply units are regularly arranged on the conveyor surface. The unit is a square, with a length of 45 mm. For each unit, a circular porous pad, which has a diameter of 20 mm and a length of 3 mm, is placed at the center as the restrictor. Grooves (5 mm in width, 1 mm in depth) are set between the units to further uniform the film pressure and to case the stress concentration on the glass sheet. This treatment reduces the bearing capacity and stiffness of the air film; however, without the grooves, the air film would exhibit a large pressure concentrated at the center area, where the flow field would become too complicated to be analyzed.

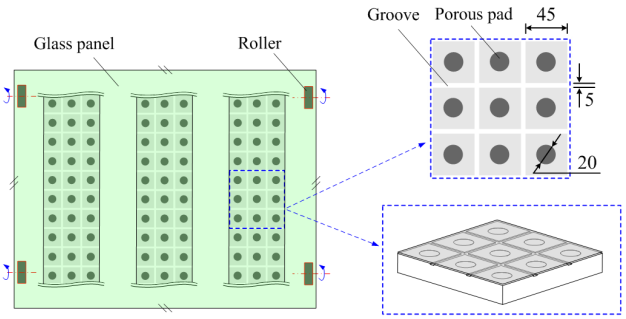

Figure 2 A sketch of an air conveyor system

3. Film pressure distribution

3.1.Mathematical Modeling

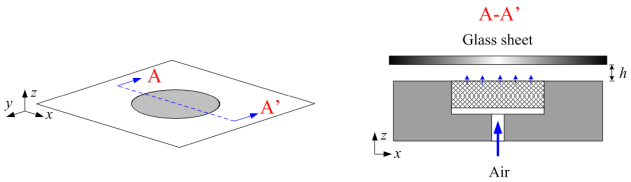

(a) A representative unit (b) flow in the gap

Figure 3 Airflow model

Figure 3 shows a representative unit, which is a square area including a porous pad as well as its surrounding flanges. A Cartesian coordinate is established, and the bottom left point of the gap of the unit is considered as the origin. To reduce the complexity of modeling of flow in the gap, we assume that the airflow is laminar (The Reynolds number is far below 10^3) and film pressure change in z direction is ignored. With the assumption, a simplified Navier-Stokes equation in x-direction can be written as below.

$$-\frac{\partial p}{\partial x}+\mu\frac{\partial^2 u_x}{\partial z^2}=0 \tag{1}$$

where p denotes the film pressure, u_x denotes the flow velocity, and μ denotes the air viscosity.

In z-direction, Navier-Stokes equation can be written as below

$$\mu \frac{\partial^2 u_z}{\partial z^2} = 0 \tag{2}$$

Assuming a no-slip case, the boundary condition that u_x=0 (z=0) and u_x=0 (z=h) can be obtained, and equation (3) is obtained by integrating equation (1) with respect to z

$$u_x = \frac{1}{2\mu}\frac{\partial p}{\partial x}\left(z^2 - hz\right) \tag{3}$$

where h denotes the thickness of the gap.

Similarly, with the boundary velocity that u_z=0 (z=0) and u_z=0 (z=h), the flow velocity u_z can be determined by integrating equation (2) with respect to z,

$$u_z = \omega_0 - \frac{\omega_0}{h} z \tag{4}$$

where ω_0 is the porous walled outflow velocity. The velocity can be obtained by the flow regime through porous media [18, 19].

The continuity equation is expressed as below

$$\frac{\partial(pu_x)}{\partial x} + \frac{\partial(pu_z)}{\partial z} + \frac{\partial p}{\partial t} = 0 \tag{5}$$

Substituting equations (3) and (4) into equation (5), yields

$$\frac{\partial p}{\partial t} = \frac{h^2}{12\mu}\left(\frac{\partial p}{\partial x}\frac{\partial p}{\partial x} + p\frac{\partial^2 p}{\partial x^2}\right) + \frac{p\omega_0}{h} \tag{6}$$

The gap that filled by air should be divided into a number of grids so that the iteration calculation can be applied to obtain the film pressure. Figure 4 shows the generated grids of the calculation domain. The cross-sectional area of the gap is divided into n grids, marked as A[i] (i = 0 – n). Figure 5 shows the procedure to calculate the film pressure. Initially, atmospheric pressure is assigned to each grid. Then, the outlet flow rate from the porous surface is calculated by the Forchheimer equation, and thus, the velocity ω_0 is known. A finite volume method (FVM) is applied to solve equation (6) to obtain the pressure distribution. The Euler explicit method is used for iteration calculation, and the time step is 10^{-8} s. The calculated data are updated and saved after every iteration cycle until the calculation converges. The final results can be obtained after the calculation converges. When the difference between the inlet flow rate and the outlet flow rate is less than ±1%, it can be considered that the calculation converges.

3.2 Experimental apparatus

Figure 6 shows a sketch of the apparatus used to measure the deformation of the glass sheet. An air conveyor with a size of 3 × 3 units is fabricated. A glass sheet with a size of 200mm × 155mm × 0.7mm is supported on the conveyor. The glass sheet is with the following physical properties: 1) the density is 2500 (kg/m^3), 2) Young's modulus is 73 GPa, 3) the Poisson's ratio is 0.25. The glass sheet is supported at four corners, and the vertical distance from the conveyor surface to the supporting point is 150 μm. A high resolution laser sensor is used to measure the deformation of the glass sheet. The laser sensor is fixed on an XY sliding table, the position of which is detected using two installed displacement sensors. The deformation can be measured by the following steps: (1) Place several plug gauges between the conveyor and the glass sheet, and measure the flatness without air supply. (2) Repeat the measurement with air supply. The difference between the two measurements approximates the deformation. Figure 6 shows the moving route of the laser sensor. The slide table moves at a velocity of 5 mm/min for detecting the flatness along x-direction, and, it moves in 5 mm increments without recording the data along y-direction.

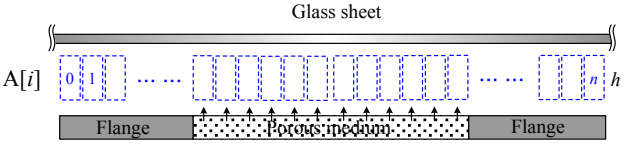

Figure 4 Grid generation of the computational domain

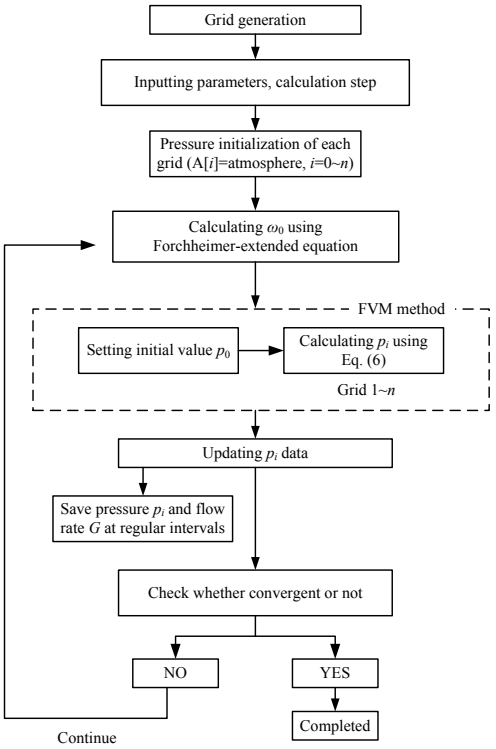

Figure 5 A flowchart indicating the calculation of air film pressure

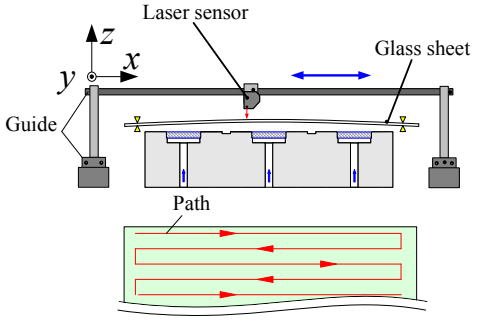

Figure 6 A sketch of the apparatus that shows the measuring method

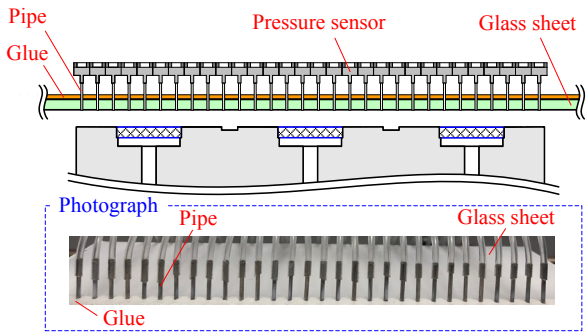

Figure 7 Apparatus for measuring the pressure of the air film

The film pressure distribution is measured to verify the theoretical model. Previous researches [20, 21] reported several methods concerning measurement of the film pressure in the case that the object will not deform and the two surfaces are in parallel. However, in current work, the glass sheet appears an obvious deformation that cannot be ignored since it is very thin. To realize the measurement of the film pressure in a deformed status, the apparatus shown in figure 7 is used. Thirty through-holes are opened on the glass sheet. These holes are with a diameter of 2 mm and arranged at 5 mm intervals. Each hole is individually connected to a high resolution pressure sensor using a metallic tube. A glue layer is coated on the surface to seal the tubes. When we supply pressurized air via the porous pad, under the effect of the air film, the glass sheet is in a deformed status. The deformation of the glass sheet on the centerline was measured and investigated.

3.3 Film pressure distribution

Experiments are first performed to produce an extent of deformation and the film pressure is measured to verify the theoretical model. Here, the deformation and the film pressure on the centerline (AA' in figure 2) are discussed. The deformation versus the position is measured in two cases. The two cases are with different degrees of deformation (Figure 8). Case 1 shows that the glass sheet appears a certain degree of deformation and case 2 shows that the glass sheet is in parallel with the conveyor surface. The case 2 can be achieved by using a sufficiently thick glass sheet. The measured points are passed through by a quadratic fitting curve, which is treated as the real deformation. Thus, the film pressure can be calculated with the theoretical model stated above.

Figure 9 shows the measured film pressure in comparison with the calculated results for the two cases. The supporting points are at a 150 μm height from the surface. The supply flow rate for each unit is set to 3 L /min. The film pressure at the grooves is detected and treated as the boundary to calculate the pressure distribution in each unit. The film pressure is distributed like a parabola, and the grooves uniform the film pressure of different units. Without these grooves, flow interference would appear in the gap, and this makes the flow pattern too complicated to be modeled. Existence of the pressure-equalizing grooves enables independent calculations of the film pressure for each unit, which greatly improves the computation efficiency. Observations on the results show that, for the case 1, the film pressure of the inner unit is slightly larger than that of the outer units, but for the case 2 where the center portion exhibits a larger deformation, the center pressure show a lower value compared with that of the outer area. Although the theoretical model is deduced with the assumption that the glass sheet is in parallel with the conveyor surface, the comparison between the calculated results and the experimental data indicates that the calculation can approximate the experimental film pressure when the deformation is limited within 0.1 mm. It should also be noted that for the maximum deformation that is larger than 0.1 mm but smaller than 0.3 mm, the modeling for the flat center portion might also be valid but not for the outer units.

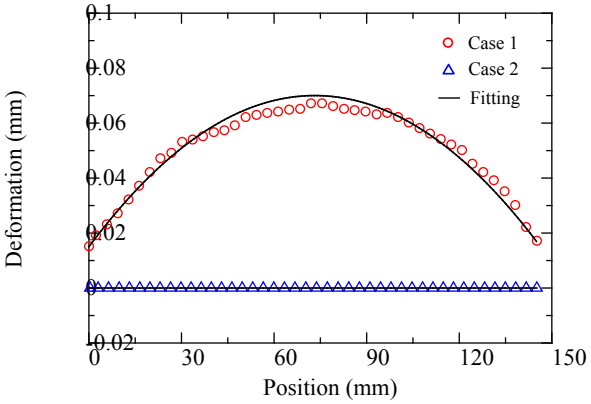

Figure 8 Fittings of the deformation results of two cases

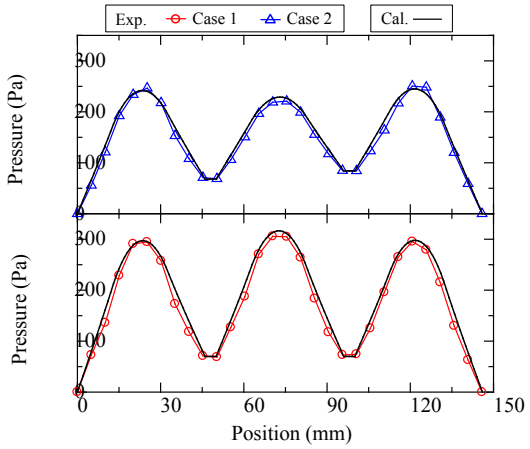

Figure 9 Film pressure distribution of the two cases

4 Estimation of the deformation of the glass sheet and the results

Figure 10 shows a one dimensional case where a glass sheet is supported at two points and deformed by the film pressure is considered. The vertical position of the

supporting points is treated as the base. The distance of the conveyor surface relative to the base is denoted as h_0.The maximum deformation (at the center) relative to the base is denoted as h_c. A quadratic curve expressed by $f(x) = ax^2 + bx + c$ is used to shape the deformation with respect to the position x. Here, a, b, and c are coefficients that need to be determined. The deflections at two sides are treated as the boundary conditions, and two position sensors are installed to detect the edge deflections, which are respectively denoted as δ_1 and δ_2. The left supporting point is regarded as the original point. Using three points on the curve, (L_1, δ_1), $(L/2,h_c)$, and (L_1+L_2, δ_2), determines the coefficients a, b, and c for the deformation curve by the following equations

$$\begin{cases} aL_1^2 + bL_1 + c = \delta_1 \\ a\dfrac{L^2}{4} + \dfrac{b}{2}L + c = h_c \\ aL_1^2 + 2aL_1L_2 + aL_2^2 + bL_1 + bL_2 + c = \delta_2 \end{cases} \tag{7}$$

By this method, the deformation along the centerline in the form of $f(x) = ax^2+bx+c$ can be obtained. The expression of f(x) with $L_1 = 0.028$ m, $L_2 = 0.145$ m and $L = 0.2$ m can then be determined as

$$f(x) = (95.785\delta_1 - 190.258h_c + 94.473\delta_2)x^2 + (-26.149\delta_1 + 38.242h_c - 12.092\delta_2)x + (1.657\delta_1 - 0.921h_c + 0.265\delta_2) \tag{8}$$

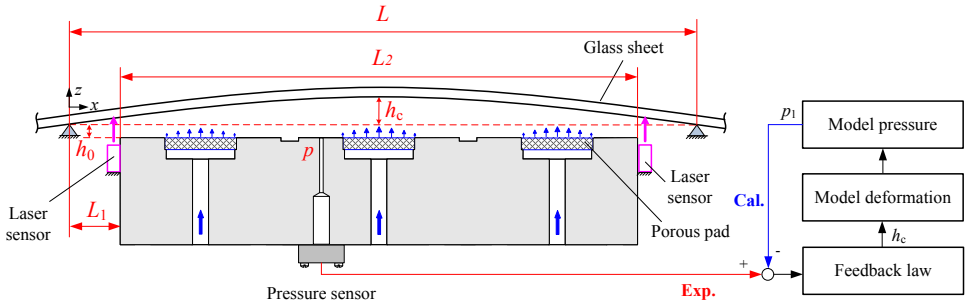

Figure 10 The principle of the one-dimensional estimating method

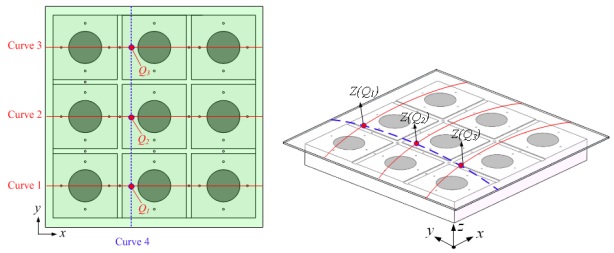

(a) Vertical view (b) Axonometric drawing

Figure 11 The principle of the two-dimensional estimating method

An interpolation method is in use to obtain two-dimensional deformation of the glass sheet. As shown in figure 11, the deformation of the curve 1, curve 2 and curve 3, which are the centerlines of the three rows of the units, can be obtained with the method presented above. To estimate the deformation along y direction, for example, curve 4, three points on the three curves marked as $Q_1(x_1,y_1)$, $Q_2(x_2,y_2)$ and $Q_3(x_3, y_3)$ are selected. Then, with the three points, a parabolic curve $P(y)$ can be fit using equation (9). To be noticed that, with the three centerlines along x-direction P(y) can be calculated, and inversely, with the centerlines along y-direction P(x) can be calculated. Therefore, first, the deformation along y direction is determined at an interval of 3 mm, and second, the deformation along x direction is determined with the same interval. Then, at the overlapping points, the deformation values are averaged to improve the calculating accuracy.

$$P(y) = \frac{(y-y_2)(y-y_3)}{(y_1-y_2)(y_1-y_3)}z(Q_1) + \frac{(y-y_1)(y-y_3)}{(y_2-y_1)(y_1-y_3)}z(Q_2) + \frac{(y-y_1)(y-y_2)}{(y_3-y_1)(y_3-y_1)}z(Q_3) \tag{9}$$

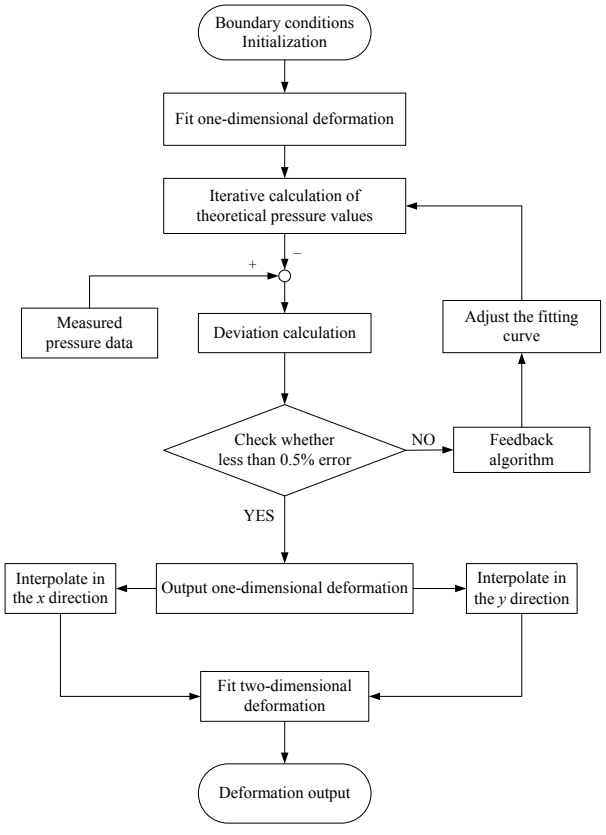

Figure 12 A flowchart indicating the estimation process

Figure 12 shows the estimation procedure. Film pressure in the flange region is measured by pressure sensors which are connected to pressure taps. The measured pressure data is imported into the model and compared with the simulated results to shape the deformation curve by changing h_c. Frist, the simulations are initialized with actual conditions. Then, the film pressure is calculated using the iteration routine until it is sufficiently close to the measured data (within 0.5% error). During the process, During the process, a solution by means of proportional-integral algorithm (Eq. 10) is used to shape the estimated deformation. By this means, we can estimate the deformation of the centerline either along x-direction or along y-direction. Interpolation operations are then applied with the deformation results on the centerlines to obtain the entire two-dimensional deformation.

$$\Delta h_c = -K_p(e + K_i \sum e) \tag{10}$$

where K_p denotes the proportional gain, K_i denotes the integral gain, e denotes the error, and Δh_c denotes the variation of the maximum deflection.

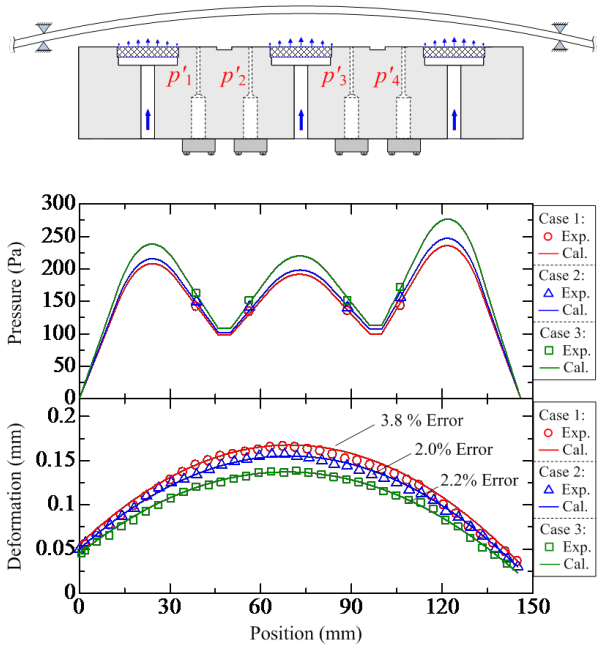

Figure 13 Estimated results of the deformation in comparison with the measured data at the centerline

Adjustment of the deformation shape can be easily implemented to make the calculated pressure close to the measured pressure with only one point used. However, if the pressure of the selected point is not accurately measured, it may cause a great error. Considering this, two points in the grooves are used as the boundary, and four inner pressure measuring points are used as the feedback to assure the reliability for the estimation. The deformation curve is shaped using a nonlinear least square method to take into consideration the error from every point. The estimation processes are conducted for the generated different degrees of deformation (three cases in total). In figure 13, the upper plot shows the calculated results in comparison with the measured film pressure, and the lower plot shows the corresponding deformation. The compressed air is supplied at a flow rate of 3 L/min per unit. The deformation estimations are with an average error of 3.8%, 2.0% and 2.2% for case 1, case 2 and case 3, respectively.

Figure 14 shows the calculated results of the deformation at the six centerlines (three in x-direction and three in y-direction), with which the two-dimensional deformation can be obtained. Figure 15 shows the entire status of the two-dimensional deformation in the case that the glass sheet is fixed at four corners, and observation shows that the center portion exhibits an obvious deformation.

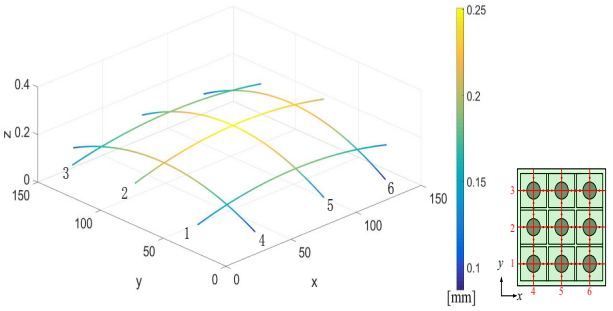

Figure 14 Estimated results of the deformation at all of the centerlines

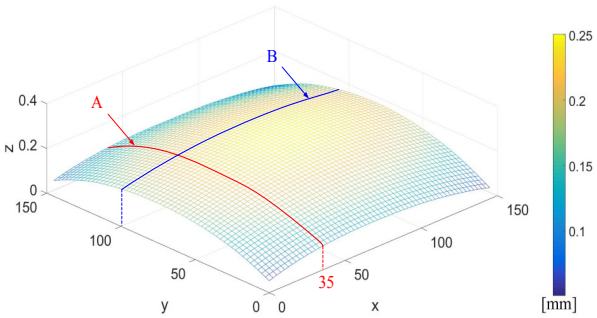

Figure 15 Estimated results of two-dimensional deformation

To verify the effectiveness of the estimating method, the results on the line that deviates from the centerline are also checked. That is, as shown in figure 15, the deformations of the glass sheet at the position A (x=35 mm) and the position B (y=100 mm). Figure 16 compares the experimental results with the estimated results of the deformation curve A and B. The estimated results accord with the experimental data, with an average error around 3%, indicating that the estimating method is feasible. The interpolation method can predict the deformations at the positions deviated from the centerline but one-dimensional estimation is not easy to realize.

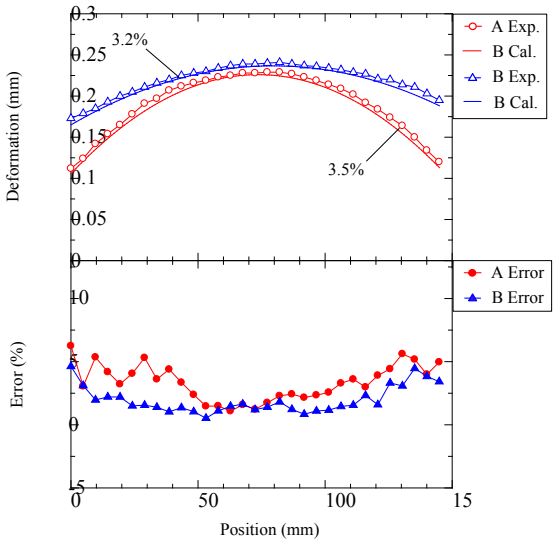

Figure 16 Calculated and experimental results of the deformation of the glass sheet and the errors

Experiments are performed to measure the entire glass deformation with the apparatus shown in figure 6. The glass sheet that has a size of 200 mm × 155 mm × 0.7 mm is in use. Four supporting points distributed at four corners are employed, and the glass sheet is initially 150 μm above the conveyor surface. The deformation with no air supply is treated as the reference, and the real result can be calculated by subtracted from the reference value. So, there is no deformation at the four supporting points and the center portion exhibits an apparent deformation. Figure 17 (a) and (b) show the contour plot of the calculated results and the measured results, respectively. Figure 18 shows the errors, and observation indicates that the errors are all within 4%. Careful observation also shows that large errors appear at the position where the deformation exhibits a steep change. This is because the model cannot describe the flow behavior accurately. However, for the center area where there exists a large deformation, the estimating method works well since the glass sheet is relatively flat, without steep variations.

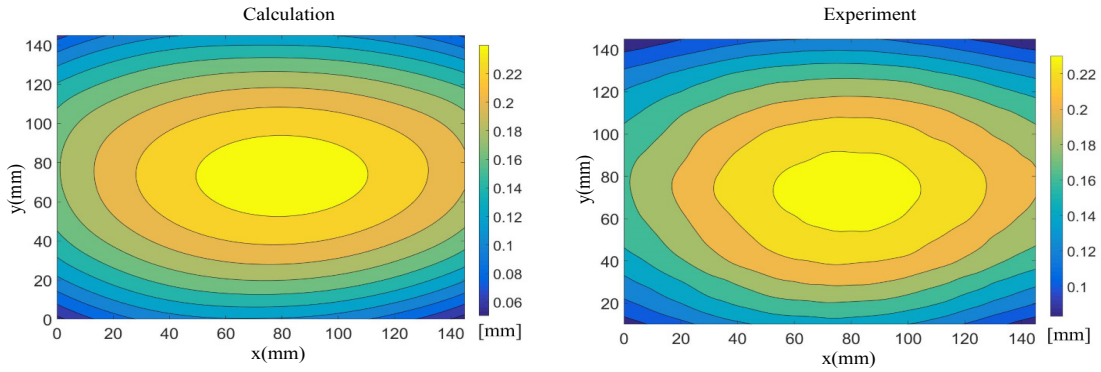

(a) Calculated results (b) Experimental results

Figure 17 Calculated and experimental results of the deformation of the glass sheet

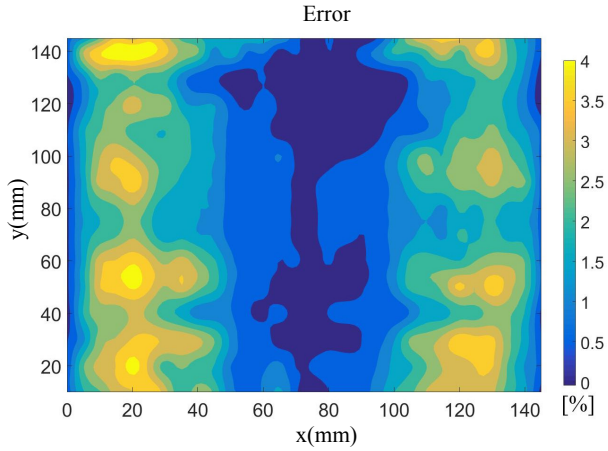

Figure 18 Errors between the Calculated and experimental results of the deformation of the glass sheet

5 Conclusions

A method for estimating the deformation of a glass sheet on a noncontact air conveyor by integration of measurement and simulation of the film pressure is proposed. A theoretical model is established within typical units, and the model is solved to attain the film pressure. An algorithm is used to adjust the deformed shape of the glass sheet with the measured film pressure to achieve that the calculated

film pressure accords with the experimental data. Film pressure are monitored at several positions, and, the film pressure at the grooves are used as the boundary and that at the flange area are used as the feedback. Experimental setup is constructed to measure the two-dimensional deformation and the film pressure simultaneously. First, film pressure distributions are measured in a deformed and a non-deformed status, and it is observed that the calculated pressure shows good agreement with the experimental data. Then, the film pressure feedback method is used to estimate one-dimensional deformation on the centerlines along x-direction and y-direction, with which an interpolation operation is applied to obtain the two-dimensional deformation of the glass sheet. Experiments are performed to measure the deformation of the entire area. Comparison of the estimation results with the measured data indicates that the estimating method can afford a 4% accuracy. Furthermore, the estimating method shows a good performance for the area where the deformation exhibits a smooth variation. But for the area with a steep variation, the estimating results show relatively large errors.

Author Contributions: Conceptualization, Wei ZHONG; Data curation, Rui YANG; Investigation, Jiwen Fang; Methodology, Rui YANG and Chong LI; Resources, Chong LI; Validation, Jiwen Fang; Writing – original draft, Rui YANG; Writing – review & editing, Wei ZHONG.

Conflict of Interest: The author(s) declare(s) that there is no conflict of interest regarding the publication of this paper.

Acknowledgments: This study was supported by the Natural Science Foundation of Jiangsu Province (Grant No. BK20181467) and the National Natural Science Foundation of China (Grant No. 51675247).

References

[1] Chen X.; Zhong W.; Li C.; Fang J.; Liu F. Development of a contactless air conveyor system for transporting and positioning planar objects. Micromachines 2018, 9(10), 487.

[2] Zhong W.; Ji X.; Li C.; Fang J.; Liu F. Determination of permeability and inertial coefficients of sintered metal porous media using an isothermal chamber. Appl. Sci 2018, 8(9), 1670.

[3] Shi K.; Li X.; Experimental and theoretical study of dynamic characteristics of Bernoulli gripper. Precis. Eng 2018, 52, 323–331.

[4] Savkiv V.; Mykhailyshyn R.; Duchon F. Gas dynamic analysis of the Bernoulli grippers interaction with the surface of flat objects with displacement of the center of mass. Vacuum 2019, 159, 524–34.

[5] Devitt D. The physics of glass flotation. Semicond. Int. Japan 2009, 5, 19-24.

[6] Im I.T.; Park C.W.; Kim K.S. A numerical study on the flow and heat transfer characteristics in a noncontact glass transportation unit. J. Mech. Sci. Technol. 2009, 23(12), 3416-3423.

[7] Amano K.; Yoshimoto S.; Miyatake M.; Hirayama T. Basic investigation of noncontact transportation system for large TFT-LCD glass sheet used in CCD inspection section. Precis. Eng 2011, 35(1), 58–64.

[8] Oiwa N.; Masuda M.; Hirayama T.; Matsuoka T.; Yabe H. Deformation and flying height orbit of glass sheets on aerostatic porous bearing guides. Tribol. Int. 2012, 48, 2–7.

[9] Miyatake M.; Akahori H.; Yoshimoto S. Deformation of large liquid crystal display glass sheets across a gap between noncontact transportation devices. Precis. Eng. 2016, 46, 360–368.

[10] Funaki T.; Kawashima K.; Inoue S. Application of measurement integrated simulation to unsteady flow monitoring. IEEE 2006 SICE-ICASE International Joint Conference, Busan, Korea, 2006, pp. 5218-5221.

[11] Kontz M.E.; Book W.J.; Frankel J.G.; Pressure based exogenous force estimation. ASME 2006 Int. Mechanical Engineering Congress and Exposition, Chicago, Illinois, USA, 2006, pp.111–120.

[12] Yoon J.Y.; Singh R. Estimation of interfacial forces in a multi-degree of freedom isolation system using a dynamic load sensing mount and quasi-linear models. J. Sound Vib. 2011, 330(18-19), 4429–4446.

[13] Watanabe S.; Inoue H.; Fumoto K. An estimation of static aerodynamic forces of box girders using computational fluid dynamics. Wind Struct. 2004, 7(1), 29–40.

[14] Hayase T. F051001 Integration of Measurement and Simulation in Flow Analysis. 2011.

[15] Imagawa K.; Hayase T. Numerical experiment of measurement-integrated simulation to reproduce turbulent flows with feedback loop to dynamically compensate the solution using real flow information. Comput. Fluids 2010, 39(9), 1439–1450.

[16] Li X.; Horie M.; Kagawa T. Pressure-distribution methods for estimating lifting force of a swirl gripper. IEEE/ASME Trans. Mechatronics 2013, 19(2), 707–718.

[17] Nakao M.; Kawashima K.; Kagawa T. Measurement integrated simulation of wall pressure measurements using a turbulent model for analyzing oscillating orifice flow in a circular pipe. Comput. Fluids 2011, 49(1), 188–196.

[18] Zhong W.; Gu X.; Li X.; Kagawa T. Study on the basic characteristics of a noncontact air conveyor for large glass sheets. Adv. Mech. Eng. 2017, 9(4), 1–13.

[19] Zhong W.; Li X.; Liu F.H.; Tao G.; Lu B.; Kagawa T. Measurement and correlation of pressure drop characteristics for air flow through sintered metal porous media. Transp. Porous Med.2014, 101(1), pp.53-67.

[20] Possamai F.C.; Ferreira R.T.S.; Prata A.T. Pressure distribution in laminar radial flow through inclined disks. Int. J. Heat Fluid Flow 2001, 22(4), 440-449.

[21] Li X.; Kawashima K.; Kagawa T. Analysis of vortex levitation. Exp. Therm. Fluid Sci. 2008, 32(8), 1448-1454.

Viser Technology Pte. Ltd.
Mechanical Engineering Science
doi: 10.33142/mes.v2i2.3165

Research Article Open Access

Simulation research on dynamic performance of the new type high-pressure solenoid valve

Qihui YU[1,2*], Qiancheng WANG[1], Kaifei ZHANG[3], Weiwei ZHENG[4]

1 School of Mechanical Engineering, Inner Mongolia University of Science and Technology, baotou, China
2 The State Key Laboratory of Fluid Power and Mechatronic Systems, Hangzhou, China
3 College of Mechanical and Electrical Engineering, Henan Agricultural University, 450002, Zhengzhou, China
4 College of Mechanical and Electrical Engineering, Henan radio and television University, Zhengzhou, China,

***Corresponding Author:** Qihui YU, Baotou, 014010,China; yqhhxq@163.com*

Abstract:
To improve energy density, the transportation, storage, and operations of hydrogen, methane, and compressed air vehicles currently require high-pressure compression. High-pressure solenoid valve becomes the vital element to above system. In order to reduce leakage and aerodynamic force influence, a new type high-pressure solenoid valve was proposed. The simulation model which included electromagnetic model, aerodynamic force model was established by means of the nonlinear mathematic models. Using the software MATLAB/Simulink for simulation, the dynamic response characteristics of high-pressure pneumatic solenoid valve were obtained under different pulse width modulation (PWM) input control signals. Results show that, first of all, the new type of high-pressure solenoid valve can meet the switch requirement. Secondly, the opening movement and closing movement of the spool lags the PWM rising signal, and the coil current fluctuates significantly during the movement of the spool. Lastly, on/off status of high-pressure valve cannot be represented by the duty cycle. This research can be referred in the design of the high-pressure solenoid valve..

Keywords: *high-pressure solenoid valve; dynamic response performance; pulse width modulation; the duty cycle*

1 Introduction

To improve energy density, the transportation, storage, and operations of hydrogen, methane, and compressed air vehicles currently require high-pressure compression. The use of electronic control technology is a major direction for the development of above systems. To gas distribution system, the high-pressure solenoid valve is the vital part. The control performance of the gas distribution system is mainly determined by the applied high-pressure solenoid valve. Its dynamic response characteristics directly affect the efficiency and reliability of the system.

Normally, the electromagnetic switch valve is used as the pilot valve of the control stage [1], which is directly controlled by the pulse width modulation (PWM) method and the output pulse flow rate is the control variable of the power level pilot valve. Most researches are based on simulation under the no-load condition of the solenoid valve [2-3], and the pressure characteristics of the fluid is neglected. In order to reduce leakage and aerodynamic force influence, a new type high-pressure solenoid valve was proposed. The simulation model which included electromagnetic model, aerodynamic force model was established by means of the nonlinear mathematic models. Using the software MATLAB/Simulink for simulation, the dynamic response characteristics of high-pressure pneumatic solenoid valve were obtained under different pulse width modulation (PWM) input control signals. This research can be referred in the design of the high-pressure solenoid valve.

2 Working principle of high-pressure solenoid valve

To reduce leakage and aerodynamic force influence, the main structure consists two parts: one is pressure compensated which is adopted slide valve mechanism; the other is seal which is adopted poppet valve mechanism which has good sealing performance. Figure 1 is the structural schematic diagram of the force balanced high pressure solenoid valve which was used in high pressure pneumatic engine.

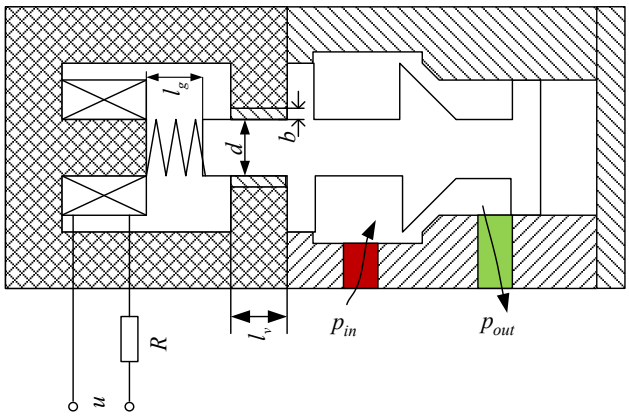

Figure 1 The structure of high-pressure solenoid valve

The valve working process can be divided into the following two stages:

2.1 Opening phase

According to the requirements of gas distribution control, the electronic control unit sends control pulses to the drive module of the solenoid valve at a specific time. The drive module provides a high peak drive voltage, and the solenoid valve generates an electromagnetic force on the spool. When the electromagnetic force is greater than the preload of the return spring, the spool moves upward to quickly open the valve.

2.2 Closing phase

When the control pulse is terminated, the driving voltage is cut off, and the solenoid valve is de-energized, the electromagnetic force quickly disappears. Under the action of the return spring, the spool moves downward until the solenoid valve is completely closed.

The high-pressure solenoid valve used in the pneumatic engine gas distribution system should have good fast response performance, the main reasons are the following aspects:

(1) The rapid opening of the solenoid valve is conducive to ensuring the accurate timing of the valve and the rapid formation of high pressure; the quick closing of valve is helpful to ensure the quick cutting off of high-pressure gas. The slow opening of the valve makes the high-pressure gas entering the pneumatic engine unable to be distributed according to the predetermined control law, thus greatly reducing the economy and efficiency of the pneumatic engine.

(2) The response time of the closing process and opening process of the solenoid valve has a great influence on the air distribution of the pneumatic engine. Especially when the air supply pressure is high and the engine's angular speed is very fast, in order to obtain stable output power, the response time of the solenoid valve should be appropriately short.

From the above analysis, it can be seen that shortening the response time of the closing and opening process of the solenoid valve is the key to achieving good performance of the electronically controlled gas distribution system, and also the key to improving the comprehensive performance of the pneumatic engine.

3 Theoretical analysis of driving characteristics of high-pressure solenoid valve

The flow of gas in a valve is a thermodynamic process of a complex open system. To simplify the model, the following assumptions were made [4]:

(1) Pressure fields and velocity fields in chambers are homogenous;

(2) Leakage and pressure loss are ignored;

(3) The working medium is an ideal air that followed the equation of an ideal air state;

(4) Impact contact influence is ignored.

3.1 Electromagnetic characteristic equation of solenoid valve

The working process of the solenoid valve is simplified into the electromagnetic circuit equation and the equation of motion [5-11].

In general, the inductance of the electromagnet can be expressed by equation (1):

$$L=\mu_0\pi D^2N^2l_v \Big/ 4l_v\left(l_0-x\right)+rD \tag{1}$$

where μ_0 is the vacuum permeability, D is armature diameter, N is coil turns, l_v is the length of valve spool armature, r is the average width of the working air gap, l_0 is the maximum length of the working air gap, x is spool displacement.

The derivative of equation (1) is obtained:

$$\frac{dL}{dx}=4\mu_0\pi D^2N^2l_v^2 \Big/ \left[4l_v\left(l_0-x\right)+rD\right]^2 \tag{2}$$

Using the principle of virtual displacement and setting the amount of change in the air gap of the electromagnet, the mechanical work done by electromagnetic force can be obtained. The mechanical work is equal to the change of the total magnetic energy of the system. According to equation (3), the electromagnetic force can be obtained as shown in equation (4):

$$Fdx=dW=1/2\,i^2dL \tag{3}$$

$$F=\frac{1}{2}i^2\,dL/dx \tag{4}$$

where dx is the amount of change in the air gap of the electromagnet, Fdx is mechanical work, dW is the change in total magnetic energy, i is the current in the solenoid coil.

The current in the solenoid valve coil can be obtained by equation (5):

$$V_s=iR+L\frac{di}{dt}+i\frac{dL}{dt} \tag{5}$$

where V_s is the coil excitation voltage, R is resistance of the coil, t is time.

Before the armature is moved, $dL/dt=0$; once the armature is attracted, the kinematic counter electromotive force will be generated. At this time, the spool motion

voltage equation is as follows:

$$e = i\frac{dL}{dt} = vi\frac{dL}{dx} \tag{6}$$

where v is the movement speed of the spool.

3.2 Dynamic equation of solenoid valve

The equation of motion of the solenoid valve can be expressed as follows:

$$F_{mag} - k_s x_0 - k_s x - b_1 \dot{x} - F_{flu} = ma \tag{7}$$

where a is motion acceleration, F_{mag} is electromagnetic force of the solenoid valve, k_s is stiffness of the return spring, x_0 is initial pretension length of the return spring, b_1 is the viscosity coefficient of air, F_{flu} is the aerodynamic force suffered by the spool, m is spool mass.

As can be seen from equation (7), in the opening process of the solenoid valve, in order to shorten the response time, it is expected that the electromagnetic force will increase, and the air force on the valve core, the return spring force, and the mass of the valve core will decrease. In the closing process, in order to shorten the response time, it is hoped that the solenoid valve acting force will quickly reduce to zero, the return spring acting force will increase, the aerodynamic force of the valve core will increase, the gas resistance will decrease, and the quality of the valve core will decrease.

3.3 Aerodynamic equation of solenoid valve spool

From the spool structure shown in Figure 1, the principle diagram of the mechanism can be obtained as shown in Figure 2:

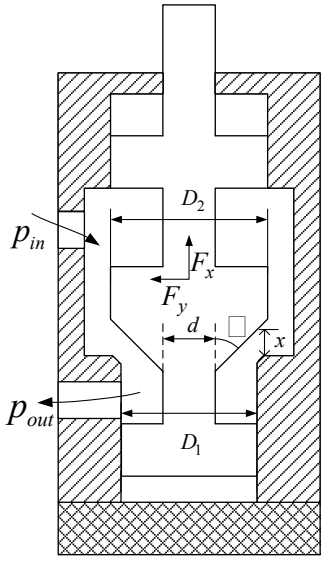

Figure 2 The schematic structure of the poppet valve

The aerodynamic force received by the spool can be derived from Euler's law of momentum, as shown in Equation 8 below:

$$F_{flu} = -\frac{d}{dt}\left[\int_V \rho \vec{u} dV\right] - \int_{A_e} \vec{u}\left(\rho \vec{u} dA_e\right) \tag{8}$$

where V is volume of the control body formed by the inner cavity of the valve core, ρ is gas density, $\vec{u}$ is gas flow rate, A_e is equivalent cross-sectional area of the flow cross-section.

The above formula is mainly composed of two parts, among which the first term on the right represents the transient aerodynamic force required for the valve core inner chamber to control the gas in the body to accelerate (or decelerate), the second term represents the steady-state aerodynamic force caused by the different velocities of the gas at different positions. Because the transient aerodynamic force of the spool is mainly caused by the speed change of the spool, and the air gap of the spool of the switching valve is very short, the maximum speed that the spool can reach is limited, so the influence of the transient aerodynamic force is ignored here.

Finally, the aerodynamic force experienced by the spool can be expressed as:

$$F_{flu} = \int_{D_1/2}^{D_2/2} 2p\pi r \cos\alpha \sin\alpha dr - \bar{\rho} q_{mg} v_1 \cos\alpha \tag{9}$$

$$p = p_{in} - \frac{6\eta q_{mg}}{\bar{\rho}\pi x^3 \sin^4\alpha} \ln\frac{2r}{D_1} \tag{10}$$

$$q_{mg} = \frac{\bar{\rho}\pi x^3 \sin^4\alpha \left(p_{in} - p_{out}\right)}{6\eta \ln\left(D_1/D_2\right)} \tag{11}$$

$$v_1 = c_v \sqrt{\frac{2}{\bar{\rho}}\left(p_{in} - p_{out}\right)} \tag{12}$$

$$\bar{\rho} = \left(p_{in} + p_{out}\right)/2R_g T \tag{13}$$

where p_{in} is pressure of the intake, p_{out} is pressure of the exhaust, x is distance the spool moves, α is half the cone angle of the cone valve, η is dynamic viscosity of a gas, R_g is gas constant, T is temperature of the environment, c_v is speed factor, p is velocity distribution at the orifice, q_{mg} is the mass flow of gas through the orifice, $\bar{\rho}$ is average density of the gas in the valve. The remaining structural parameters can be seen in Figure 2.

Considering the continuity characteristics of aerodynamic force, assuming that the steady-state aerodynamic force maintains a linear relationship with its opening within the spool action range, so a correction coefficient is introduced in this way, and the above aerodynamic force is corrected as:

$$F_p = \left(k_{f1} + k_{f2}\frac{x}{x_m}\right) F_{flu} \tag{14}$$

Consider the boundary conditions when the correction coefficient is satisfied: when the opening and closing of the valve is $x \to 0$, $F_P = k_{f1}F_f = F_f$, so take $k_{f1}=1$; When the opening degree of the on-off valve is the maximum value, $F_P = (1+k_{f2})F_f$, in this paper, the empirical value $k_{f2}=1.15$ is used. In this way, the aerodynamic force of the solenoid valve can be obtained.

From the above analysis, the block diagram of the nonlinear model of the spool can be obtained as follows:

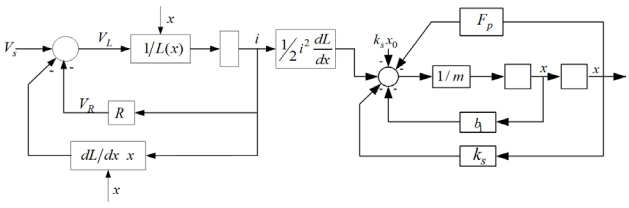

Figure 3 Non-linear model of the solenoid valve spool

4 Dynamic characteristics simulation analysis

The high-pressure solenoid valve performs "on" and "off" actions according to the PWM control electrical signal. It can be seen that the flow rate of the on-off valve is proportional to the duty cycle (τ = pulse width / pulse period) of the input voltage signal. The larger the duty cycle, the greater the corresponding control flow rate. Therefore, to study the dynamic performance of the electromagnetic switch valve, it is necessary to simulate the movement of the spool under the PWM control signals of different duty cycles. In this study, the step signal is used to excite the PWM signal module. The PWM signal controls the on and off of the electromagnetic switch valve.

In this study, the simulation parameters were set to 3MPa gas pressure, PWM signal frequency 20Hz, and PWM signal duty cycle τ were 0.25, 0.5, 0.75, respectively. The relationship between the PWM signal of the switching valve, the coil current i of the electromagnet, and the displacement S of the valve core is shown in Figures 4-6.

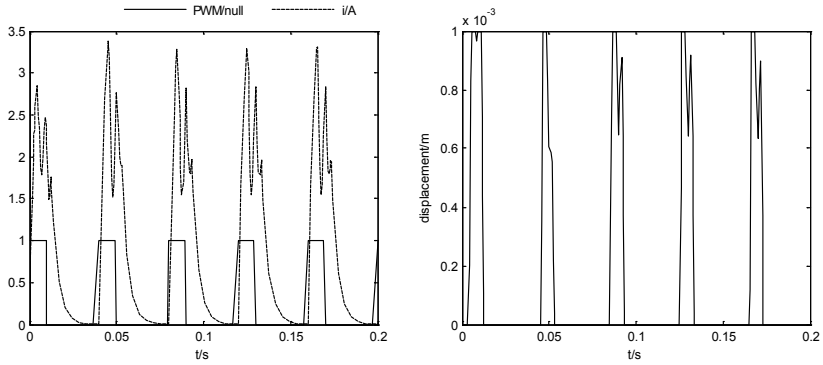

Figure 4 The solenoid valve PWM signal, coil current and spool displacement curve (τ=0.25)

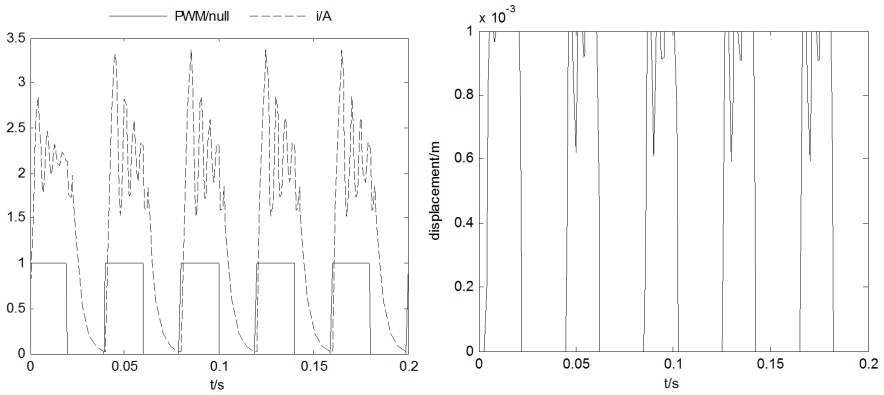

Figure 5 The solenoid valve PWM signal, coil current and spool displacement curve (τ=0.5)

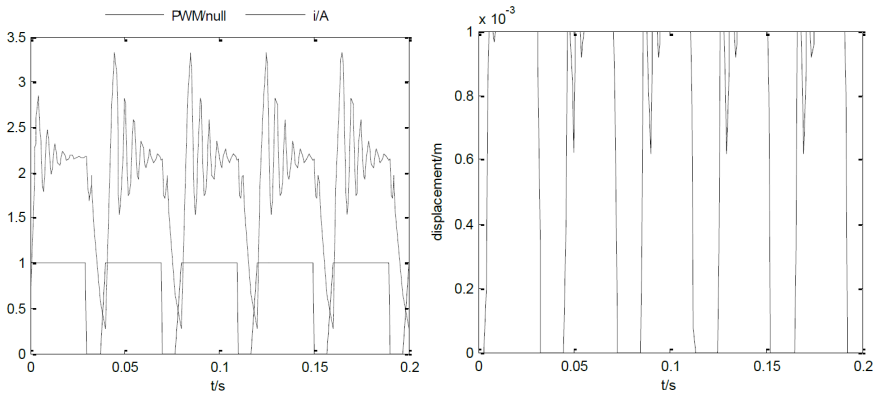

Figure 6 The solenoid valve PWM signal, coil current and spool displacement curve (τ=0.75)

By analyzing the relationship between the PWM signal with different duty cycles, coil current, and spool displacement in Figure 4-6, the following conclusions can be drawn:

(1) The spool opening movement lags the PWM rising signal, and the coil current fluctuates significantly during the movement of the spool. The reason is that when PWM input high level, the coil is connected to the power supply voltage, where the current gradually increases from zero, and the law of magnetic flux growth is the same as the current. When the current increases so that the electromagnetic attraction generated is sufficient to move the armature, the armature begins to move. After the armature moves, the air gap decreases, the magnetic resistance in the air gap changes, and the coil inductance changes, causing a small back electromotive force, which reduces the coil current. This caused the coil current to fluctuate.

(2) The spool closing movement also lags the PWM falling signal, and the coil current fluctuates significantly during the spool movement. The reason is when PWM input low level, the excitation in the coil is lost, and the magnetic flux begins to decay. Due to the induced potential and the eddy current in the iron core, the electromagnetic attraction is gradually reduced. When the suction force is not enough to hold the armature, the armature starts to release, the air gap increases, the magnetic resistance in the air gap changes, and the coil inductance changes, causing a small positive potential to increase the coil current. This causes the coil current to fluctuate when the spool is closed.

(3) When other parameters are unchanged, the relationship between the duty cycle of the PWM signal, the coil current and the displacement of the spool has the following rules: with the decrease of τ, the duration of the high level of the PWM input signal shortens, and the coil the maximum value that the current can reach is decreasing. When τ is reduced to a certain value, the force of the electromagnet is not enough to move the armature then the spool cannot be opened. At this time, the solenoid valve will be in a normally closed state, and the PWM signal cannot be play a controlling role; with the increase of τ, the high level duration of PWM input signal is extended. When the low level of PWM signal is not enough to close the valve core, the coil current will start to increase. The valve core cannot be closed, and the PWM signal cannot play a control role at this time.

5 Conclusion

Through the above research on the dynamic characteristics of the solenoid valve and the simulation results, the following conclusions can be drawn:

(1) Since the presence of the high-speed switching valve induced current causes the opening and closing of the spool to lag behind the PWM control signal, the duty ratio τ cannot be completely changed arbitrarily.

(2) Due to the time delay, the duty cycle cannot fully represent the switching state of the spool.

In summary, the combination of MATLAB / Simulink can better complete the simulation analysis of the modeling process of pneumatic high-pressure high-frequency solenoid valves. Provide a basis for the control efficiency and control accuracy of high-pressure high-frequency pneumatic solenoid valves.

Author Contributions: Qihui YU contributed to the conception of the study; Qiancheng WANG contributed significantly to analysis and manuscript preparation; Kaifei ZHANG performed the simulation model; and Yiwei Zheng helped perform the analysis with constructive discussions.

Conflict of Interest: There is no conflict of interest regarding the publication of this paper.

Acknowledgments: The research work presented in this paper is financially supported by a grant (NJZZ18139) from the scientific research project of Universities in Inner Mongolia, a grant (2018BS05003) from the Natural Science Foundation of Inner Mongolia, and a grant (2017QDL-B07) from Inner Mongolia University of Science and Technology Innovation Fund Project.

References

[1] Lihuan, G; Kaizhang, S; Gang, Z. The new high speed digital switch valve is a multi - way reversing valve. Journal of Lanzhou University of Technology. 2006, 32(3), 56-58, DOI: CNKI:SUN:GSGY.0.2006-03-015

[2] Yugui, L;Xiaoming, Y;Xuejie, G. Study on static characteristics of PWM high speed switching valve. Journal of taiyuan heavy machinery college. 2002, 23(1), 68-71,DOI: 10.3969/j.issn.1673-2057.2002.01.017

[3] Zhong, L;Weiping, L; Qian, H. Modeling and simulation of dynamic response of high speed switching solenoid valve. Journal of Natural Science of Hunan Normal University. 2009, 32(3), 53-57, DOI: 10.3969/j.issn.1000-2537.2009.03.013

[4] Gang Y; Youbin S; Baoren L. Numerical simulation on dynamic characteristics of Extra-high pressure pneumatic Blowing valve. China Mechanical Engineering. 2012, 23(1): 42-45 (In Chinese) DOI: 10.3969/j.issn.1004-132X.2012.01.009.

[5] Lihui, W; Zhixin, Y; Minghui, Y. Simulation and testing of dynamic characteristics of digital closed loop fiber optic current transformer. Chinese Journal of Scientific Instrument. 2010, 31(8), 1890-1895, DOI: CNKI:SUN:YQXB.0.2010-08-033

[6] Yi, L; Bin, G; Xiaowang, P. Study on the comprehensive performance test system of direct-acting pneumatic solenoid valve. Chinese Journal of Scientific Instrument. 2011, 32(4), 795-800, DOI: CNKI:SUN:YQXB.0.2011-04-013

[7] Xiaowang, P; Min, L; Bin, G. Simulation and experimental study of dynamic characteristics of pneumatic solenoid valve. Journal of China University of Metrology. 2010, 21(3), 232-236, DOI: CNKI:SUN:ZGJL.0.2010-03-010

[8] Xiao L; Wenjie, N. Design calculation of solenoid valve. Electric Switch. 2008, (3), 11-13, DOI: CNKI:SUN:DQKG.0.2008-03-006

[9] Farong, D; Juan, H. Simulation and Response Analysis of High-speed Solenoid Valve for EUI. Science Technology and Engineering. 2011, 11(5), 1080-1083, DOI: CNKI:SUN:KXJS.0.2011-05-038.

[10] Ting, C. Simulation of high pressure common rail solenoid valve of diesel engine and its driving circuit. Beijing Jiaotong University. 2009, DOI: 10.7666/d.y1577655

[11] Zhihong, B; Yuhu, Z. Simulation and analysis of dynamic characteristics of electromagnet. Journal of Electric Power.2009, 19(3), 200-201, DOI: 10.3969/j.issn.1005-6548.2004.03.006

Publisher: Viser Technology Pte. Ltd.

URL: www.viserdata.com

Add.:21 Woodlands Close, #08-18,

Primz Bizhub SINGAPORE (737854)